Energy

FOSSIL

DOE/BC/10216-13
(DE84012721)

RELATIONSHIP OF PORE STRUCTURE TO FLUID BEHAVIOR IN LOW PERMEABILITY GAS SANDS

1984 Final Report

By
Norman R. Morrow
K. R. Brower
Neal H. Kilmer

September 1984
Date Published

Work Performed Under Contract No. AS19-80BC10216

New Mexico Petroleum Recovery Research Center
New Mexico Institute of Mining and Technology
Socorro, New Mexico

Technical Information Center
Office of Scientific and Technical Information
United States Department of Energy

DISCLAIMER

This report was prepared as an account of work sponsored by an agency of the United States Government. Neither the United States Government nor any agency thereof, nor any of their employees, makes any warranty, express or implied, or assumes any legal liability or responsibility for the accuracy, completeness, or usefulness of any information, apparatus, product, or process disclosed, or represents that its use would not infringe privately owned rights. Reference herein to any specific commercial product, process, or service by trade name, trademark, manufacturer, or otherwise does not necessarily constitute or imply its endorsement, recommendation, or favoring by the United States Government or any agency thereof. The views and opinions of authors expressed herein do not necessarily state or reflect those of the United States Government or any agency thereof.

This report has been reproduced directly from the best available copy.

Available from the National Technical Information Service, U. S. Department of Commerce, Springfield, Virginia 22161.

Price: Printed Copy A07
Microfiche A01

Codes are used for pricing all publications. The code is determined by the number of pages in the publication. Information pertaining to the pricing codes can be found in the current issues of the following publications, which are generally available in most libraries: *Energy Research Abstracts (ERA); Government Reports Announcements* and Index (*GRA* and I); *Scientific and Technical Abstract Reports (STAR);* and publication NTIS-PR-360 available from NTIS at the above address.

DOE/BC/10216-13
(DE84012721)
Distribution Category UC-92a

RELATIONSHIP OF PORE STRUCTURE TO FLUID BEHAVIOR IN LOW PERMEABILITY GAS SANDS

1984 Final Report

Norman R. Morrow, *Principal Investigator*
K. R. Brower, *Professor of Chemistry*
Neal H. Kilmer, *Research Chemist*

Contributors:

Shirleen Bretz
Vijaya Dandge
Deborah Hagen
Janet Pitman
Jill S. Ward
Kai-Yuan Wei

New Mexico Petroleum Recovery Research Center
New Mexico Institute of Mining and Technology
Socorro, New Mexico

Technical Project Officer—James Chism

Date Published - September 1984

TECHNOLOGY TRANSFER BRANCH
BARTLESVILLE PROJECT OFFICE
U.S. DEPARTMENT OF ENERGY
BARTLESVILLE, OKLAHOMA

TABLE OF CONTENTS

LIST OF TABLES.....ii

LIST OF FIGURES.....iv

SUMMARY.....xi

SECTION 1. PRESSURE SENSITIVITY OF PERMEABILITY.....1

SECTION 2. THE EFFECT OF FLUID, CONFINING PRESSURE AND TEMPERATURE ON ABSOLUTE PERMEABILITIES OF LOW PERMEABILITY SANDSTONES.....42

SECTION 3. EFFECT OF ACID LEACHING AND PRESENCE OF FRACTURES ON PRESSURE SENSITIVITY.....43

SECTION 4. ADSORPTION.....60

SECTION 5. MATHEMATICAL MODELLING AND CORRELATIONS.....72

APPENDIX 1. PERMEABILITY VS. CONFINING PRESSURE RELATIONSHIPS.....100

APPENDIX 2. AN ALTERNATIVE METHOD - RIDGE REGRESSION.....125

ACKNOWLEDGMENT.....131

LIST OF TABLES

Table 1.1 Results for Suite 2 Samples (High in Carbonate Cement).....14

Table 1.2 Constituents of High Carbonate Core Samples Determined by Mineral Analysis from Thin Section.....15

Table 1.3 Results for Multi-Well Samples.....16

Table 1.4 Multi-Well Samples on Hand.....17

Table 1.5 Variables Used in Regression Analyses.....18

Table 3.1 Summary of Core Properties (Measured at Ambient Temperature and 500 psi Overburden Pressure).....48

Table 3.2 RBE-01 (6923.3 ft) Effect of Carbonate Removal by Acetic Acid.....49

Table 3.3 Mobil 26-7G (3309 ft) Effect of Carbonate Removal by Acetic Acid.....50

Table 3.4 Arco Exxon L-36 (3701 ft) Effect of Carbonate Removal by Acetic Acid.....51

Table 3.5 RBE-01 (5863.6 ft) Effect of Carbonate Removal by Acetic Acid.....52

Table 3.6 Multi-Well Fractured Sample MWX-1 34-10 (6002.3-6002.5 ft).....53

Table 3.7 Multi-Well Fractured Sample MWX-1 21-4A (5271.6-5272 ft).....54

Table 3.8 Multi-Well Fractured Sample MWX-1 13-18 (4846.5-4847 ft).....55

Table 3.9 Multi-Well Fractured Sample MWX-1 29-31 (5730.9-5731.2 ft).....56

Table 3.10 Multi-Well Fractured Sample MWX-1 13-18 (4846.5-4847 ft).....57

Table 4.1 Effect on Heptance Adsorption of Treating Montmorillonite with Tetramethylammonium Chloride.....65

Table 5.1 The Effect of Overburden on Permeability and Crack Thickness of Suite 2 Samples (High in Carbonate Cement).....85

Table 5.2 Crack Thicknesses Estimated for Suite 1 Samples (Assorted Cores).....86

Table 5.3 C and n Values Determined for Old Man Mountain #2, 10570 S BETC, CIGE 21, U78JP36, and (MWX-2) Core Samples at the Indicated Temperatures and Confining Pressures.....87

Table 5.4 C and n Values Obtained for a Single Sample at a Single Temperature but Varying Confining Pressures.....88

LIST OF FIGURES

Fig. 1.1 Pressure sensitivity behavior of a low permeability core sample.....19

Fig. 1.2 Porosity vs. depth.....20

Fig. 1.3 Porosity vs. total carbonate.....21

Fig. 1.4 $K_{\infty,5000}$ vs. porosity.....22

Fig. 1.5 Comparison of visible porosity observed in thin sections and porosity measured by routine core analysis.....23

Fig. 1.6 Percent of Na-feldspar vs. depth.....24

Fig. 1.7 $K_{\infty,5000}$ vs. percent Na-feldspar.....25

Fig. 1.8 Sensitivities of core samples to confining pressure shown by plot of $K_{\infty,500}$ vs. $K_{\infty,5000}$.....26

Fig. 1.9 Plot of ψ_{∞} vs. ψ_p.....27

Fig. 1.10 Pressure sensitivity index vs. $K_{\infty,5000}$.....28

Fig. 1.11 Pressure sensitivity index vs. porosity.....29

Fig. 1.12 Pressure sensitivity index vs. depth.....30

Fig. 1.13 Simple correlation coefficients of indicated variables with the pressure sensitivity index.ψ_{∞} Absolute values of the correlation coefficients are illustrated.....31

Fig. 1.14 Simple correlation coefficients of selected variables with the pressure sensitivity index ψ_{∞}.....32

Fig. 1.15 Measured pressure sensitivity index values vs. those predicted by one of the best of the correlations using two independent variables.....33

Fig. 1.16 Measured pressure sensitivity index values vs. those predicted by one of the best of the correlations using three independent variables.....34

Fig. 1.17 Measured pressure sensitivity index values vs. those predicted by one of the best of the correlations using four independent variables.....35

Fig. 1.18 Pressure sensitivity index vs. a linear combination calculated by linear regression on assorted core suite data.....36

Fig. 1.19 Pressure sensitivity index vs. a linear combination of variables.....37

Fig. 1.20 Pressure sensitivity index vs. a linear combination of variables with regression coefficients determined from Multi-Well core sample data.....38

Fig. 1.21 Pressure sensitivity index vs. another linear combination of variables with regression coefficients determined from Multi-Well core sample data.....39

Fig. 1.22 Pressure sensitivity index vs. still another linear combination of variables with regression coefficients determined from Multi-Well core sample data.....40

Fig. 1.23 Pressure sensitivity index vs. a linear combination of variables chosen using ridge regression.....41

Fig. 3.1 Apparatus used to flush cores with acetic acid.....59

Fig. 3.2 Configuration of core cut from whole core sample which contains a calcite-filled fracture.....60

Fig. 4.1 Relative humidity of air in equilibrium with aqueous solutions of sulfuric acid.....66

Fig. 4.2 Percent of pore space occupied by water vs. relative humidity of air that surrounds core.....67

Fig. 4.3 Percent of pore space occupied by water vs. relative humidity of air surrounding core.....68

Fig. 4.4 Percent of pore space occupied by water vs. relative humidity of air that surrounds core.....69

Fig. 4.5 Amount of sorbed heptane in an (MWX-1) 14-14 core sample before and after treatment by tetramethylammonium chloride.....70

Fig. 4.6 Effect of firing on adsorption-desorption iostherms of (MWX-2) 48-9 core material.....71

Fig. 5.1 Log-normal number distributions of simulated crack thicknesses and corresponding estimated crack thickness calculated from algebraic expressions derived for the no-branching model.....89

Fig. 5.2 Comparison of simulated estimate of crack thickness from gas slippage with the actual geometric mean for model of cracks connected in series.....90

Fig. 5.3 Representation of 242-bond rectuangular network.....91

Fig. 5.4 Representation of 200-bond rectangular network.....91

Fig. 5.5 Comparision of simulated estimates of crack thickness from gas slippage with the actual geometric and arithmetic means for two-dimensional network models. For both models, the simulated measurements provide good estimates of geometric mean.....92

Fig. 5.6 Comparison of simulated estimates of crack thickness from gas slippage with the actual geometric and arithmetic means for two-dimensional network models.....93

Fig. 5.7 Comparison of simulated estimates of crack thickness from purely viscous flow with the actual gemetric and arithmetic means for two-dimensional network models. For both models, the simulated measurements provide good estimates of the geometric mean.....94

Fig. 5.8 Comparison of simulated estimates of crack thickness from purely viscous flow with the actual geometric and arithmetic means for two-dimensional network models.....95

Fig. 5.9 Comparison of simulated estimates of crack thickness from gas slippage with the actual means for the 285-bond three-dimensional network model.....96

Fig. 5.10 Suite 2 samples (with high carbonate cement).....97

Fig. 5.11 Points represent actual values of Klinkengerg B factor vs. values predicted by Eq. 5.22 for five core samples at various temperatures and confining pressures.....98

Fig. 5.12 The relationship between C (in Eq. 5.23) and temperature and confining pressure.....99

Fig. A1.1 Permeability vs. net confining pressure for 6405 core sample (Group ID 1; depth 6405.0 ft; horizontal cut).....101

Fig. A1.2 Permeability vs. net confining pressure for 6405 core sample (Group ID 1; depth 6405.0 ft; vertical cut).....101

Fig. A1.3 Permeability vs. net confining pressure for 10570 S BETC core sample (Group ID 2; depth 10570.0 ft; horizontal cut).....102

Fig. A1.4 Permeability vs. net confining pressure for 10570 S BETC core sample (Group ID 2; depth 10570.0 ft; vertical cut).....102

Fig. A1.5 Permeability vs. net confining pressure
for Old Man Mountain #2 core sample
(Group ID 3; depth 4498.0 ft; horizontal cut).....103

Fig. A1.6 Permeability vs. net confining pressure
for Old Man Mountain #2 core sample
(Group ID 3; depth 4498.0 ft; vertical cut).....103

Fig. A1.7 Permeability vs. net confining pressure
for Ralston core sample
(Group ID 4; depth 3713.0 ft; horizontal cut).....104

Fig. A1.8 Permeability vs. net confining pressure
for Ralston core sample
(Group ID 4; depth 3713.0 ft; vertical cut).....104

Fig. A1.9 Permeability vs. net confining pressure
for BC-1-25 core sample
(Group ID 5; depth 7277.0 ft; horizontal cut).....105

Fig. A1.10 Permeability vs. net confining pressure
for PCUF31-13G core sample
(Group ID 6; depth 8493.0 ft; horizontal cut).....105

Fig. A1.11 Permeability vs. net confining pressure
for CIGE 21 core sample
(Group ID 7; depth 4403.3 ft; horizontal cut).....106

Fig. A1.12 Permeability vs. net confining pressure
for CIGE 21 core sample
(Group ID 7; depth 4403.3 ft; vertical cut).....106

Fig. A1.13 Permeability vs. net confining pressure
for CIGE 21 core sample
(Group ID 8; depth 8492.0 ft; horizontal cut).....107

Fig. A1.14 Permeability vs. net confining pressure
for CIGE 21 core sample
(Group ID 8; depth 8492.0 ft; vertical cut).....107

Fig. A1.15 Permeability vs. net confining pressure
for CIGE 21 core sample
(Group ID 9; depth 6503.0 ft; horizontal cut).....108

Fig. A1.16 Permeability vs. net confining pressure
for U78JP16 core sample
(Group ID 10; depth 8265.1 ft; horizontal cut).....108

Fig. A1.17 Permeability vs. net confining pressure
for U78JP36 core sample
(Group ID 11; depth 8262.3 ft; horizontal cut).....111

Fig. A1.18 Permeability vs. net confining pressure for U78JP36 core sample (Group ID 11; depth 8262.3 ft; vertical cut).....109

Fig. A1.19 Permeability vs. net confining pressure for Wilkin Ridge core sample (Group ID 12; depth 10298.7 ft; horizontal cut).....110

Fig. A1.20 Permeability vs. net confining pressure for Wilkin Ridge core sample (Group ID 12; depth 10298.7 ft; vertical cut).....110

Fig. A1.21 Permeability vs. net confining pressure for RBE-01 core sample (Group ID 13; depth 5863.6 ft).....111

Fig. A1.22 Permeability vs. net confining pressure for RBE-01 core sample (Group ID 14; depth 5898.5 ft) 111

Fig. A1.23 Permeability vs. net confining pressure for PTS 22-12 core sample (Group ID 17; depth 6403.0 ft).....112

Fig. A1.24 Permeability vs. net confining pressure for PTS 22-12 core sample (Group ID 18; depth 6431.0 ft).....112

Fig. A1.25 Permeability vs. net confining pressure for PTS 22-12 core sample (Group ID 19; depth 6509.6 ft).....113

Fig. A1.26 Permeability vs. net confining pressure for Mobil 45-14G core sample (Group ID 20; depth 5140.0 ft).....113

Fig. A1.27 Permeability vs. net confining pressure for Mobil 26-7G core sample (Group ID 21; depth 3309.0 ft).....114

Fig. A1.28 Permeability vs. net confining pressure for Mobil 26-7G core sample (Group ID 22; depth 2924.0 ft).....114

Fig. A1.29 Permeability vs. net confining pressure for OMM #2 Colo core sample (Group ID 23; depth 5457.0 ft).....115

Fig. A1.30 Permeability vs. net confining pressure for OMM #2 Colo core sample (Group ID 24; depth 5469.4 ft).....115

Fig. A1.31 Permeability vs. net confining pressure for Arco-Exxon L-36 core sample (Group ID 25; depth 3701.0 ft).....116

Fig. A1.32 Pemeability vs. net confining pressure for 3014-15 core sample (Group ID 26).....116

Fig. A1.33 Permeability vs. net confining pressure for (MWX-1) 42-25 core sample (Group ID 51; depth 6512.4 ft; vertical cut from bottom of whole core sample; nitrogen inlet pressure = 300 psig).....117

Fig. A1.34 Permeability vs. net confining pressure for (MWX-1) 31-32 core sample (Group ID 52; depth 5840.6 ft; horizontal cut from top of whole core sample; nitrogen inlet pressure = 350 psig).....118

Fig. A1.35 Permeability vs. net confining pressure for (MWX-1) 31-32 core sample (Group ID 52; depth 5840.6 ft; vertical cut from top of whole core sample; nitrogen inlet pressure = 350 psig).....118

Fig. A1.36 Permeability vs. net confining pressure for (MWX-1) 14-14 core sample (Group ID 53; depth 4917.0 ft; horizontal cut from top of whole core sample; nitrogen inlet pressure = 350 psig).....119

Fig. A1.37 Permeability vs. net confining pressure for (MWX-1) 14-14 core sample (Group ID 53; depth 4917.0 ft; vertical cut from top of whole core sample; nitrogen inlet pressure = 300 psig).....119

Fig. A1.38 Permeability vs. net confining pressure for (MWX-2) 48-9 core sample (Group ID 54; depth 5731.0 ft; horizontal cut; nitrogen inlet pressure = 350 psig).....120

Fig. A1.39 Permeability vs. net confining pressure for (MWX-2) 48-9 core sample (Group ID 54; depth 5731.0 ft; vertical cut; nitrogen inlet pressure = 350 psig).....120

Fig. A1.40 Permeability vs. net confining pressure for (MWX-2) 56-19 core sample (Group ID 55; depth 7878.7 ft; vertical cut; nitrogen inlet pressure = 350 psig).....121

Fig. A1.41 Permeability vs. net confining pressure for (MWX-2) 51-19 core sample (Group ID 56; depth 6529.0 ft; vertical cut from top of whole core sample; nitrogen inlet pressure = 350 psig).....121

Fig. A1.42 Permeability vs. net confining pressure for (MWX-2) 52-15 core sample (Group ID 57; depth 7133.8 ft; vertical cut from top of whole core sample; nitrogen inlet pressure = 350 psig).....122

Fig. A1.43 Permeability vs. net confining pressure for (MWX-2) 52-15 core sample (Group ID 57; depth 7134.0 ft; vertical cut from top of whole core sample; nitrogen inlet pressure = 350 psig).....122

Fig. A1.44 Permeability vs. net confining pressure for (MWX-2) 54-11 core sample (Group ID 58; depth 7267.5 ft; vertical cut from top of whole core sample; nitrogen inlet pressure = 350 psig).....123

Fig. A1.45 Permeability vs. net confining pressure for (MWX-2) 54-11 core sample (Group ID 58; depth 7268.1 ft; vertical cut from bottom of whole core sample; nitrogen inlet pressure = 350 psig).....123

Fig. A1.46 Permeability vs. net confining pressure for (MWX-2) 55-16 core sample (Group ID 59; depth 7362.2 ft; vertical cut from top of whole core sample; nitrogen inlet pressure = 350 psig).....124

Fig. A1.47 Permeability vs. net confining pressure for (MWX-2) 57-5 core sample (Group ID 60; depth 8109.7 ft; vertical cut from bottom of whole core sample; nitrogen inlet pressure = 350 psig).....124

Fig. A2.1 Ridge trace for combined data set (assorted, high carbonate, and Multi-Well cores) Variables 15, 19, and 21 are not very good predictors.....128

Fig. A2.2 Ridge trace for combined data set (assorted, high carbonate, and Multi-Well cores) Factors 2, 20, 22, and 27 are the least important of these nine factors when k = 1.....129

Fig. A2.3 Ridge trace for combined data set (assorted, high carbonate, and Multi-Well cores). Porosity and percent chert seem to be good predictors.....130

SUMMARY

This is the final report of a three-year project concerned with the pore structure of low permeability gas sands. The report is divided into five sections: 1) Pressure Sensitivity of Permeability, 2) Effects of Fluid, Confining Pressure, and Temperature on Absolute Permeabilities of Low Permeability Sandstones, 3) Effect of Acid Leaching and Presence of Fractures, 4) Adsorption, and, 5) Mathematical Modelling and Correlations.

In the first section, a data base of core properties is developed with measurements of permeability vs. confining pressure for three suites of cores as the main feature. The first suite to be studied, a suite of assorted core samples, was selected for its varied geologic character. A second suite of cores was chosen for their unusually high carbonate content. The third suite consisted of cores from the Multi-Well Test. Interrelationships between the measured variables were tested. Special attention was paid to correlation of core properties with pressure sensitivity derived from permeability vs. overburden relationships.

The second section reports a study of the dependency of absolute permeabilities of tight gas sands on temperature and confining pressure and the polarity of the fluid used in permeability measurement. Permeabilities could be highly sensitive to overburden pressure, but were found to be independent of temperature.

The third section describes an initial investigation into a) the effects of removing carbonate cement by leaching cores with acetic acid, b) the effects of calcite-filled fractures on permeability and pressure sensitivity. Dramatic increase in permeability and decrease in pressure sensitivity were observed to result from leaching. For cores containing calcite-filled fractures, it was found that the fracture was neither a permeability barrier to flow across the fracture or a highly conductive region for flow along the fracture.

Results presented in the fourth section on relationships between relative pressure and amount of adsorption provide careful information about the existence and extent of microporous material contained in tight gas sands. Results are interpreted in terms of pore size and as capillary pressures ranging from about 30 to 2000 atmospheres.

The fifth section on mathematical modelling presents results in which the diffusive contribution to flow is calculated for crack-shaped pores in series, and for two- and three-dimensional networks. The pore size estimated from Klinkenberg plots is compared with the pore-size distribution assumed for a given model. Evaluations of the Klinkenberg slip factors obtained from data in the present work are compared with those reported previously.

SECTION 1. PRESSURE SENSITIVITY OF PERMEABILITY

INTRODUCTION

Sensitivity of permeability to overburden pressure is often a key factor in formation evaluation of tight gas sands. Reductions in absolute gas permeabilities of more than an order of magnitude have been observed when overburden pressure is increased to typical formation values. One of the main objectives of this project was to carry out advanced core analyses on tight gas sandstones and in particular explain what structural features cause their permeabilities often to show marked sensitivity to overburden pressure. In previously reported work, the basic cause of pressure sensitivity was ascribed to high aspect ratio sheet pores that develop between grain boundaries.[1.1,1.2]

In order to learn more about the variation in pressure sensitivity that can occur from one core to another, measurements of relationships between permeability and confining pressure have been made on three suites of core samples, which will be referred to as Suites 1, 2, and 3. Suite 1, hereafter referred to as assorted cores, were selected for their varied geologic character (considering factors such as mineralogy, depth of burial, and burial history). Suite 2 is a set of cores which were selected for their high carbonate content, mainly because carbonate cement might have considerable influence on the sizes of pores which control flow. Suite 3 consists of cores obtained from the Multi-Well test.

Selection of a suitable quantitative measure of pressure sensitivity is far from straightforward. This problem is discussed in detail following consideration of the general character of permeability vs. confining pressure results. Finally, correlations of pressure sensitivity with some other conveniently measured core properties are shown.

MEASUREMENTS

Typical pressure sensitivity behavior of a low permeability core sample is shown in Fig. 1.1, in which permeability is plotted against confining pressure. Features shown by this plot include the large reduction in permeability when confining pressure is increased to several thousand psi and the failure of the sample to regain all of its initially measured permeability within a reasonably short time when the confining pressure is reduced.

Detailed studies were carried out on most core samples. These included: permeability vs. overburden pressure relationships for two cycles of loading and unloading at selected intervals of nominal confining pressure in the range of 500 to 5000 psi (results for the three suites of

cores are presented in Appendix 1); determination of Klinkenberg permeabilities; estimates of pore size from gas slippage; mineral analyses from thin sections; porosity; and surface areas from gas adsorption.

In addition to routine measurements, more specialized observations were made on some of the samples. These included: scanning electron microscopy of core samples and their resin pore casts; grain size distributions from scanning electron micrographs and sieve analysis; surface areas from a novel hydrogen-deuterium exchange method; estimates of effective areas of sheet pores from cross-sections given by electron micrographs of pore casts, grain size, fluid flow properties, and pore size; and clay identification from electron microscopy and, if sufficient sample was available, analysis by x-ray diffraction.

RESULTS

Suite 1 - Assorted Core Samples

The Suite 1 cores showed pressure sensitivities from less than 30% to over 90% reduction in Klinkenberg permeability when confining pressure was increased from 500 to 5000 psi on first loading. Detailed results have been reported.[1.1] Recent work has been concerned with attempting to identify factors related to pressure sensitivity and to test for correlations that are more general than those found[1.1] for Suite 1 alone.

Suite 2 - Cores High in Carbonate Cement

Presence of carbonates was indicated to be a factor in determining pressure sensitivity both by some of the correlations and by consideration of how carbonate cement may affect pore structure. A second suite of core samples, selected for their high carbonate cement content, was therefore tested. Results are summarized in Table 1.1. These cores generally have very low porosities and permeabilities and show extreme sensitivity to overburden pressure for first loading. Sensitivities given by second loading are, when measurable, less extreme, but do cover a wider range than seen for other systems. Results generally demonstrate that presence of carbonates can be associated with unusually low porosities and marked sensitivity of permeability to confining pressure. Constituents determined by mineral analysis from thin section are listed in Table 1.2.

Suite 3 - Multi-Well Core Samples

A large number of cores have been obtained from the Multi-Well Test Site, section 34, township 6-S, range 94-W, Garfield County, Colorado. A number of the cores tested to date have permeabilities which are strongly sensitive to overburden pressure and are therefore of special interest with respect to the main objective of the project: determining the

relationship between pore structure and permeability. Permeabilities to gas down to about 2 microdarcies at 500 psi overburden pressure have been observed for dry cores. Results are presented in Table 1.3. Further measurements of relationships between permeability and overburden pressure for Multi-Well samples are being made. A list of Multi-Well core material now in hand is presented in Table 1.4.

CORRELATIONS INVOLVING INDIVIDUAL VARIABLES

Several interesting correlations for the three suites of cores were found. Fig. 1.2 is a plot of percent porosity against the depth (in feet) of the core sample. A distinct trend of decreasing porosity with increasing depth is seen for the assorted core samples. However, the Multi-Well samples are clustered near the center of the plot and do not show any distinct trend. Most of the high carbonate samples are distinguished by their low porosities. This plot shows a clear separation of the assorted core samples from the high carbonate samples. There is some overlap of each of those two suites with the points given by the Multi-Well samples.

Fig. 1.3 shows a plot of percent porosity against percent total carbonate. As expected, most of the samples of the high carbonate suite are separated from the other samples in this plot. However, two of the Multi-Well samples also have relatively high carbonate content. For the samples of the high carbonate suite, there is a noticeable decrease in porosity with increase in total carbonate.

In Fig. 1.4, $K_{\infty,5000}$, the Klinkenberg permeability (in md) at 5000 psi nominal confining pressure on first loading, is plotted against percent porosity. All of the samples considered together show the expected trend of increasing $K_{\infty,5000}$ with increasing porosity. This general trend is apparent in the assorted core and high carbonate suites considered separately, but less obvious with the Multi-Well samples.

Fig. 1.5 shows a plot of visible porosity (percent) observed in thin section vs. porosity (percent) measured by laboratory techniques such as: (1) saturating with distilled water and weighing, and (2) using a helium porosimeter. In almost all cases, the visible porosity from thin section is less than the porosity determined by the other laboratory techniques. For the 34 samples for which the former quantity was determined, the average visible porosity from thin section is only 3.4 percent, compared with an average of 6.8 percent for the porosity determined by other laboratory techniques. Possible reasons for this difference may be incomplete penetration of the resin and incorrect estimates due to exclusion of porosity given by sheet pores and microporosity.

Percent of sodium feldspar (determined from thin section) is plotted against the depth (in feet) in Fig. 1.6. A noticeable trend of decreasing sodium feldspar with increasing depth is seen for both the assorted core

and the Multi-Well suites of cores. It is thought that this trend could reflect a tendency toward greater total loss of sodium feldspar via pressure solution with increasing depth. However, no apparent trend relating amount of sodium feldspar with depth is seen for the cores of the high carbonate suite.

In Fig. 1.7, the Klinkenberg permeability (in md) at 5000 psi nominal confining pressure on first loading is plotted against percent sodium feldspar. On first inspection, there appears to be a trend of increasing permeability with increasing sodium feldspar. However, this trend may possibly be a manifestation of the relationship of both of these variables to depth. This point helps focus on a recurring problem: when there are intercorrelations among the variables, how much of a given effect can be attributed to a given variable?

SELECTION OF A MEASURE OF SENSITIVITY OF PERMEABILITY TO CONFINING PRESSURE

In attempting to find correlations between pressure sensitivity and other measured core properties, the general problem of providing satisfactory characterization of pressure sensitivity must first be addressed.

The typical character of relationships between permeability and confining pressure for a sample that has stood, generally for at least several weeks, at ambient conditions is shown in Fig. 1.1. First loading results exhibit the greatest pressure sensitivity. Upon first unloading, the original permeability at 500 psi is not recovered, although slow increase in permeability for periods of several days can be detected for a sample held at 500 psi. After first loading, subsequent cycles of loading and unloading give quite closely reproducible relationships between permeability and overburden pressure. Hysteresis in the loading and unloading curves is fairly minor. This behavior was found to be characteristic of practically all tested samples. Thomas and Ward[1.3] reported that the first loading curve could be repeated if the core were allowed to stand at ambient conditions for 3 to 6 weeks or for a shorter time if the core is stored at 70°C. Vairogs et al[1.4] reported that the extent to which first loading permeability was recovered after 43 days varied with the particular core sample. Also, the extent of permeability recovery on unloading varied according to the amount to which the core was loaded on first loading. Thus, choice of a quantitative measure of sensitivity of permeability to confining pressure is not obvious and must necessarily be somewhat arbitrary.

It has been observed that most of the reduction in permeability occurs with increase in confining pressure to 4000 psi.[1.3,1.4] In the present work, the effect of a 10-fold variation in nominal confining pressure was obtained with variation being from 500 psi to 5000 psi. Measurements of gas permeability were made for first loading from 500 to

5000 psi at selected intervals. First unloading, second loading, and second unloading curves were also determined.

Fig. 1.8 illustrates sensitivities of core samples to confining pressure. $K_{\infty,500}$, the Klinkenberg permeability exhibited at a nominal confining pressure of 500 psi on first loading, is plotted against $K_{\infty,5000}$, the corresponding quantity at 5000 psi, also on first loading. If the Klinkenberg permeability of any sample at 500 psi were equal to that at 5000 psi, then the point representing that sample would lie on the solid line. The distance of a point above the solid line indicates the sensitivity of that sample's permeability to confining pressure. It is seen that samples having lower permeabilities tend to be more sensitive to confining pressure. Also, the sensitivities seem to display more scatter among samples having lower permeabilities.

Early in the present work, the ratio of Klinkenberg permeability at 500 psi nominal confining pressure to that at 5000 psi for first loading was used as an estimate of pressure sensitivity, and correlations were sought between this ratio and other measurable core properties in an attempt to identify the factors which can cause wide variation in sensitivity from one core sample to another. However, because of the long-term stress relaxation effects, first loading data are particularly sensitive to previous stress history.

Permeability vs. confining pressure curves given by cycling the confining pressure indicate that the first unloading, second loading, and second unloading curves are quite similar, with hysteresis between unloading and loading being quite small. Therefore, it appeared that any one of these changes in stress condition would be reasonably consistent. It was decided to use first unloading data to obtain a measure of pressure sensitivity.

Plots of the logarithm of permeability vs. the logarithm of confining pressure for first unloading gave a series of points that largely followed linear relationships. (Jones and Owens[1.5] noted that similar plots for first loading gave fairly linear relationships for confining pressures greater than 2000 psi.) The absolute value, ψ, of the slope (which was always negative) given by

$$\log K = -\psi \log P + C_o \qquad (1.1)$$

was used to define a measure of sensitivity. (C_o is a constant for a given set of data.) In initial tests on the assorted core samples and some of the Multi-Well samples, Klinkenberg plots were not prepared for first unloading at 500 psi, and initial data treatment used total confining pressure for P and K_p for K. In order to achieve consistency in the way results were treated overall, values of K_∞ at net confining pressure P were estimated. Several possible approaches to estimating K_∞ were considered. The method adopted involved using a relationship between Klinkenberg B factors and K_∞ values similar to those reported by Jones and Owens[1.5] and Heid et al.[1.6] These relationships were of the form

$$K_\infty = \frac{K_p}{1 + CK_\infty^{\,n}/P_m} \qquad (1.2)$$

Some of the best quality data (as indicated by the straightness of Klinkenberg plots) obtained here provided the estimates C = 0.432 and n = -0.357. Those values were used to estimate K_∞ iteratively from the equation,

$$K_{\infty,j+1} = \frac{K_p}{1 + 0.432\ K_{\infty,j}^{\,-0.357}/P_m} \qquad (1.3)$$

where $K_{\infty,j}$ is the jth estimate of K_∞, $K_{\infty,j+1}$ is the (j+1)st estimate of K_∞, and K_p is the measured permeability (in md) to gas at a mean pressure of P_m atmospheres.

Several tests based on comparison of measured and estimated values of K_∞ showed this approach to be reasonable. Pressure sensitivities ψ_∞ given by absolute values of slopes obtained for log of K_∞ estimated in this way vs. log of NET confining pressure are compared with corresponding values ψ_∞ obtained for log of K_p vs. log of TOTAL confining pressure in Fig. 1.9. This figure shows that differences resulting from applying this standardizing correction are small. This fact, combined with results of other tests, suggests that the procedure is satisfactory.

For the remainder of this report, PRESSURE SENSITIVITY INDEX, ψ_∞, is used to refer to the absolute value of the slope of log K_∞ (estimated) vs. log P, where P is the mean net confining pressure.

CORRELATIONS INVOLVING PRESSURE SENSITIVITY AND SINGLE VARIABLES

The pressure sensitivity index, defined above, shows some correlations with some individual variables. For example, as the Klinkenberg permeability at a nominal confining pressure of 5000 psi decreases, the pressure sensitivity index tends to increase. This is shown in Fig. 1.10. Further, it is seen that there tends to be more scatter in pressure sensitivity index values as permeability decreases. The assorted core samples considered by themselves also follow the general pattern described for the combined data set. However, it is difficult to perceive any general trend for either the high carbonate core samples considered separately or the Multi-Well samples considered separately.

Similar behavior is observed by pressure sensitivity index vs. percent porosity data, which are plotted in Fig. 1.11. The overall trend, which is also exhibited by the assorted core samples considered separately, is for the pressure sensitivity index to increase and to exhibit more scatter as porosity decreases. However, if the high carbonate suite or the Multi-Well suite is considered separately, it is difficult to perceive a trend.

The pressure sensitivity index is plotted against depth in feet in

Fig. 1.12. When all of the samples are considered together without regard to origin, there appears to be no clear trend. However, some interesting conclusions can be inferred by considering each suite separately. Assorted core samples show a clear trend of increasing pressure sensitivity index with increasing depth. On the other hand, Multi-Well samples tend to exhibit decreasing pressure sensitivity with increasing depth. While it is hard to detect any general trend among the high carbonate samples, they are clearly more sensitive to confining pressure than the assorted core samples obtained from comparable depths.

As a simple test for possible trends in the combined data of all three core suites, correlation coefficients (r) between the pressure sensitivity index and other single variables were calculated using the combined data. (In these calculations, each core plug was considered to be a separate sample, even when more than one core plug was taken from the same whole core.) The magnitudes of simple correlation coefficients of the pressure sensitivity index with a number of variables, taken one at a time, are illustrated by the lengths of bars in Fig. 1.13. Each bar extending to the left of the vertical line indicates negative correlation, that is, the pressure sensitivity index tends to decrease as the variable increases. A bar extending to the right of the vertical line indicates positive correlation, that is, the pressure sensitivity index tends to increase as the variable increases.

For predicting the pressure sensitivity index, porosity ($r = -0.68$) seems to be the most important single variable of those investigated in this work. However, pressure sensitivity has been ascribed to the presence of high aspect ratio sheet pores at grain boundaries.[1,2] The pore volume of these sheet pores is estimated to be only a small fraction of the total porosity. The sheet pores become compressed under the action of confining pressure. The most extensive compressibility data for tight sands show that while permeability may be reduced about 10-fold, the corresponding reduction in porosity is only 1/10.[1,5] It seems likely that much of the variation in porosity from one specimen to another is due to variation in the amount of solution porosity. However, the crack pore space is more important in determining pressure sensitivity. It is expected that increase in solution porosity would tend to decrease the pressure sensitivity by providing more opportunities for the fluid to avoid flowing through cracks. It may be that this effect is responsible for at least part of the observed tendency of the pressure sensitivity index to decrease when the overall porosity increases.

One of the specialized measurements, total crack length (cm) per square cm in SEM of pore casts generates the next highest value of $|r|$ with the pressure sensitivity index. The value of 0.59 for r suggests that greater total crack lengths per unit area of SEM are associated with greater sensitivities of permeability to confining pressure. Although this specialized SEM measurement was made for only a relatively small number of samples (all of which were in the assorted cores suite), and experimental difficulties may have allowed some cracks to escape detection, this calculated value of r lends support to the association of sensitivity of permeability to overburden pressure with the presence of crack-shaped pores of high aspect ratio.

The two quantities ranking next in importance (based on $|r|$) are both Klinkenberg permeabilities -- one at 500 psi nominal confining pressure ($r = -0.57$) and one at 5000 psi nominal confining pressure ($r = -0.54$). Both of these permeabilities were determined on first loading. The negative values for r indicate that sensitivity of permeability to confining pressure tends to increase as permeability decreases, whether the permeability is measured at low or high confining pressure. This trend when Klinkenberg permeability is measured at high confining pressure is also seen in Fig. 1.10.

It is interesting to note that the ratio $K_{\infty,500}/K_{\infty,5000}$ (first loading) gives a value of $|r|$ (with the pressure sensitivity index) smaller than either of those Klinkenberg permeabilities alone. This ratio was considered as a measure of sensitivity of permeability to overburden pressure in an early stage of the present work, but is seen to rank only fifth in ability to correlate with the pressure sensitivity index. This relatively poor showing is partly due to using the ratio itself, instead of its logarithm, to correlate with a quantity that was derived from log-log data. As expected, the pressure sensitivity index does tend to increase as this ratio increases ($r = 0.53$).

Percent of sodium feldspar ranks sixth among the 19 quantities, and first among the nine quantities provided by thin section analysis, in correlating ability. The r value of -0.50 suggests some tendency for the pressure sensitivity index to decrease as the percent of sodium feldspar increases. The percent of sodium feldspar is also correlated with other quantities, including Klinkenberg permeability at 500 psi ($r = 0.80$), Klinkenberg permeability at 5000 psi ($r = 0.74$), and percent porosity ($r = 0.60$). Therefore, it is appropriate to consider the possibility that the apparent negative correlation of sodium feldspar with the pressure sensitivity index is a manifestation of the relationship of both of these variables to permeability and porosity.

Visible porosity from thin section ranks seventh ($r = -0.40$) among the 19 quantities in correlating ability. This rather weak correlating ability contrasts with the good correlating ability of porosity measured by other laboratory techniques ($r = -0.68$; see above).

For some of the variables listed in Fig. 1.13, including permeabilities and the ratio of permeabilities, it is believed that correlation with logarithms of these quantities might be more appropriate. For example, using logarithms of permeabilities would avoid giving excessively high importance to relatively high permeability samples. However, if logarithms of percentages obtained from thin section were used, some samples would have to be disregarded for a given correlation if any of the percentages appearing in that correlation is zero. Such systematic discarding of values at one end of the range would be a disadvantage when searching for trends. In Fig. 1.14, correlation coefficients are plotted for the seven highest ranking variables listed in Fig. 1.13. However, for Fig. 1.14, logarithms of the Klinkenberg permeabilities and their ratio are used with previously mentioned correlation coefficients for the other four variables to obtain what seems

to be a more meaningful ranking. This ranking is shown in Fig. 1.14, with the largest $|r|$ at the top.

In summary, although plotting the pressure sensitivity index against single variables shows some interesting trends, there appears to be too much variation for such a plot to be valuable for more than approximate prediction of pressure sensitivity. Therefore, the predictive power of combinations of variables was investigated.

EMPIRICAL CORRELATIONS BETWEEN CORE PROPERTIES AND SENSITIVITY TO OVERBURDEN PRESSURE

Some empirical relationships have been found to give reasonably good agreement when comparing experimental vs. predicted pressure sensitivity index. The pressure sensitivity index, based on first unloading as described above, was used as the dependent variable.

Combinations of two variables selected from the "independent" variables listed in Table 1.5 were used in multiple linear regression, which was performed with the help of the International Mathematical and Statistical Library (IMSL) subroutines BECOVM and RLMUL. Each cut from the same whole core was considered a separate sample when performing regression, although some values (including mineral composition and porosity percentages from thin section) were determined only once and were assumed to apply to the given whole core. Inspection of results for a combined data set comprising data for all three suites of core samples confirmed that porosity plays a major role in correlation of pressure sensitivity: most of the best correlations using two independent variables include porosity as one of the variables. In Fig. 1.15, actual pressure sensitivity index values are compared with those predicted by a linear combination of percents porosity and total carbonate. The rather strong negative correlation between the latter two variables led to the sign of the coefficient of percent total carbonate being negative, even though there is a positive correlation ($r = 0.24$; see Fig. 1.13) between percent total carbonate and the pressure sensitivity index. The total sum of squares of 45 residuals (42 degrees of freedom) was 2.235.

In a similar manner, combinations of three variables selected from the same set were used in multiple linear regression. One of the best resulting correlations involved the same two variables and also depth in feet. Actual pressure sensitivity index values are compared with those predicted by this correlation in Fig. 1.16. It is seen that adding a third variable to the linear combination leads to some improvement in the predictive ability. Further, the total sum of squares of 45 residuals (41 degrees of freedom) decreased to 1.968.

Combinations of four variables selected from the same set were also tested using multiple linear regression. Again, combinations that statistics indicated to be among the best were inspected. Combinations

were disregarded if they almost amounted to using the pressure sensitivity to predict the pressure sensitivity index, e.g., combinations containing crack thicknesses at both 500 and 5000 psi (variable numbers 26 and 27) or Klinkenberg permeability at 5000 psi and crack thickness at 500 psi (variable numbers 8 and 26). Remaining ones of the seemingly best combinations were used to generate plots of actual vs. predicted pressure sensitivity index. Such plots illustrated the degree of success of combinations of variables in predicting pressure sensitivity. One of the best predictors was a combination of the three variables indicated in the preceding paragraph (percents porosity and total carbonate and depth in feet) and percent matrix. However, the addition of a fourth variable (percent matrix) led to only slight improvement in predictive value (see Figs. 1.16 and 1.17). The total sum of squares of 45 residuals (40 degrees of freedom) decreased by only 5.5% (to 1.860).

An example of the results obtained by another approach is shown in Fig. 1.18. Here, only data from the suite of assorted cores (these were the first data to be obtained and tested) were used to obtain a linear combination of variables for use as a predictor. Then this predictor was tested on cores from all three suites. The solid line in Fig. 1.18 shows where the points would lie if there were perfect agreement between the actual and predicted values of the pressure sensitivity index. The indicated linear combination of depth and percents of chert, lithic fragments (not including chert), and matrix predict pressure sensitivity of assorted core samples rather well. However, pressure sensitivity behavior exhibited by the other two suites appears similar to that illustrated in the pressure sensitivity index vs. depth plot in Fig. 1.12. Once again, the trend displayed by Multi-Well samples in Fig. 1.18 is in the opposite direction from that of assorted cores. Again, it is hard to detect any general trend among the high carbonate samples, but it is apparent that they tend to be more sensitive to confining pressure than the assorted core samples having comparable values for the linear combination used as the abscissa.

The correlation (also obtained by treating results from assorted cores) chosen for illustration in Fig. 1.19 is NOT one of the best for assorted cores. However, this linear combination does show a separate trend for the high carbonate samples.

Fig. 1.20 illustrates the predictive ability of a correlation obtained for Multi-Well core samples. This correlation also held rather well for most of the high carbonate cores. As shown in Fig. 1.20, the points for the three high carbonate cores for which this correlation does not predict well are grouped together in this actual vs. predicted pressure sensitivity index plot. This correlation was very poor for the suite of assorted cores and is not shown.

Also illustrated (see Figs. 1.21 and 1.22) are results from two more combinations that are among the most successful in predicting the pressure sensitivity index for Multi-Well core samples only. However, neither of these combinations work well for the other two (assorted and high carbonate) sample sets.

Results given by another combination are illustrated in Fig. 1.23. In this approach, a data base including measurements for core samples of all three suites was used to determine the linear combination of variables for use as a predictor of pressure sensitivity. Ridge regression[1.7,1.8] (see Appendix 2) was used to provide a guide in the selection of variables. The predicted pressure sensitivity index agrees reasonably well with the actual pressure sensitivity index for samples from all three suites.

PHYSICAL SIGNIFICANCE OF EMPIRICAL CORRELATIONS

The absolute values of coefficients used in linear combinations indicated in Figs. 1.15-1.23 are, of course, largely determined by the range of values exhibited by the variables which the coefficients multiply. For example, the absolute value of the coefficient of depth given in feet tends to be a very small number. Also, one should be careful not to attach too much physical significance to individual values of coefficients in linear combinations of variables, even when these combinations produce good correlations between predicted and experimental pressure sensitivities. As indicated by Hoerl and Kennard,[1.8] intercorrelations between variables can sometimes even lead to estimates having the wrong sign with respect to what might be expected from physical considerations.

CONCLUSIONS

1. The pressure sensitivity of low permeability sandstones has a dependency on detailed pore structure which is not likely to be revealed by macroscopic core properties. While, as expected, no strong correlations were obtained, a number of significant trends were observed.

2. Properties of the assorted core samples of varied geologic origin could be correlated with their pressure sensitivity with relative ease. An important contributing factor in the correlation was a trend of decreasing porosity with increasing depth. This trend was not shared by the Multi-Well and high carbonate samples and is ascribed, in part, to somewhat fortuitous selection of samples.

3. For the high carbonate suite, porosity decreased with increase in total carbonate. Presence of high percentages of carbonates was associated with unusually low porosities and marked sensitivity of permeability to confining pressure.

4. All of the samples considered together show a trend of increasing Klinkenberg permeability with increasing porosity.

5. In almost all cases, the visible porosity from thin section is less than the porosity determined by other laboratory techniques.

6. A noticeable trend of decreasing sodium feldspar with increasing depth is seen for both the assorted core and the Multi-Well suites of cores. This trend may reflect a tendency toward greater total loss of sodium feldspar via pressure solution with increasing depth. There also appears to be a trend of increasing permeability with increasing sodium feldspar. However, the correlations of sodium feldspar with some other variables hinder making a simple inference of the role of sodium feldspar.

7. Because of long-term stress relaxation effects, first loading data are particularly sensitive to previous stress history. After first loading, subsequent cycles of loading and unloading give quite closely reproducible relationships between permeability and overburden pressure, with hysteresis in the loading and unloading curves being fairly minor.

8. A typical plot of the logarithm of permeability vs. the logarithm of confining pressure for first unloading gives a series of points that largely follow a linear relationship. The absolute value of the slope (which was always negative) of the logarithm of K_∞ (which was estimated iteratively) vs. the logarithm of the mean net confining pressure can be used to define a pressure sensitivity index. This measure of pressure sensitivity correlated well with some other possible measures of pressure sensitivity, including the logarithm of $(K_{\infty,500}/K_{\infty,5000})$.

9. The pressure sensitivity index showed several correlations with routinely measured variables, the more significant being as follows: overall, the pressure sensitivity tends to increase with decrease in K_∞, porosity, or sodium feldspar and with increase in total crack length per unit area in SEM of pore casts.

10. Some empirical relationships that use linear combinations of variables have been found to possess reasonably good correlating ability. Porosity seemed to be important in correlating pressure sensitivity behavior, both when porosity was considered alone and when used in combination with other variables. Often empirical relationships obtained for one suite of cores would not hold for the other two suites.

11. Intercorrelations among the variables often affected estimates of the regression coefficients. Thus, one should be careful not to attach too much physical significance to individual values of coefficients in linear combinations of variables, even when these combinations produce good correlations between predicted and experimental pressure sensitivities.

12. Ridge regression can be used to enable selection of a set of independent variables that are not too highly correlated with each other. Although ridge regression enabled selection of two rather well-behaved combinations of variables, their predictive performances were not significantly better than those arrived at by linear regression.

13. Future work aimed at obtaining a more quantitative account of pressure sensitivity should involve detailed examination of pore structure and its relationship to permeability vs. overburden pressure relationships. Particular attention will be given to explaining anomalous behavior, exhibited by some samples with respect to trends established by other samples.

REFERENCES

1.1 Morrow, N.R., Brower, K.R., and Kilmer, N.H., "Relationship of Pore Structure to Fluid Behavior in Low Permeability Gas Sands," 1982 Annual Technical Report to the U.S. Department of Energy, Report No. DOE/BC/10216-14, in press.

1.2 Brower, K.R. and Morrow, N.R., "Fluid Flow in Cracks as Related to Low Permeability Gas Sands," SPE 11623, presented at SPE/DOE Joint Symposium on Low Permeability Gas Reservoirs, Denver, CO, March 14-16, 1983 (to appear in Soc. Pet. Eng. J., April 1985).

1.3 Thomas, R.D. and Ward, D.C., "Effect of Overburden Pressure and Water Saturation on Gas Permeability of Tight Sandstone Cores," J. Pet. Tech. (February 1972) 120-124.

1.4 Vairogs, J., Hearn, C.L., Dareing, D.W., and Rhoades, V.W., "Effect of Rock Stress on Gas Production from Low-Permeability Reservoirs," J. Pet. Tech. (September 1971) 1161-1167.

1.5 Jones, F.O. and Owens, W.W., "A Laboratory Study of Low Permeability Gas Sands," SPE 7551, Proceedings: SPE-AIME Symposium on Low-Permeability Gas Reservoirs, Denver, CO, May 20-22, 1979, 325-334.

1.6 Heid, J.G., McMahon, J.J., Nielsen, R.F., and Yuster, S.T., "Study of the Permeability of Rocks to Homogeneous Fluids," Drilling and Production Practice (1950) 230-246.

1.7 Hoerl, A.E. and Kennard, R.W., "Ridge Regression: Biased Estimation for Nonorthogonal Problems," Technometrics 12, No. 1 (1970) 55-67.

1.8 Hoerl, A.E. and Kennard, R.W., "Ridge Regression: Applications to Nonorthogonal Problems," Technometrics 12, No. 1 (1970) 69-82.

Table 1.1 Results for Suite 2 Samples (High in Carbonate Cement)

Group ID	Origin ID	Depth (feet)	Percent Porosity	$K_{\infty,500}$ (md), first loading	$K_{\infty,5000}$ (md), first loading	$\frac{K_{\infty,500}}{K_{\infty,5000}}$, first loading	Pressure Sensitivity Index	
13	RBE-01	5863.6	4.903	0.0232	0.00054	43.2	1.311	(PC)
14	RBE-01	5898.5	4.13	0.0129	0.00016	80.0	0.982	(PC,SEM)
15	RBE-01	6923.3	2.03	<0.0034	a			(PC)
16	RBE-01	7743.2	3.30	0.0003	a			(PC)
17	PTS 22-12	6403.0	4.90	0.0635	0.0013	49.3	1.162	(PC)
18	PTS 22-12	6431.0	2.90	0.0137	0.00036	38.2	1.150	(PC,SEM)
19	PTS 22-12	6509.6	2.37	0.0103	0.00010	105.3	0.588	(PC)
20	Mobil 45-14G	5140.0	6.95	0.0451	0.0028	16.1	0.747	(PC,SEM)
21	Mobil 26-7G	3309.0	4.82	0.0873	0.0084	10.4	0.782	(PC)
22	Mobil 26-7G	2924.0	3.23	0.0108	0.00022	49.7	0.872	(PC)
23	OMM #2 Colo	5457.0	7.06	0.0299	0.0022	13.4	0.621	(PC,SEM)
24	OMM #2 Colo	5469.4	2.69	0.0037	0.00010	36.2	0.642	(PC)
25	Arco-Exxon L-36	3701.0	3.42	0.0121	0.00034	35.3	0.609	(PC)
26	3014-15		4.62	0.0190	0.0019	10.0	0.618	(PC,SEM)

OMM = Old Man Mountain
K_{∞} refers to Klinkenberg permeability
PC indicates that a pore cast has been made
SEM indicates that scanning electron micrographs have been made

a - no measurable flow

Table 1.2 Constituents of High Carbonate Core Samples Determined by Mineral Analysis from Thin Section

Origin ID	Depth	Q	PF	KF	CH	LT	CT	M	V	O
RBE-01	5863.6	46	5	3	19	8	13	1	2	3
RBE-01	5898.5	31	9	4	10	12	29	--	--	5
RBE-01	6923.3	34	9	--	10	8	40	--	--	--
RBE-01	7743.2	siltstone								
PTS 22-12	6403.0	38	4	3	16	7	23	--	4	3
PTS 22-12	6431.0	37	5	1	14	5	34	1	1	2
PTS 22-12	6483.0	siltstone								
PTS 22-12	6509.6	17	3	6	22	6	43	--	--	3
OMM #2 Colo	5457.0	48	8	--	11	8	11	8	5	4
OMM #2 Colo	5469.4	35	7	--	4	9	40	3	--	3
Mobil 26-7G	2924.0	42	4	--	8	8	29	--	--	8
Mobil 26-7G	3309.0	54	3	--	6	7	25	--	3	1
Mobil 45-14G	5141.0	44	5	--	6	12	25	1	3	3
Arco-Exxon L-36	3701.0	27	9	--	10	8	35	4	--	7

Q - quartz
PF - Na-feldspar
KF - K-feldspar
CH - chert
LT - total lithics less chert
CT - total carbonate
M - matrix
V - visible porosity
O - other

Table 1.3 Results for Multi-Well Samples

Group ID	Origin ID	BET Surface Area (m^2/g)	Depth (feet)	Geologic Zone	Cut* Direction	Location in Whole Core	% Porosity	$K_{\infty},500$ (md), first loading	$K_{\infty},5000$ (md), first loading	$\frac{K_{\infty},500}{K_{\infty},5000}$, first loading	Pressure Sensitivity Index
51	(MWX-1) 42-25	1.545	6511.7	CO		Top	7.73				
51	(MWX-1) 42-25	2.650	6512.4	CO	V	Bottom	7.92	0.01453	0.00112	12.9	0.731
52	(MWX-1) 31-32	1.063	5840.6	FP	H	Top	5.77	0.01680	0.00089	19.0	0.940
52	(MWX-1) 31-32	1.063	5840.6	FP	V	Top	5.44	0.01262	0.00065	19.4	1.044
52	(MWX-1) 31-32	1.270	5841.0	FP		Bottom					
53	(MWX-1) 14-14	2.427	4917.0	FM	H	Top	7.00	0.1657	0.00926	17.9	0.994
53	(MWX-1) 14-14	2.427	4917.0	FM	V	Top	7.99	0.08327	0.00531	15.7	0.985
53	(MWX-1) 14-14		4917.9	FM		Bottom					
54	(MWX-2) 48-9	2.335	5731.0	FP	H		8.52	0.04223	0.00421	10.0	0.844
54	(MWX-2) 48-9	2.335	5731.0	FP	V		8.31	0.03364	0.00129	26.1	1.065
55	(MWX-2) 56-19	2.200	7878.7	SH	V		6.97	0.00230	0.00014	16.6	0.660
56	(MWX-2) 51-19	1.278	6529.0	CO	V	Top	7.52	0.01223	0.00156	7.8	0.655
57	(MWX-2) 52-15	2.427	7133.8	PAL	V	Top	9.69	0.00997	0.00360	2.8	0.360
57	(MWX-2) 52-15		7134.0	PAL	V	Bottom	9.83	0.00219	0.00070	3.1	0.447
58	(MWX-2) 54-11	2.941	7267.5	PAL	V	Top	7.49	0.00435	0.00032	13.7	0.475
58	(MWX-2) 54-11		7268.1	PAL	V	Bottom	7.53	0.00510	0.00070	7.3	0.442
59	(MWX-2) 55-16	3.581	7362.2	PAL	V	Top	7.21	0.00173	0.00024	7.1	0.413
60	(MWX-2) 57-5	1.517	8109.7	SH	V	Bottom	5.71	0.00216	0.00022	9.6	0.505

* H = Horizontal; V = Vertical

K_{∞} refers to Klinkenberg permeability.

Key to Geologic Zone:

CO = Coastal
FM = Fluvial (meander belts)
FP = Fluvial (point bars)
PAL = Paludal
SH = Shoreline/Marine

Table 1.4 Multi-Well Samples on Hand

Well	ID	Depth (feet)	Geologic zone	Date received
(MWX-1)	42-25	6511.7 - 6512.4	CO	
(MWX-1)	31-32	5840.6 - 5841.0	FP	
(MWX-1)	14-14	4917.0 - 4917.9	FM	
(MWX-2)	48-9	5731.0	FP	
(MWX-2)	56-19	7878.7	SH	February, March,
(MWX-2)	51-19	6529.0	CO	and May, 1982
(MWX-2)	52-15	7133.8 - 7134.0	PAL	
(MWX-2)	54-11	7267.5 - 7268.1	PAL	
(MWX-2)	55-16	7362.2	PAL	
(MWX-2)	57-5	8109.7	SH	
(MWX-1)	3-11	4319.4 - 4320.4	PAR	
(MWX-1)	3-21	4308.3 - 4309.1	PAR	
(MWX-1)	8-16	4548.4 - 4548.9	FM	
(MWX-1)	10-13	4699.7 - 4700.5	FM	October, 1982
(MWX-1)	13-15	4851.0 - 4851.5	FM	
(MWX-1)	22-20	5357.2 - 5357.7	FP	
(MWX-1)	29-24	5725.7 - 5726.6	FP	
(MWX-2)	17-22	4937.0 - 4937.8	FM	
(MWX-2)	47-34	4915.5 - 4916.6	FM	
(MWX-1)	14-24A	4917.9 - 4918.2	FM	February, 1983
(MWX-1)	14-24B	4918.2 - 4918.9	FM	
(MWX-1)	13-18	4846.5 - 4847.0	FM	
(MWX-1)	16-11	5034.8 - 5035.2	FM	
(MWX-1)	21-4A	5271.6 - 5272.0	FP	March, 1983
(MWX-1)	29-31	5730.9 - 5731.2	FP	(fractured samples)
(MWX-1)	29-7B	5733.2 - 5733.6	FP	
(MWX-1)	34-10	6002.3 - 6002.5	CO	
(MWX-1)	38-27	6192.6 - 6193.0	CO	
(MWX-3)	58-14	4918.1 - 4918.7	FM	
(MWX-3)	60-19	5726.3 - 5726.8	FP	August, 1983
(MWX-3)	63-16	5832.1 - 5832.6	FP	
(MWX-3)	64-29	6464.5 - 6465.0	CO	
(MWX-3)	66-17	6893.4 - 6893.8	PAL	August, 1983
(MWX-3)	67-16	7096.1 - 7096.7	PAL	
(MWX-3)	67-35	7134.2 - 7134.6	PAL	
(MWX-3)	68-15	7551.2 - 7551.7	SH	August, 1983
(MWX-1)	3-25	4330.7 - 4331.6	PAR	December, 1983 (high permeability)
(MWX-2)		5764.0	FP	February, 1984
(MWX-1)		5735.8 - 5736.0	FP	(calcite frac)

Key to Geologic Zone:

CO = Coastal
FM = Fluvial (meander belts)
FP = Fluvial (point bars)
PAL = Paludal
PAR = Paralic
SH = Shoreline / Marine

Table 1.5 Variables Used in Regression Analyses

Variable no.		Independent Variables
1	*	BET surface area (square meters per gram)
2		Depth (feet)
4		Porosity (percent)
8		Klinkenberg permeability (md) at 5000 psi confining pressure
13	*	Total crack length (cm) per square cm in SEM
14	*	Arithmetic mean of sphere diameters (from SEM)
15		Quartz (percent)
16		Na-feldspar (percent)
18		Chert (percent)
19		Lithic fragments (not including chert) (percent)
20		Total carbonate (percent)
21		Matrix (percent)
22		Visible porosity (percent)
26		Crack thickness (in microns) at 500 psi
27		Crack thickness (in microns) at 5000 psi

Dependent Variable

24	Slope from linear regression on log-log data, first unloading, as defined in text

* not measured for all cores; omitted from ridge regression

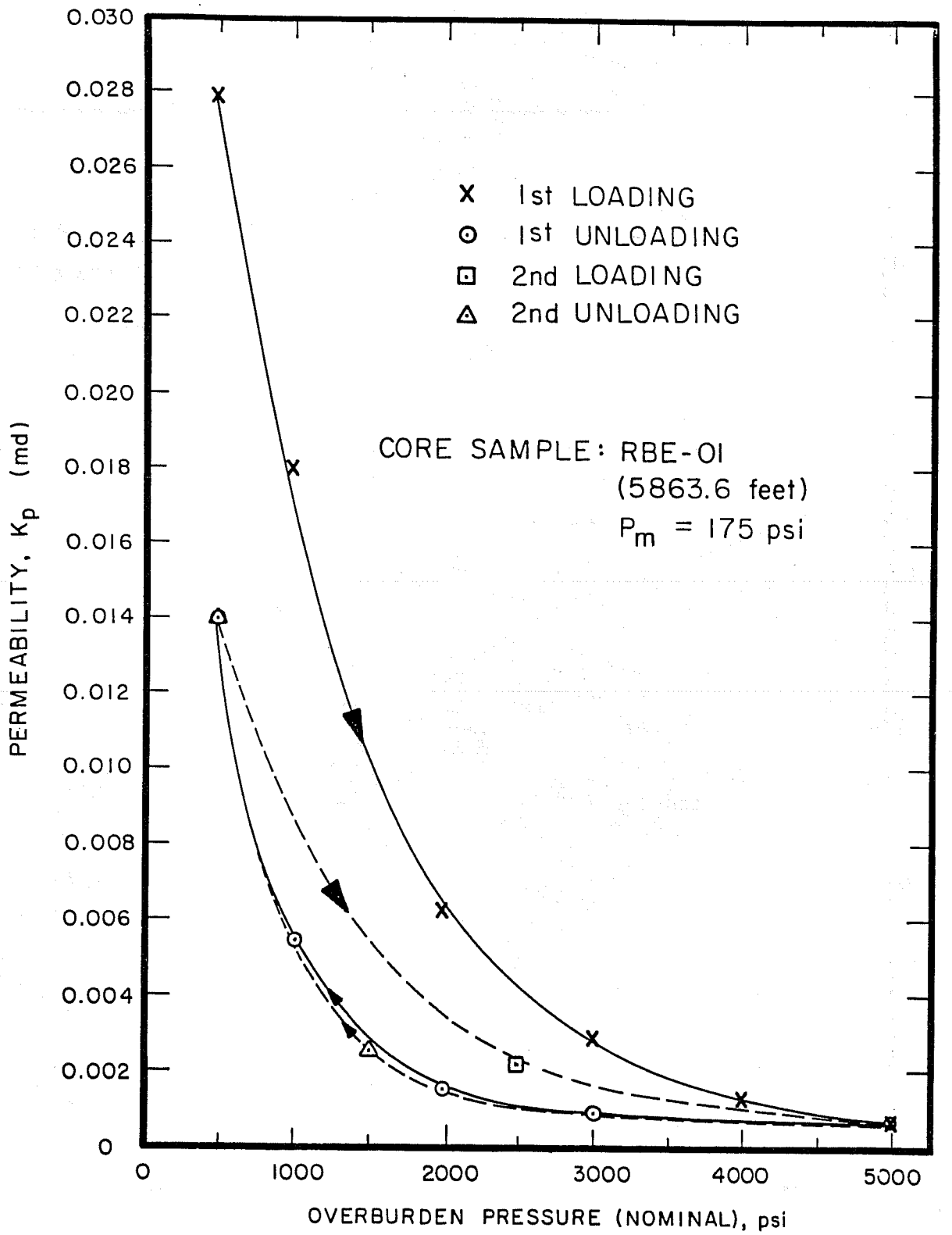

Fig. 1.1 Pressure sensitivity behavior of a low permeability core sample. This plot shows the large reduction in permeability when confining pressure is increased and the failure of the sample to regain all of its initially measured permeability when the confining pressure is reduced within the time typically allowed for such measurements.

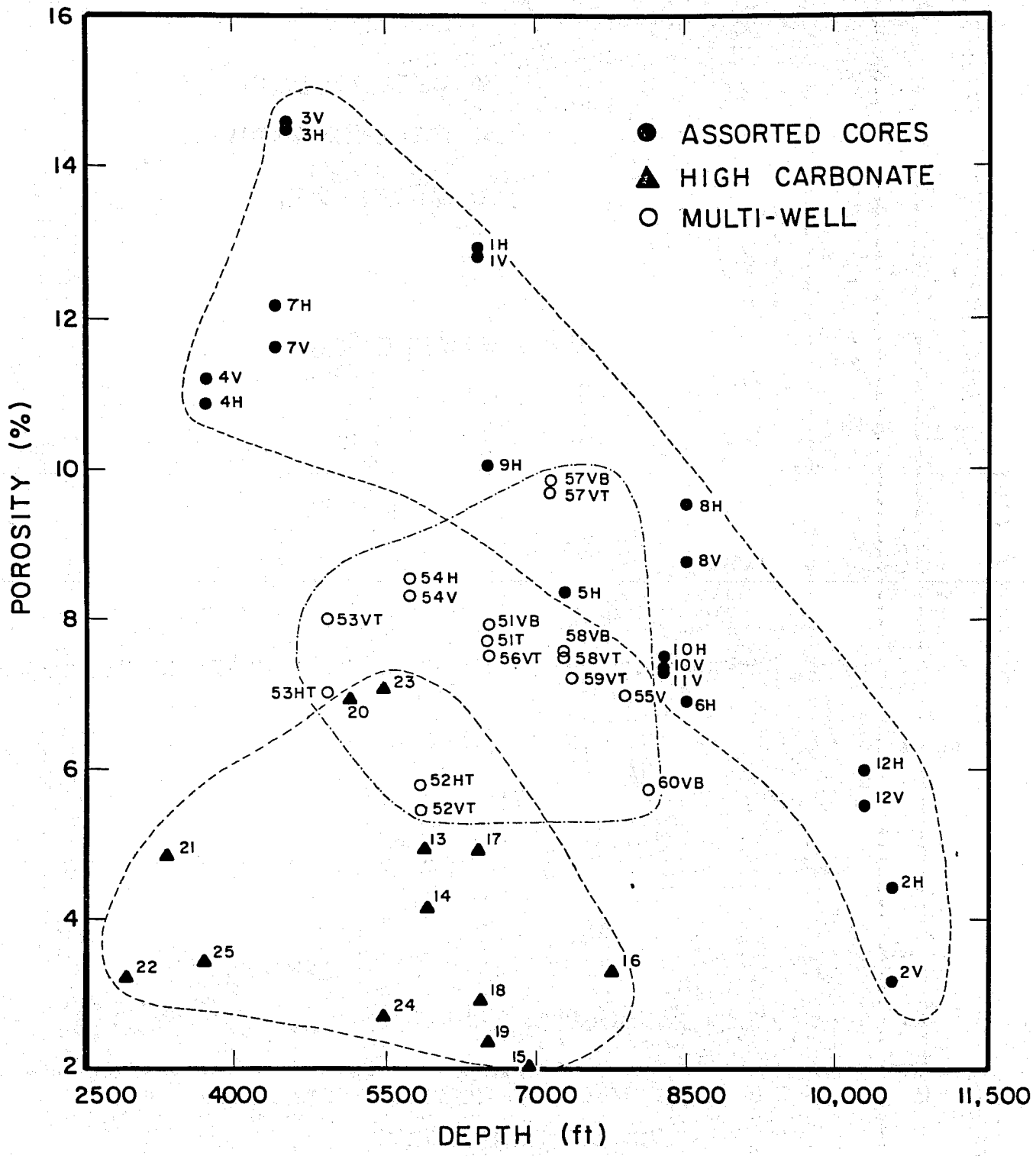

Fig. 1.2 Porosity vs. depth. Assorted cores show decrease in porosity with depth. High carbonate and Multi-Well samples do not show consistent trends.

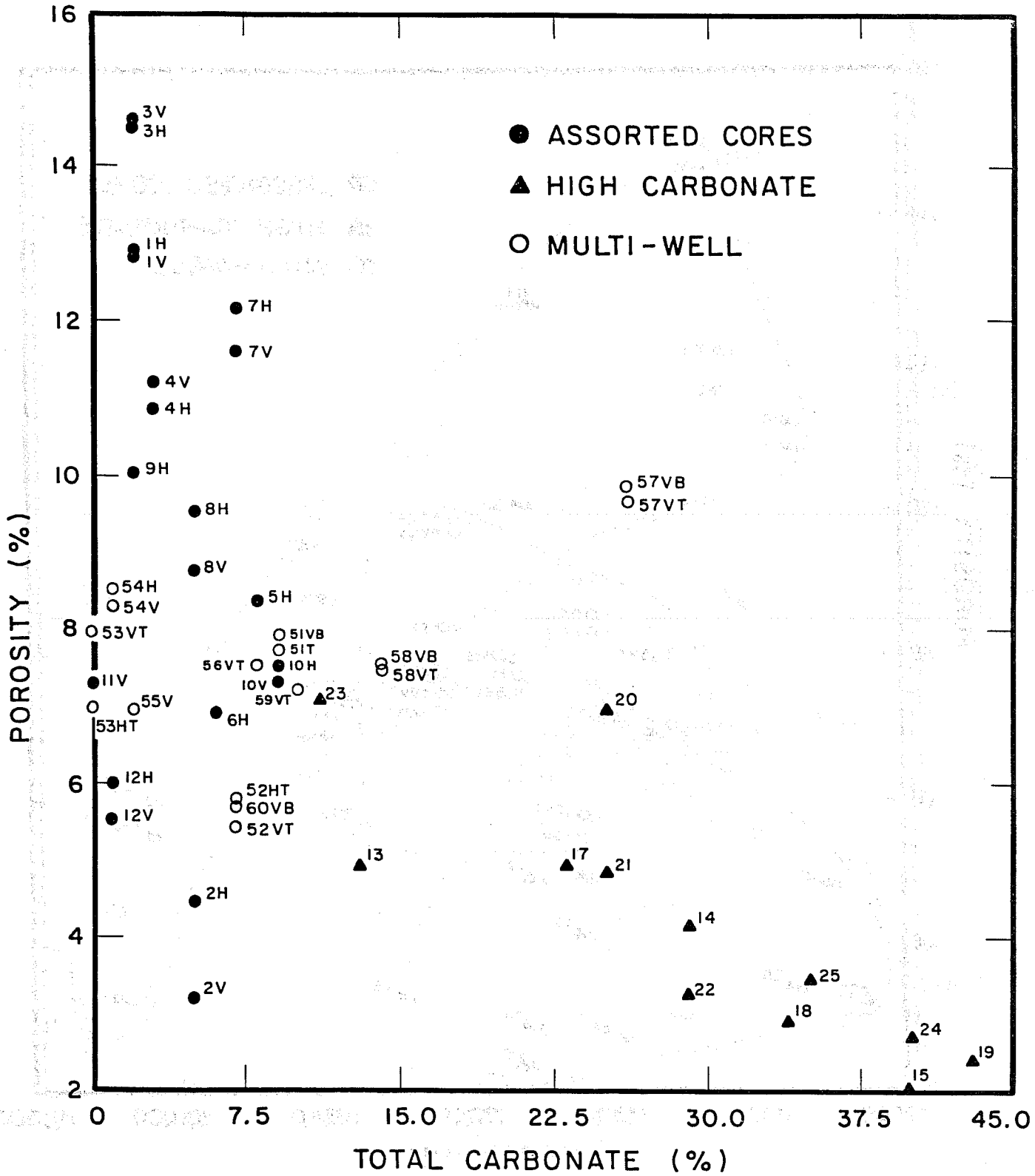

Fig. 1.3 Porosity vs. total carbonate. Overall tendency for porosity to decrease with increase in total carbonate.

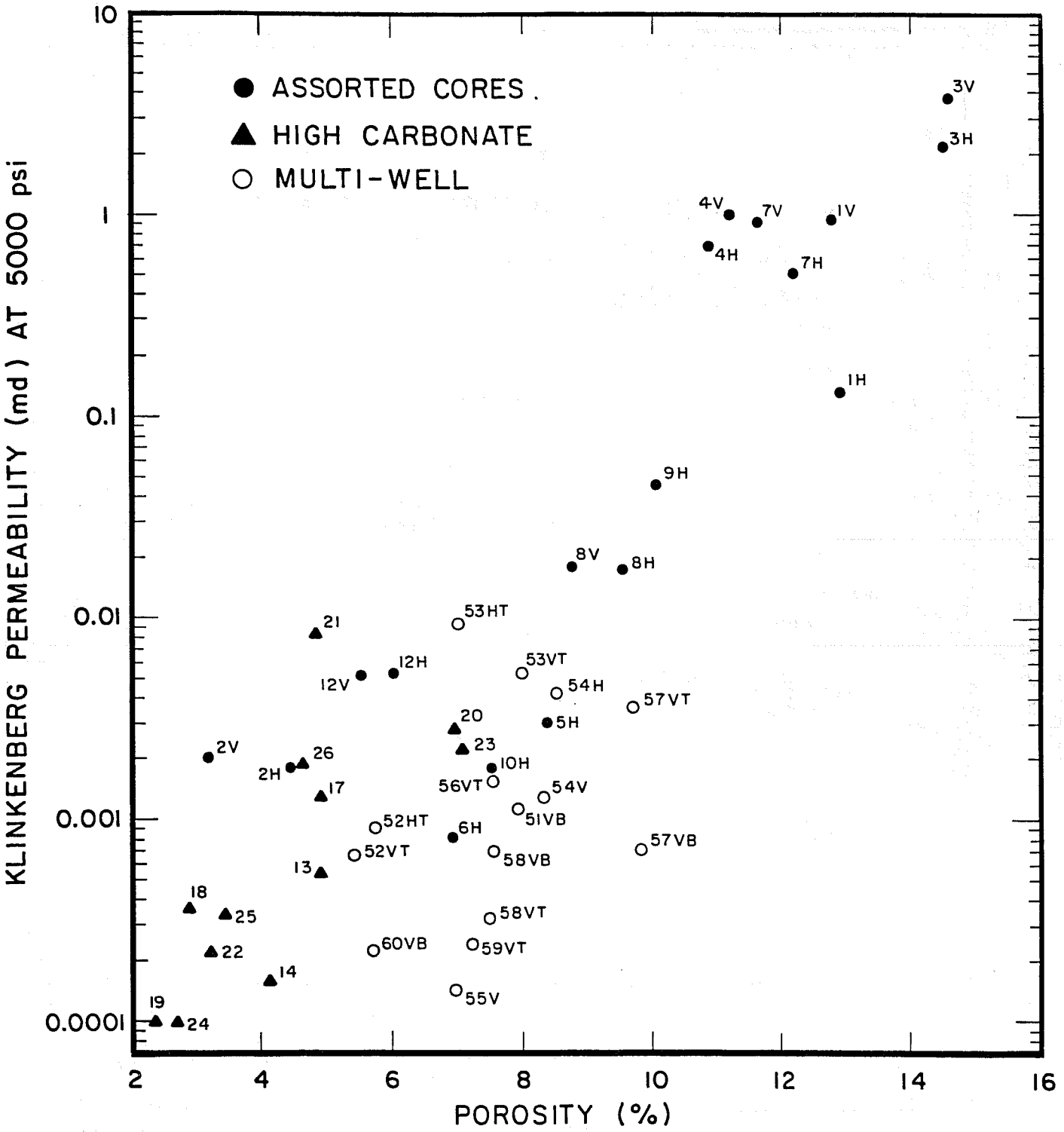

Fig. 1.4 $K_{\infty,5000}$ vs. porosity. A general trend of $K_{\infty,5000}$ to increase with porosity is shown. For porosities less than 8%, all permeabilities fall below 10 microdarcies, but results are scattered.

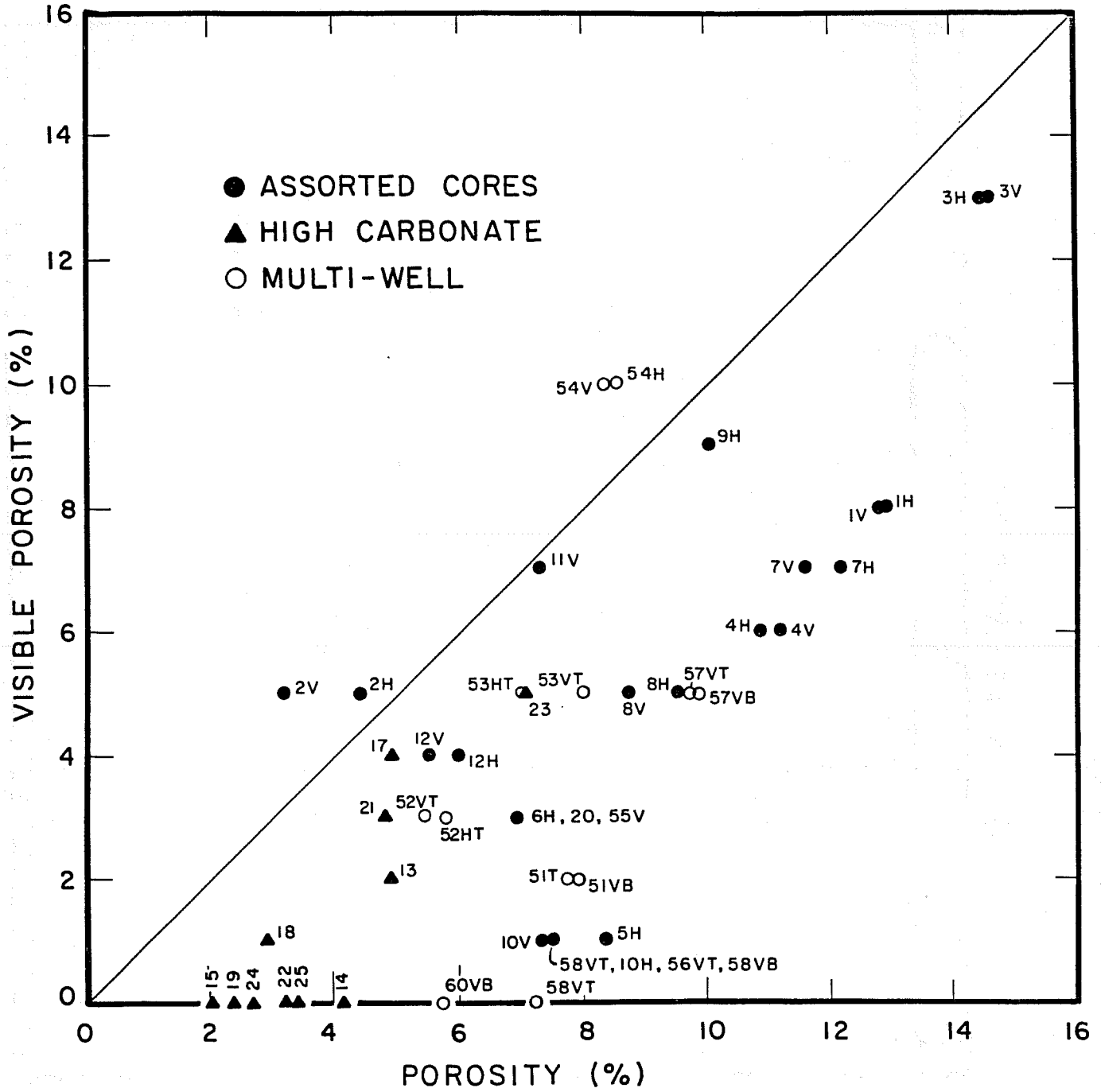

Fig. 1.5 Comparison of visible porosity observed in thin sections and porosity measured by routine core analysis. There is a tendency for visual porosities from thin sections to be too low by about 3% of total (solid + pore space) volume.

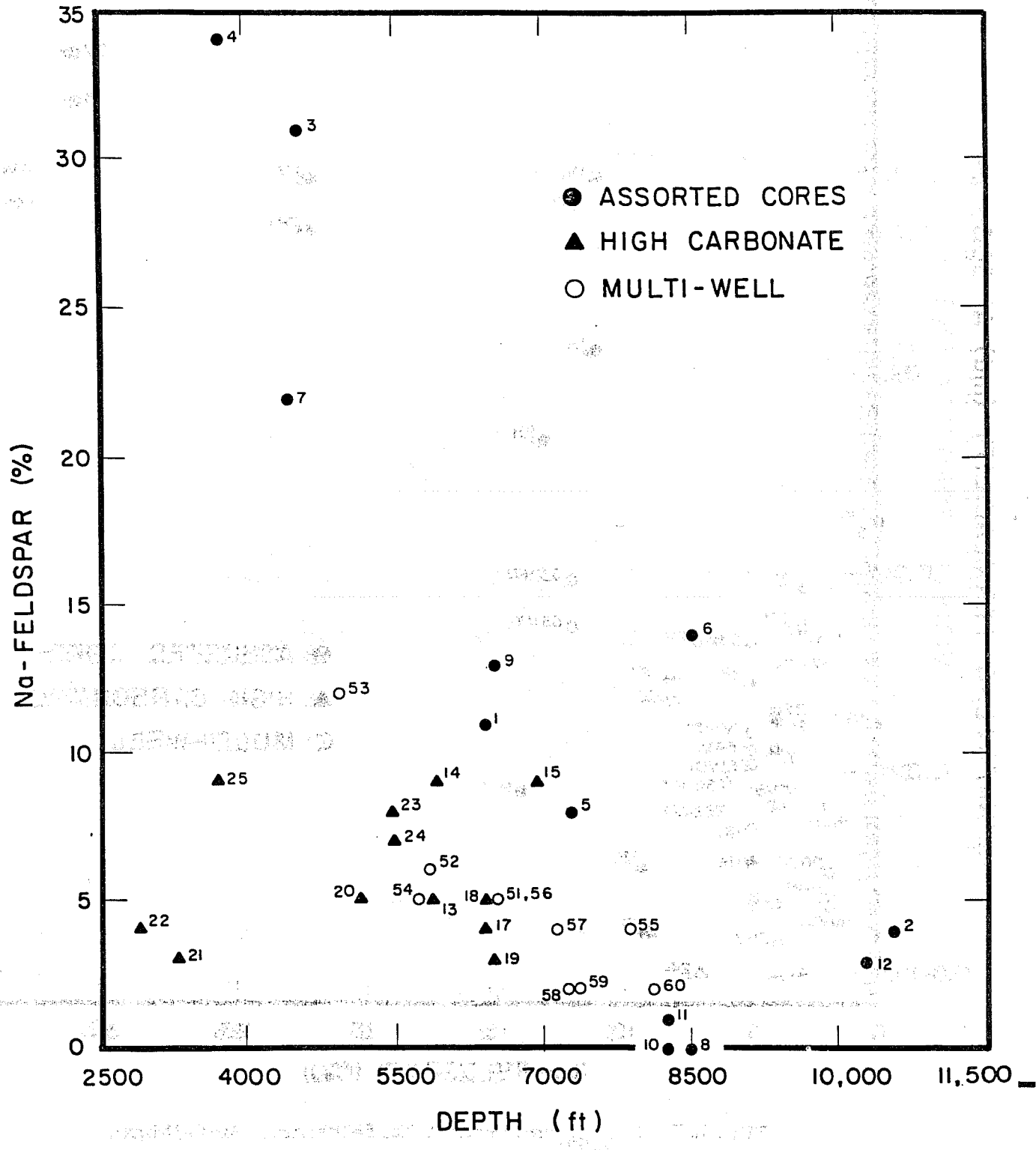

Fig. 1.6 Percent of Na-feldspar vs. depth. Percent of Na-feldspar tends to decrease with increasing depth for assorted cores and Multi-Well samples and is generally too low for the high carbonate samples.

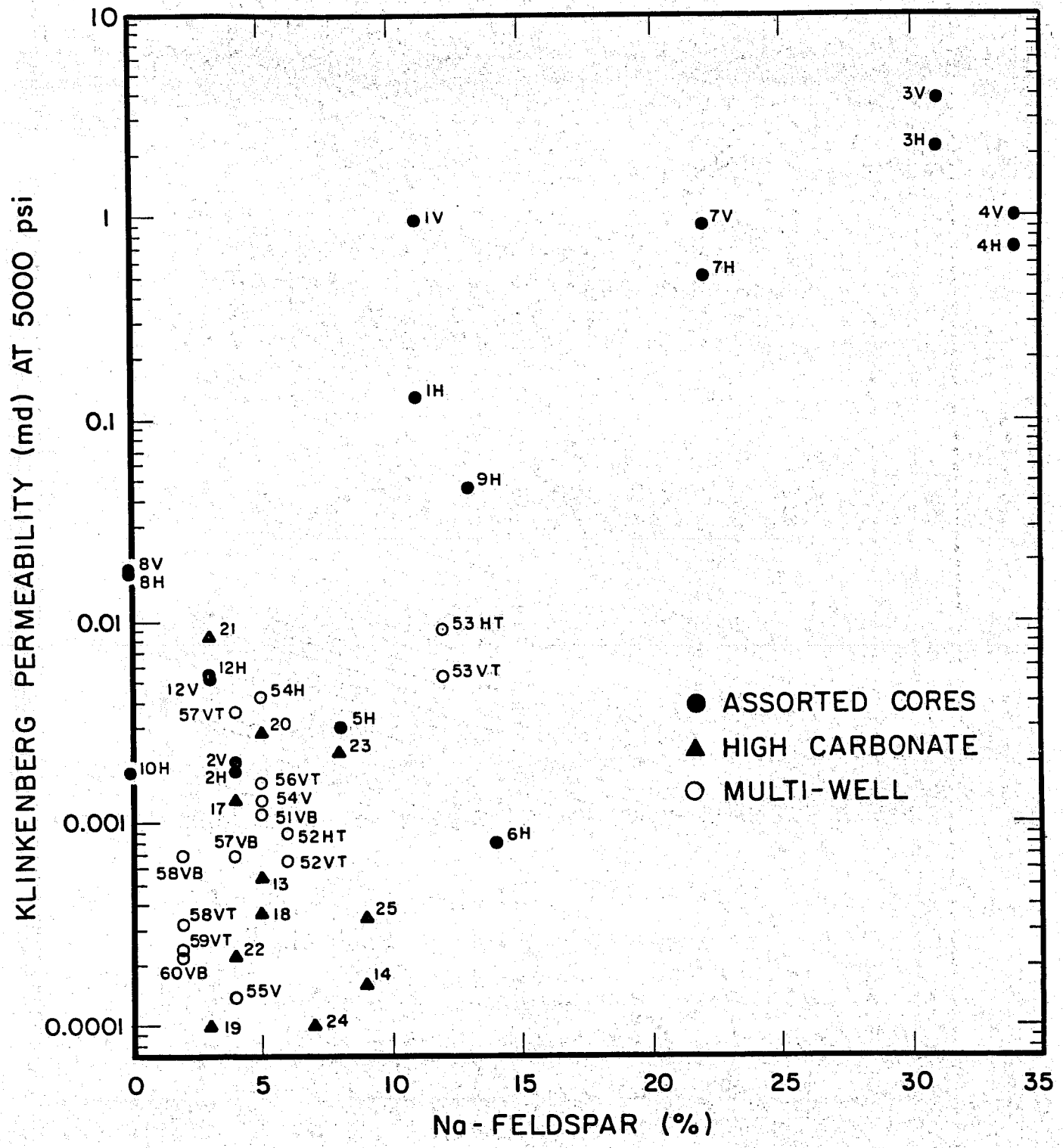

Fig. 1.7 $K_{\infty,5000}$ vs. percent Na-feldspar. Na-feldspar is generally low in the low permeability samples.

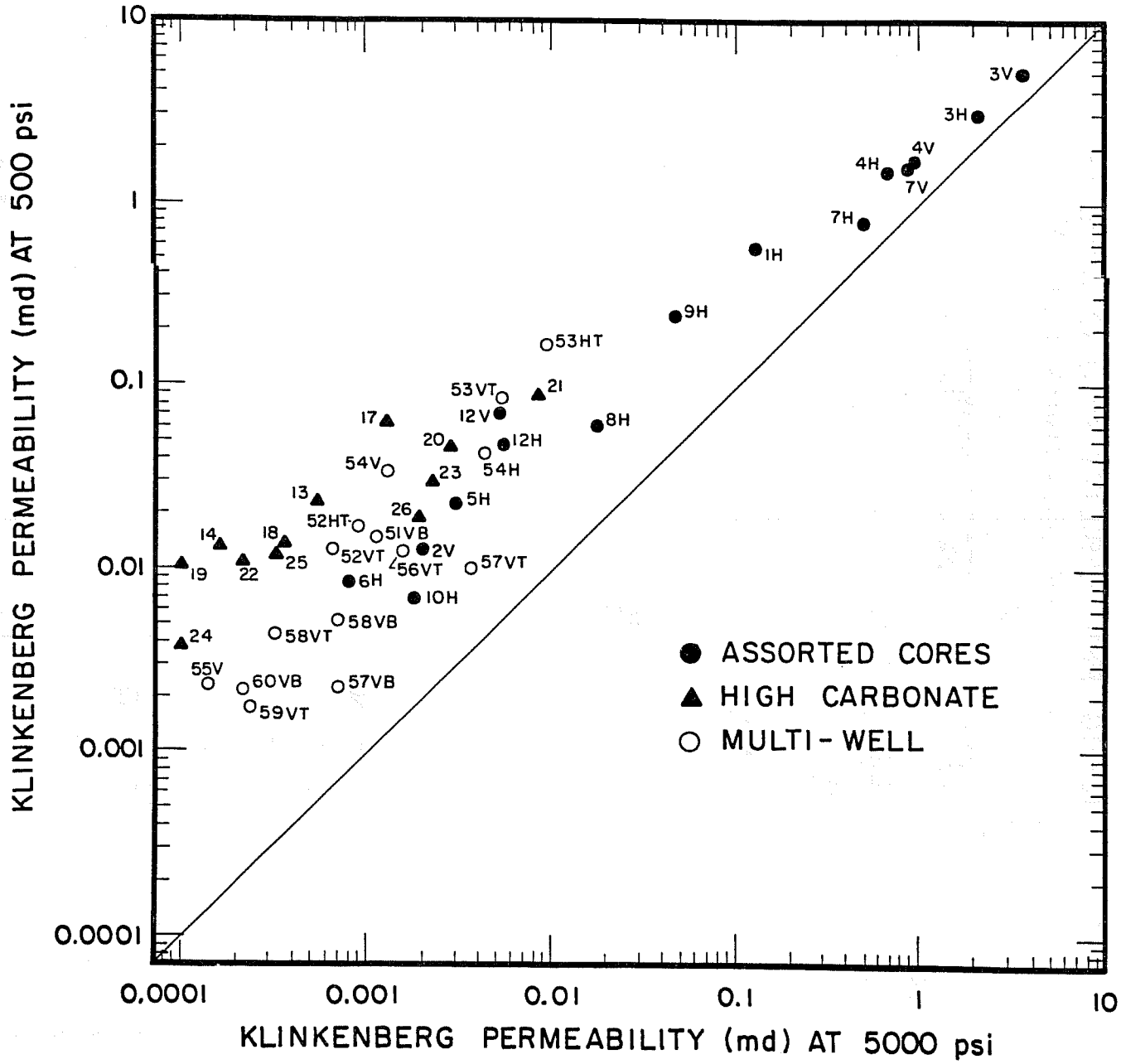

Fig. 1.8 Sensitivities of core samples to confininf pressure shown by plot of $K_{\infty,500}$ vs. $K_{\infty,5000}$. The vertical distance between a point and the diagonal line is proportional to log ($K_{\infty,500}/K_{\infty,5000}$) and therefore indicates the pressure sensitivity. The general trend of increase in pressure sensitivity with decrease in permeability can be seen.

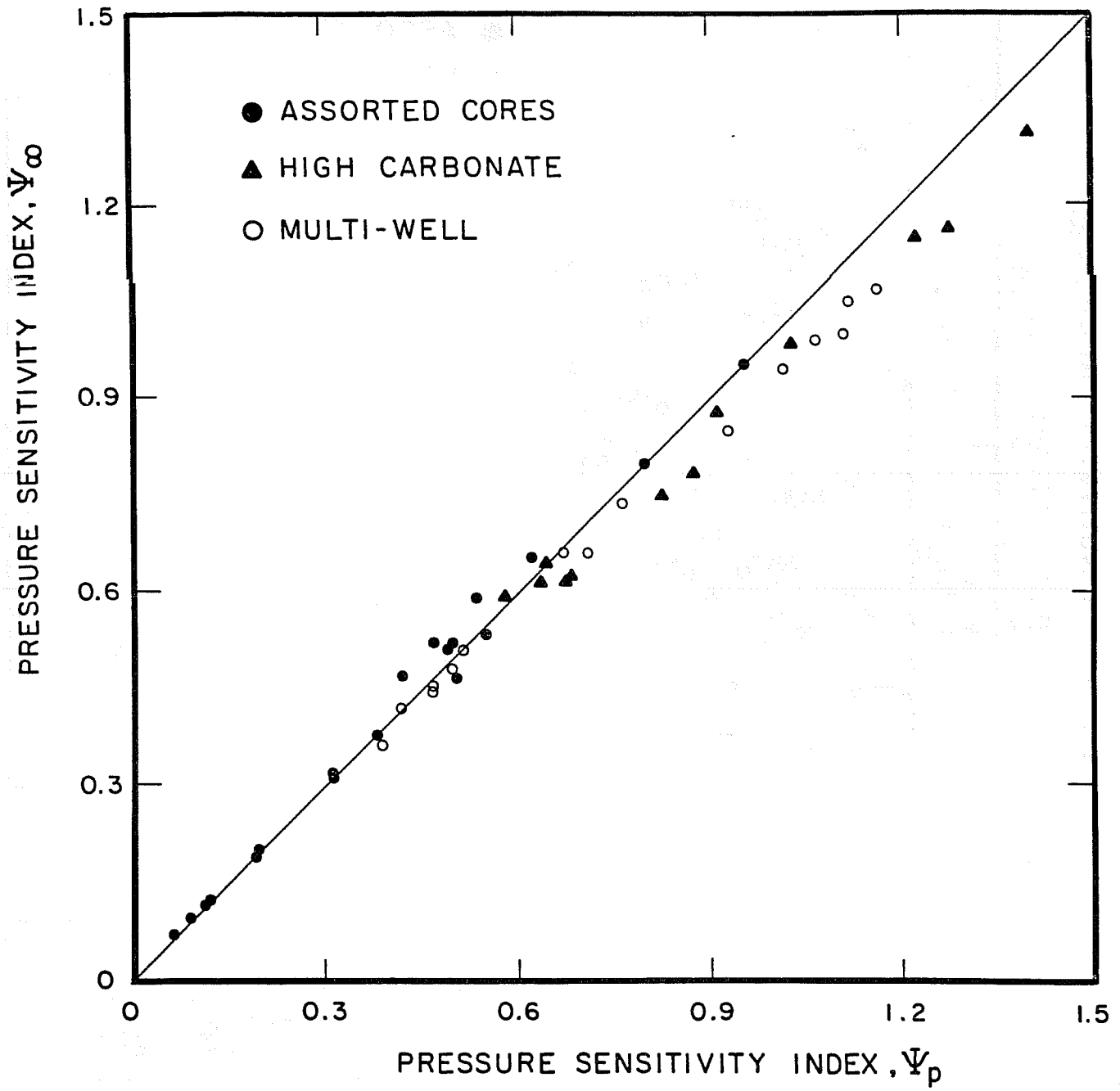

Fig. 1.9 Plot of Ψ_∞ vs. Ψ_p showing that the standardizing procedure used to provide comparison of pressure sensitivities between samples has only minor effect.

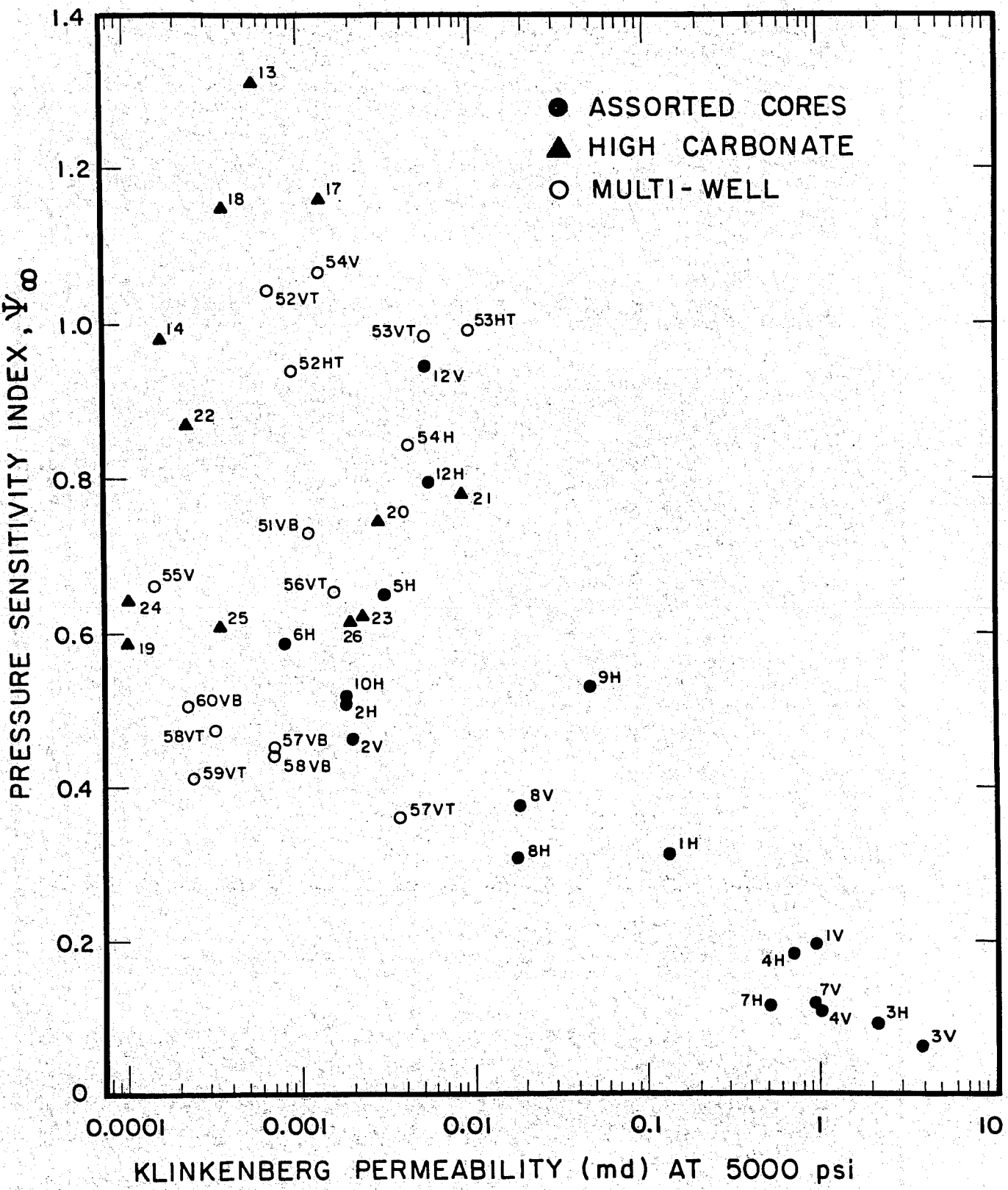

Fig. 1.10 Pressure sensitivity index vs. $K_{\infty,5000}$. As $K_{\infty,5000}$ decreases, the pressure sensitivity index tends to increase and to show more variation among samples.

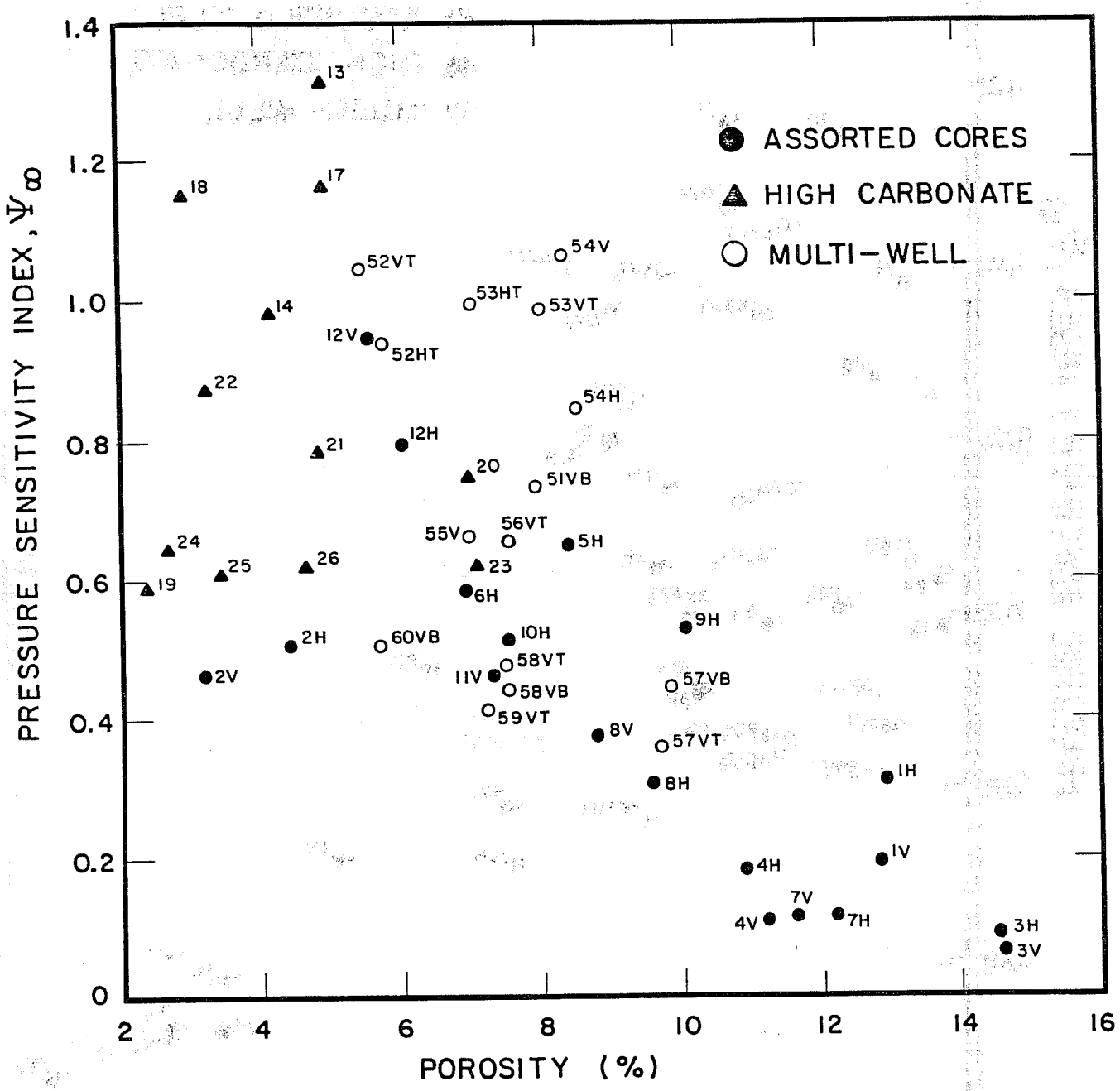

Fig. 1.11 Pressure sensitivity index vs. porosity. In general, the pressure sensitivity index tends to increase as porosity decreases, but scatter increases as porosity decreases. However, porosity appears to be the most outstanding single variable for correlation with the pressure sensitivity index.

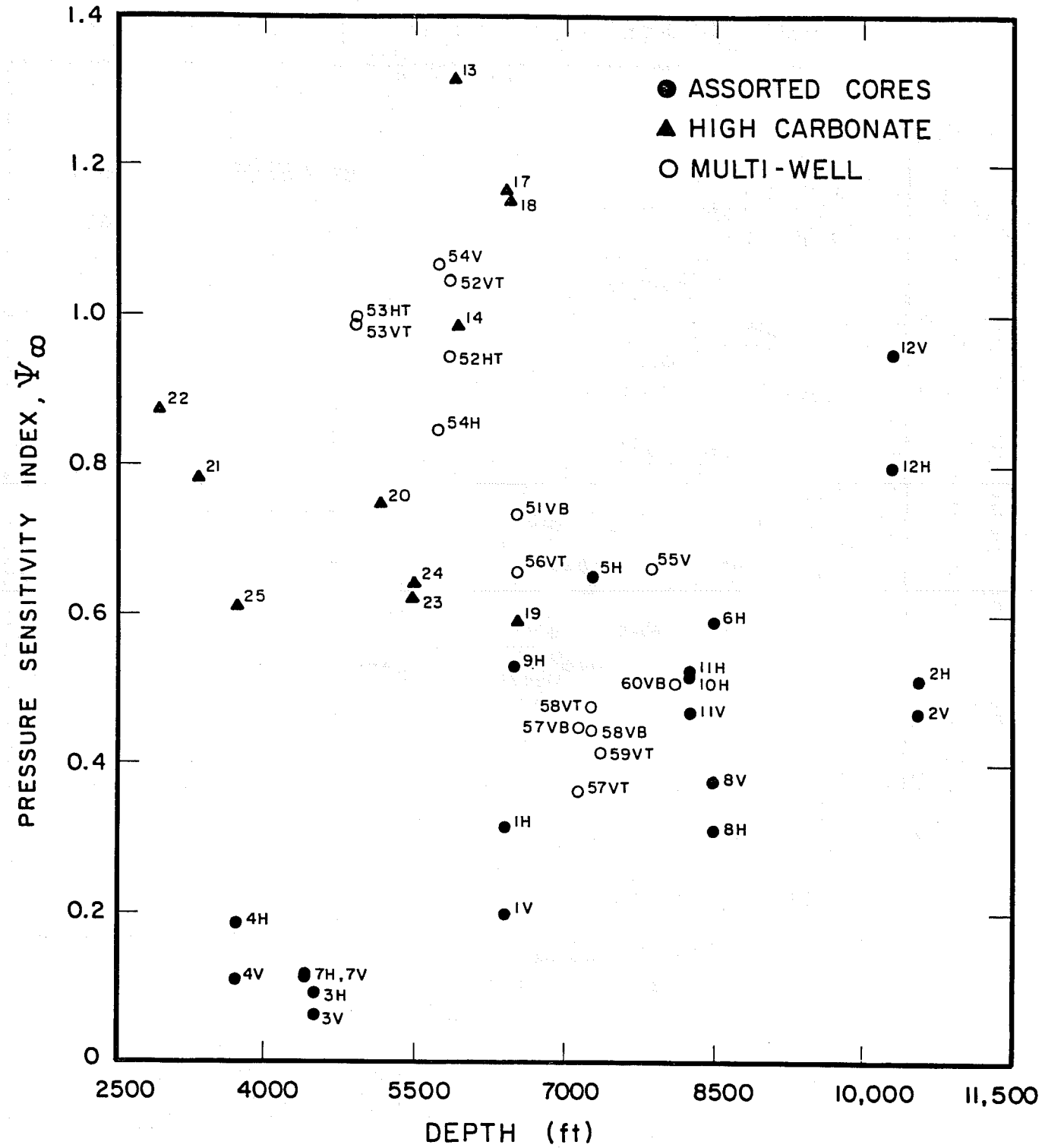

Fig. 1.12 Pressure sensitivity index vs. depth. Different suites of core samples exhibit different behavior. Assorted cores tend to display higher pressure sensitivity with increasing depth. However, Multi-Well samples tend to show lower pressure sensitivity with increasing depth. Permeabilities of high carbonate core samples are much more pressure sensitive than those of assorted cores from comparable depths.

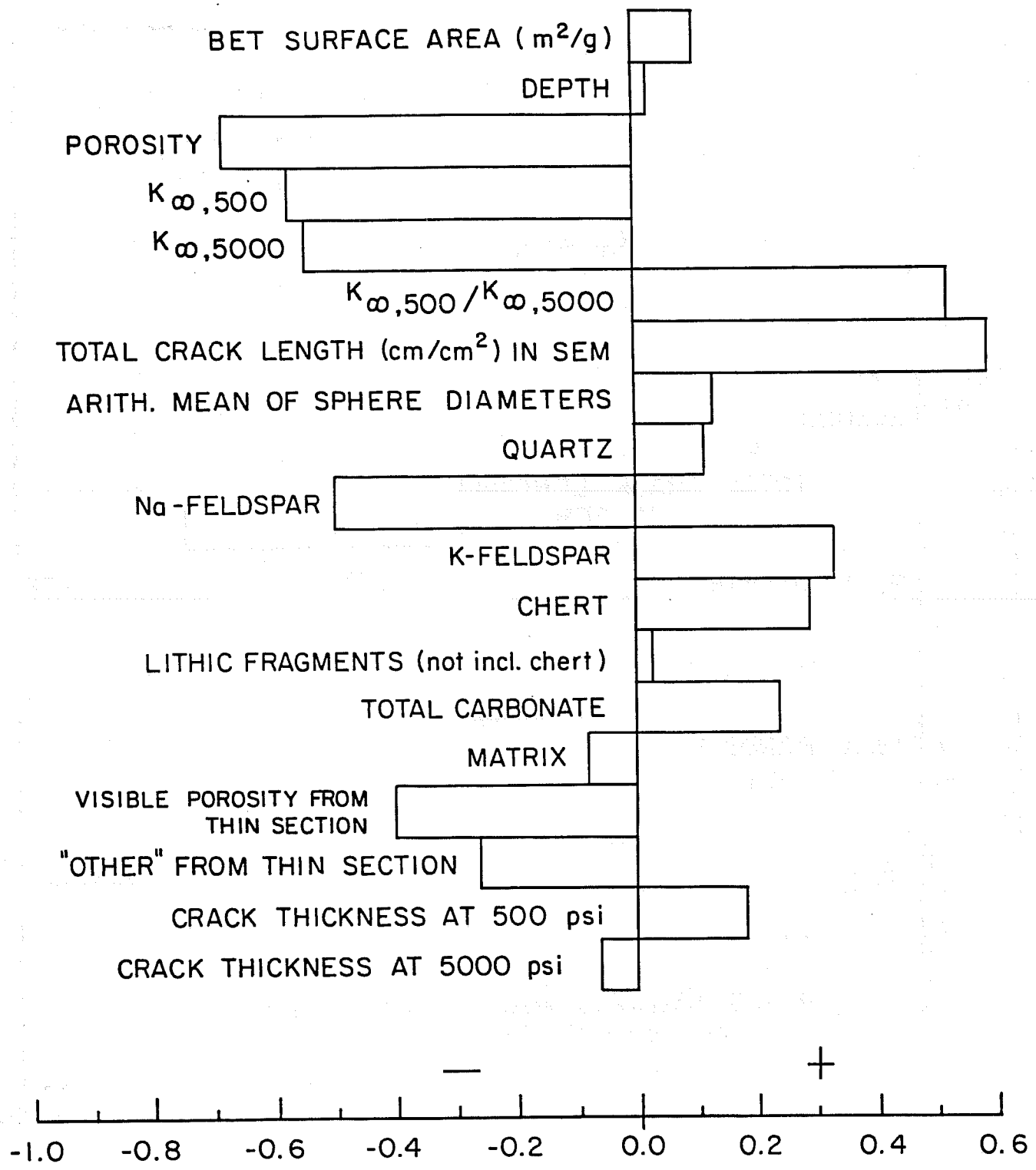

Fig. 1.13 Simple correlation coefficients of indicated variables with the pressure sensitivity index Ψ_∞. Absolute values of the correlation coefficients are illustrated by the lengths of bars. Each bar extending to the left of the vertical line indicates that the pressure sensitivity index tends to decrease as the variable increases. A bar extending to the right of the vertical line indicates that the pressure sensitivity index tends to increase as the variable increases.

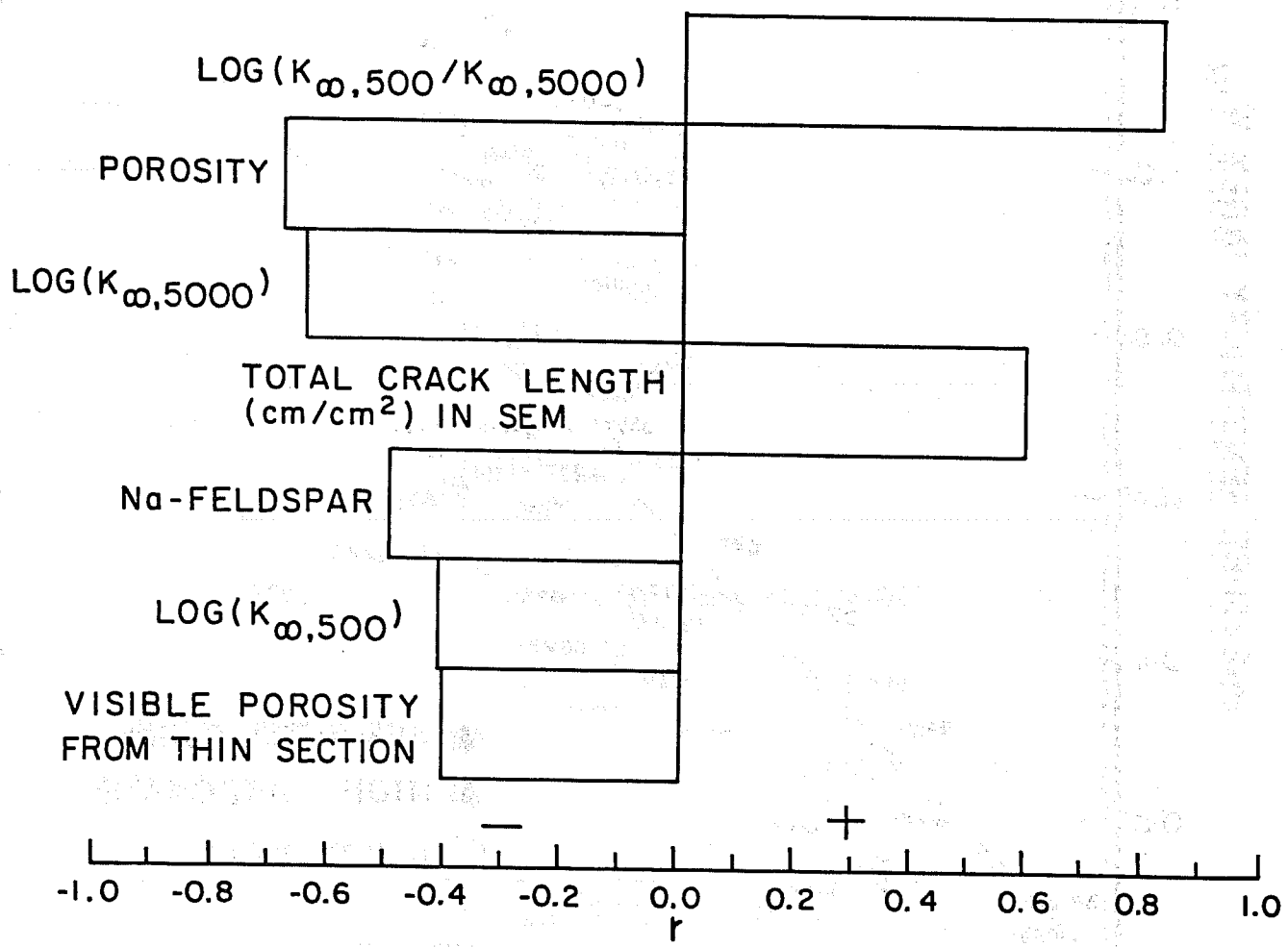

Fig. 1.14 Simple correlation coefficients of selected variables with the pressure sensitivity index Ψ_∞. Lengths of bars illustrate the absolute values of the correlation coefficients, and directions of bars indicate positive or negative correlation as in Fig. 1.13.

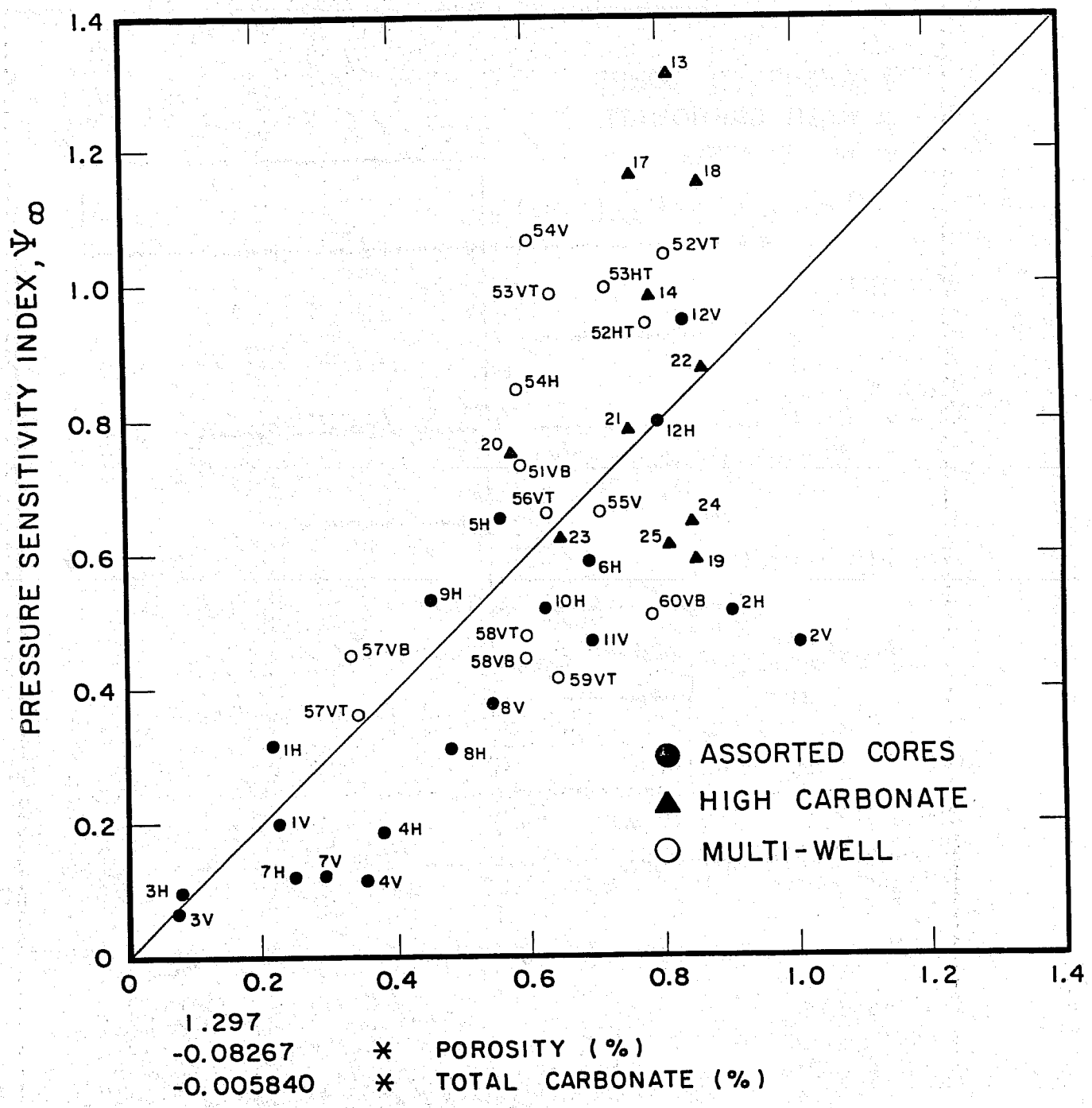

Fig. 1.15 Measured pressure sensitivity index values vs. those predicted by one of the best of the correlations using two independent variables. If predictions were perfect, all points would lie on the diagonal line.

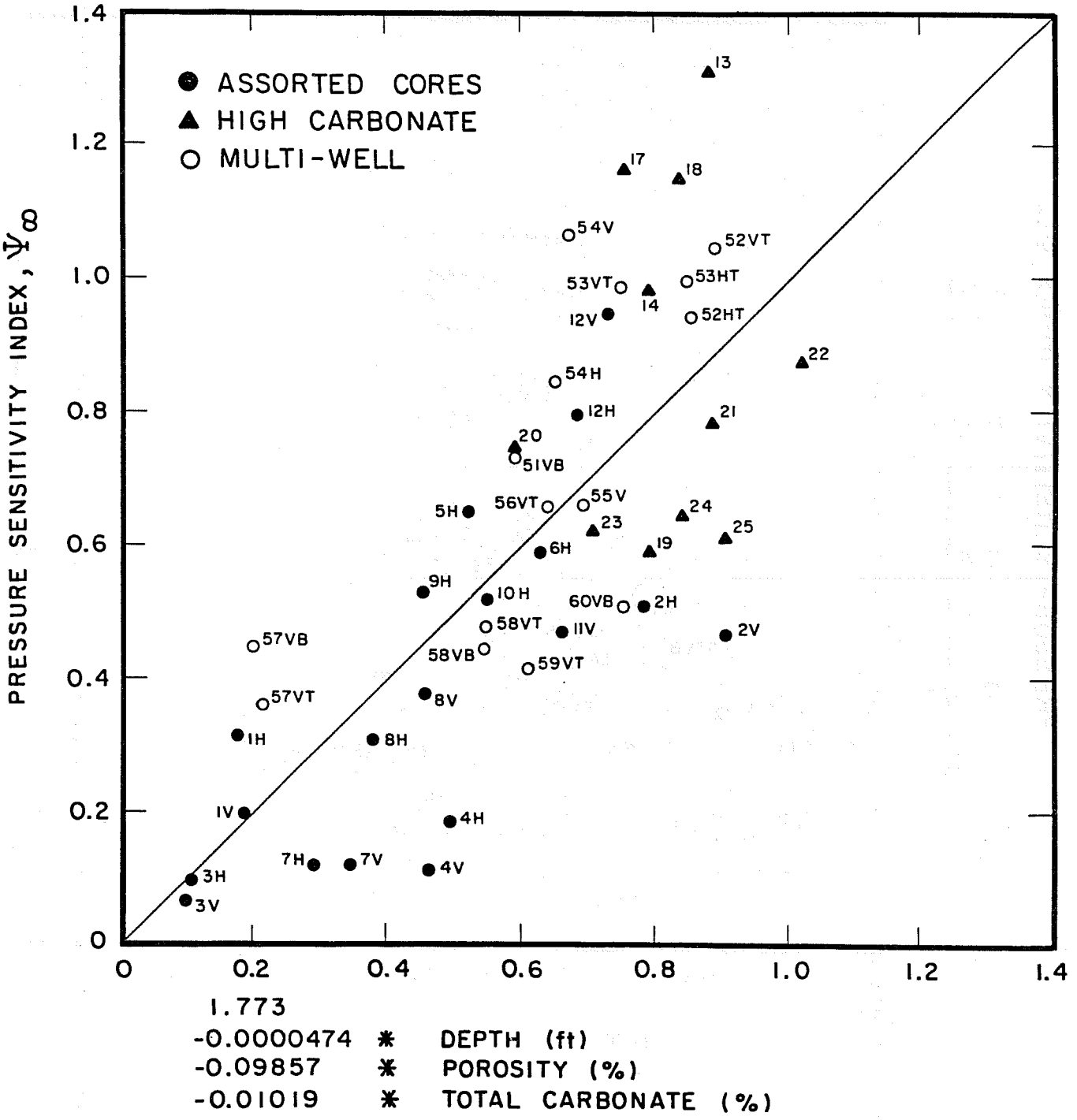

Fig. 1.16 Measured pressure sensitivity index values vs. those predicted by one of the best of the correlations using three independent variables.

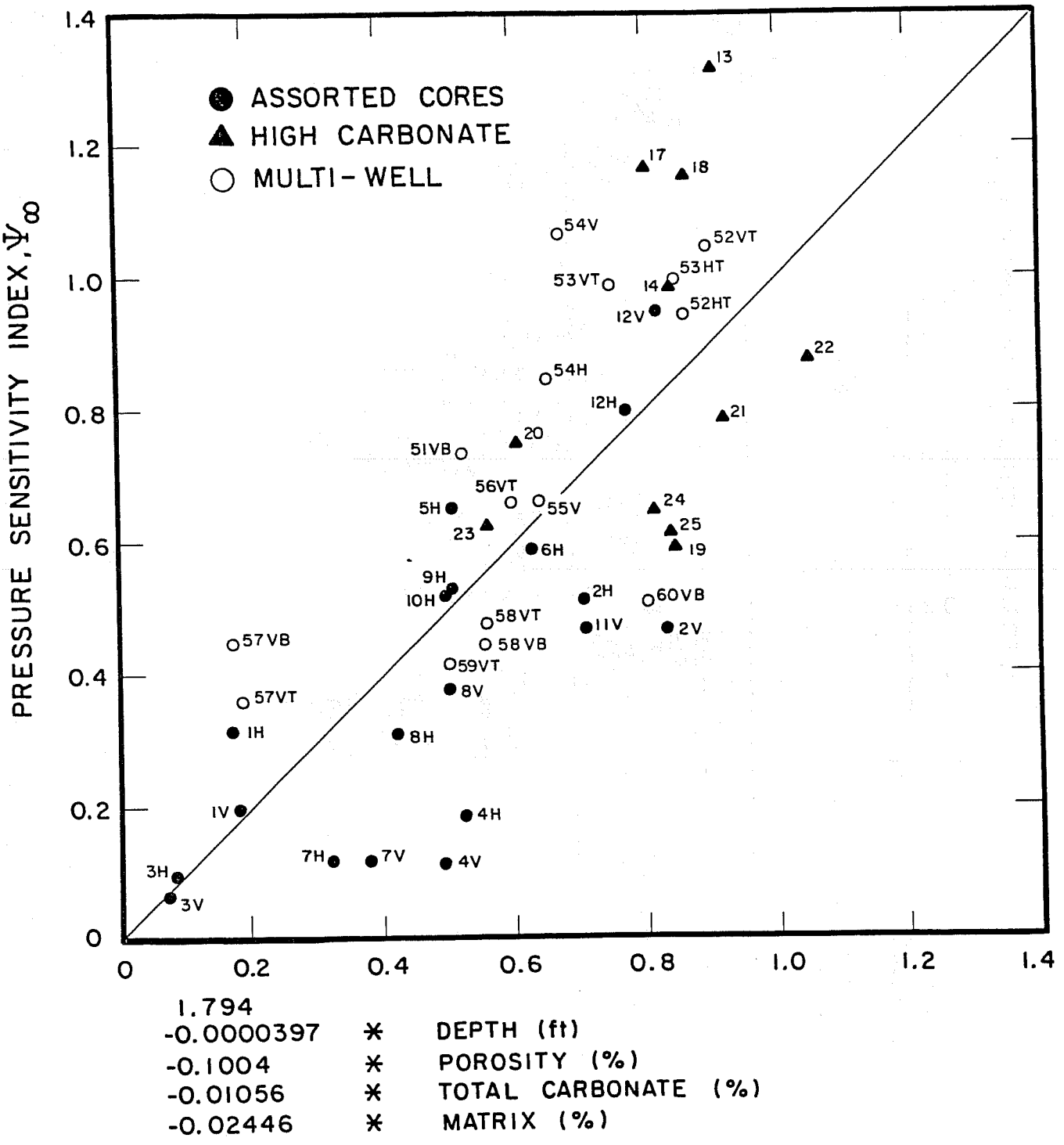

Fig. 1.17 Measured pressure sensitivity index values vs. those predicted by one of the best of the correlations using four independent variables.

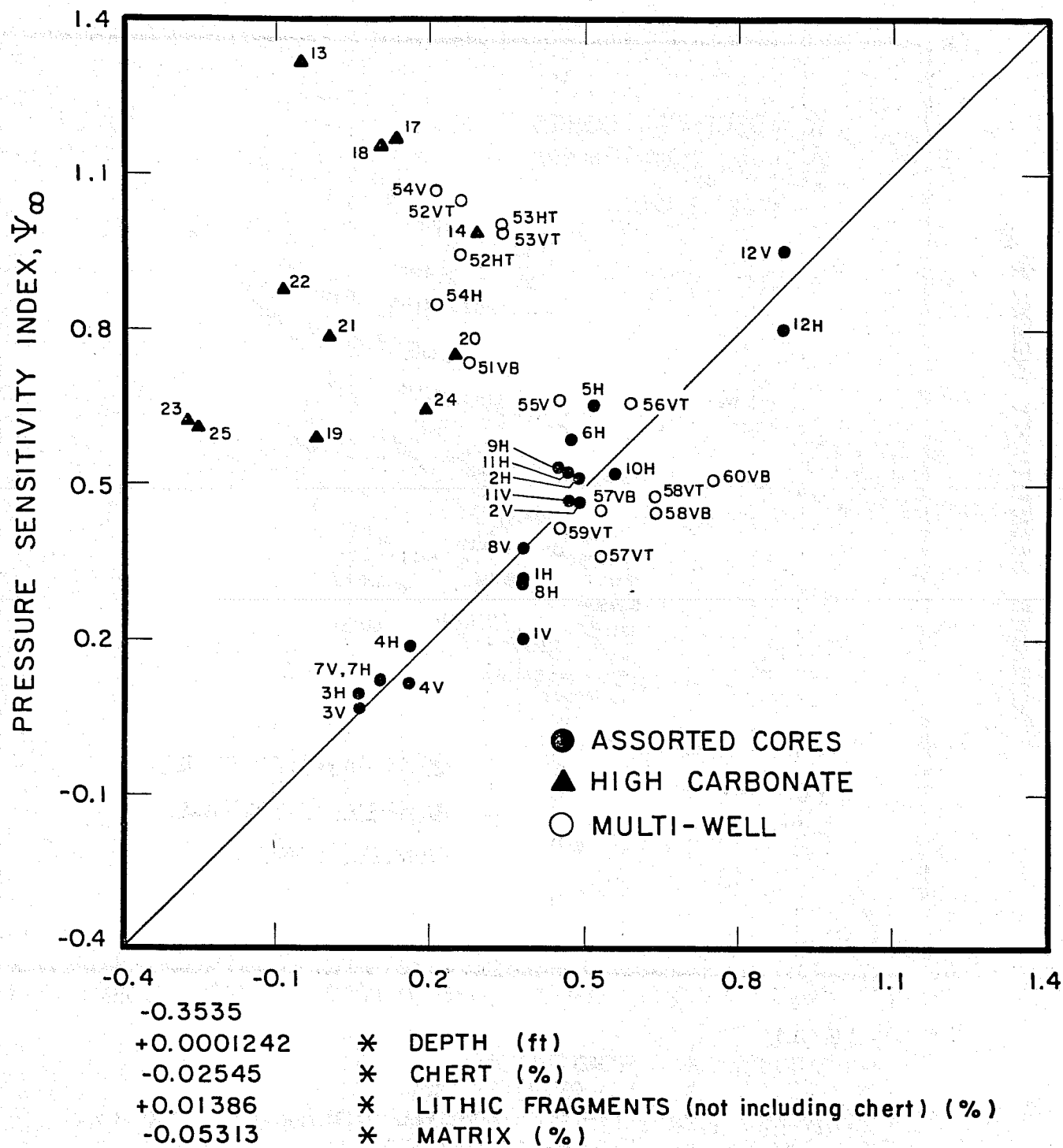

Fig. 1.18 Pressure sensitivity index vs. a linear combination calculated by linear regression on assorted core suite data. Once again, the trend displayed by Multi-Well samples is in the opposite direction from that of assorted cores. High carbonate core samples again display more pressure sensitivity than comparable assorted cores.

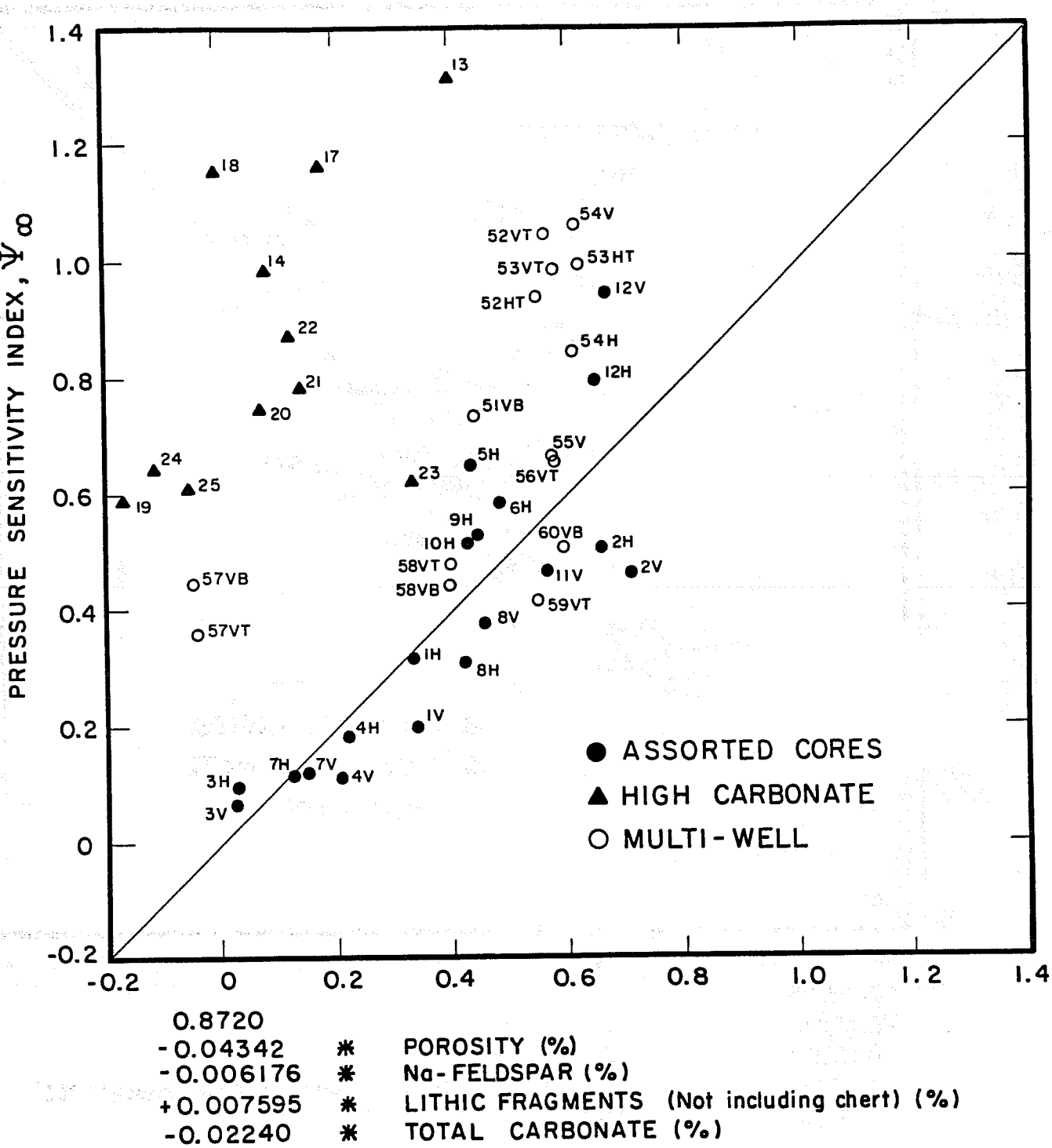

0.8720
-0.04342 * POROSITY (%)
-0.006176 * Na-FELDSPAR (%)
+0.007595 * LITHIC FRAGMENTS (Not including chert) (%)
-0.02240 * TOTAL CARBONATE (%)

Fig. 1.19 Pressure sensitivity index vs. a linear combination of variables. Noteworthy is the almost complete separation of points representing core samples of the high carbonate suite from those representing samples of the other two suites.

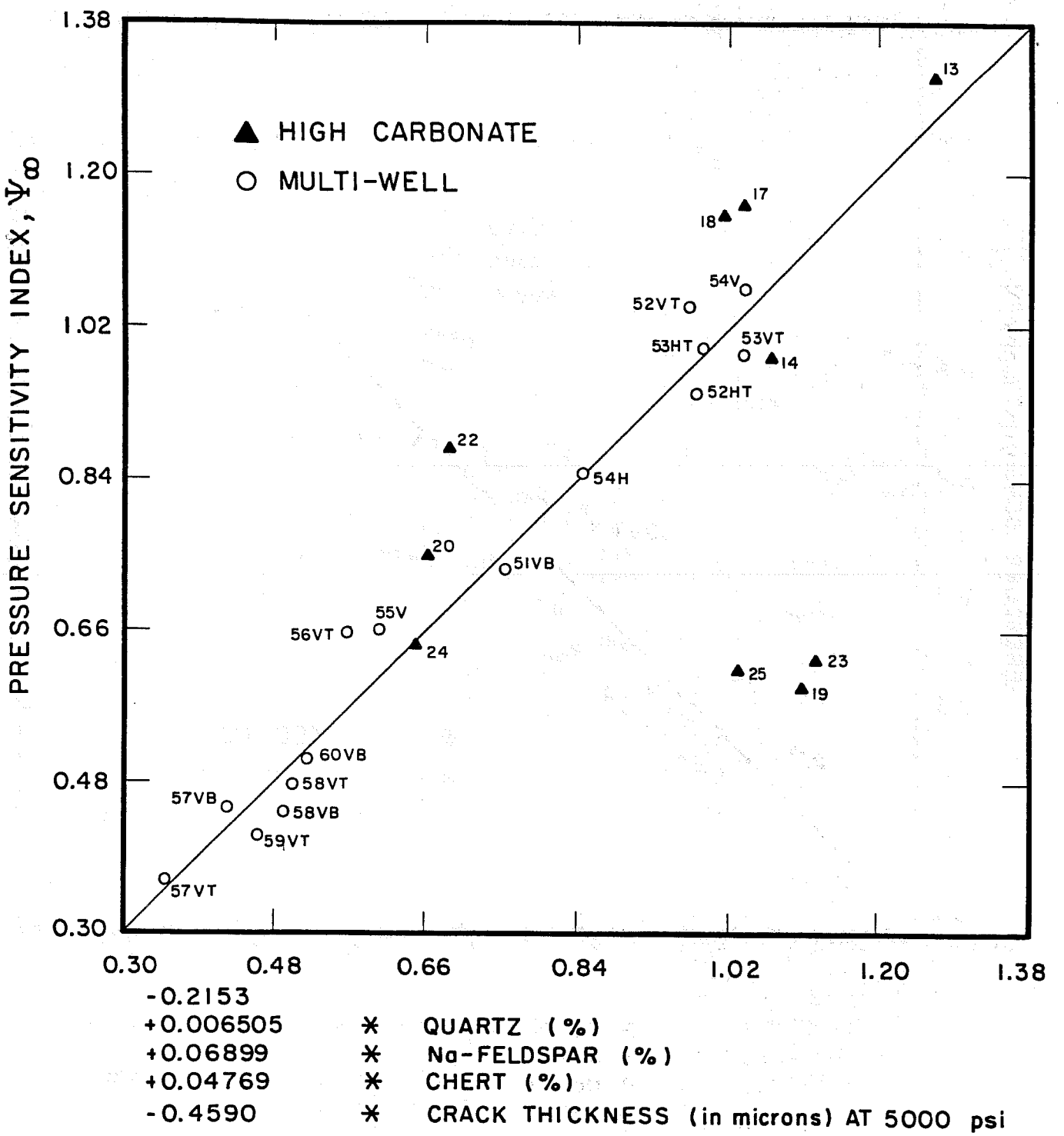

Fig. 1.20 Pressure sensitivity index vs. a linear combination of variables with regression coefficients determined from Multi-Well core data. The behavior of several of the high carbonate samples can also be approximated by this combination.

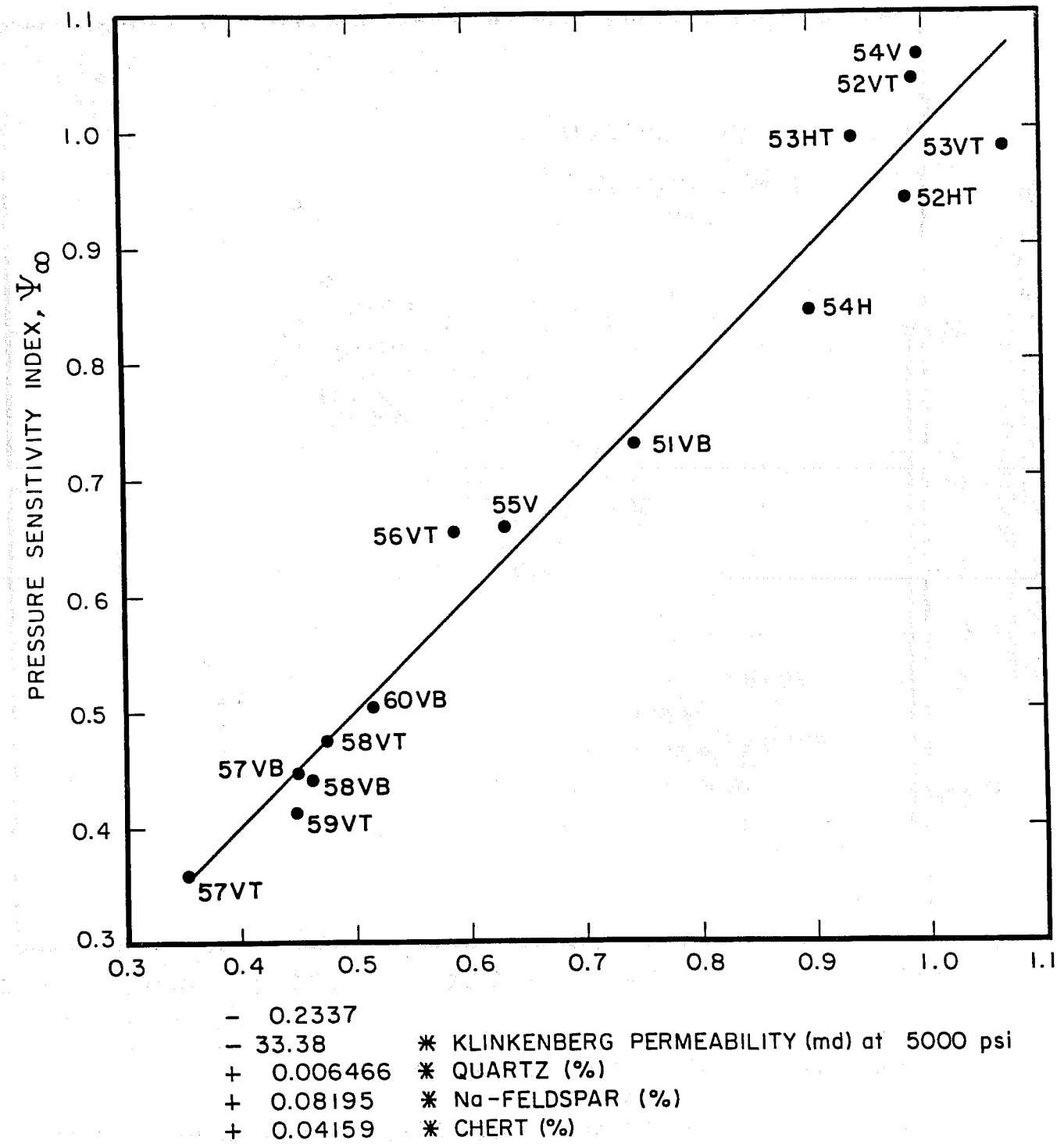

Fig. 1.21 Pressure sensitivity index vs. another linear combination of variables with regression coefficients determined from Multi-Well core sample data.

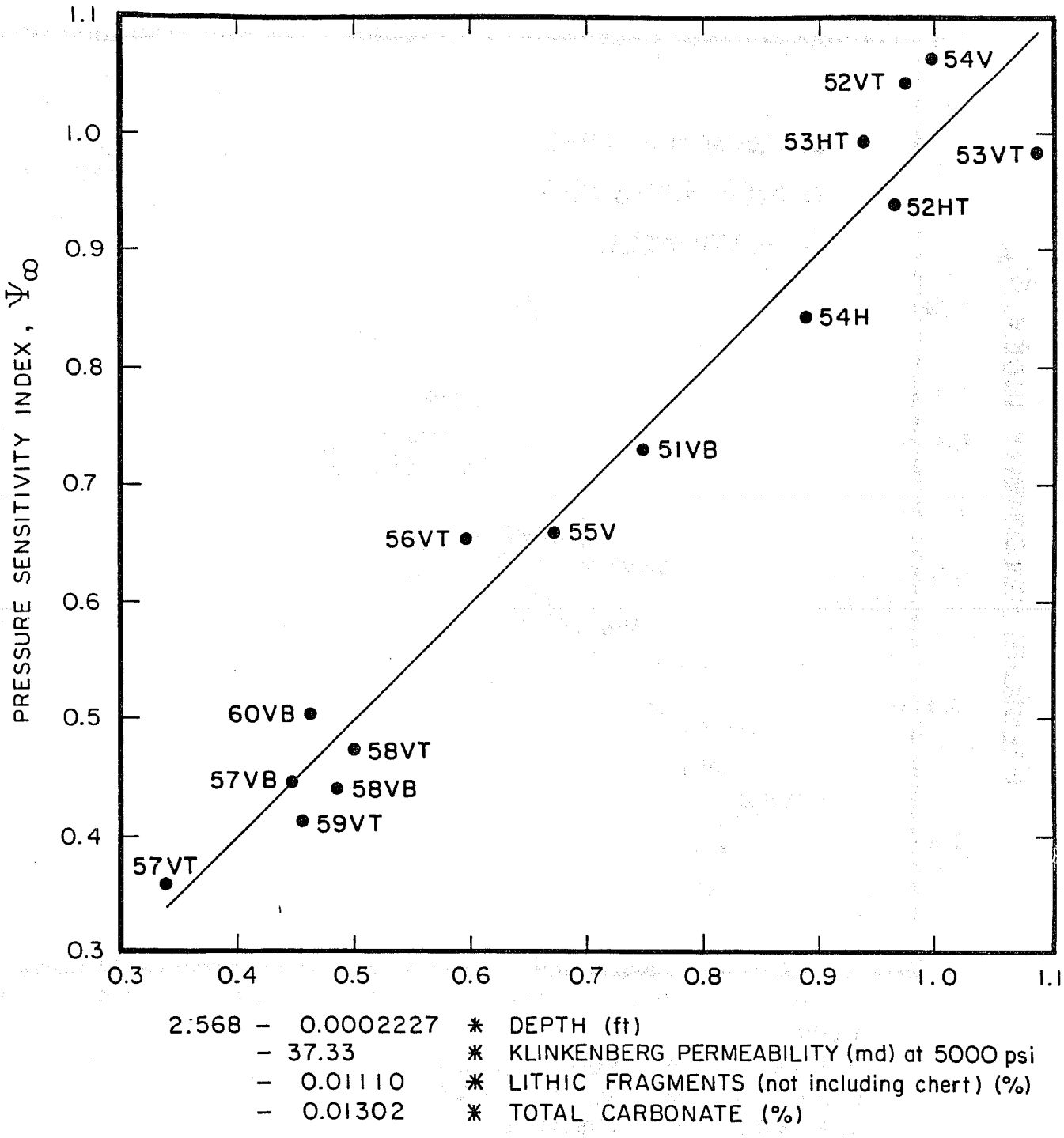

Fig. 1.22 Pressure sensitivity index vs. still another linear combination of variables with regression coefficients determined from Multi-Well core sample data.

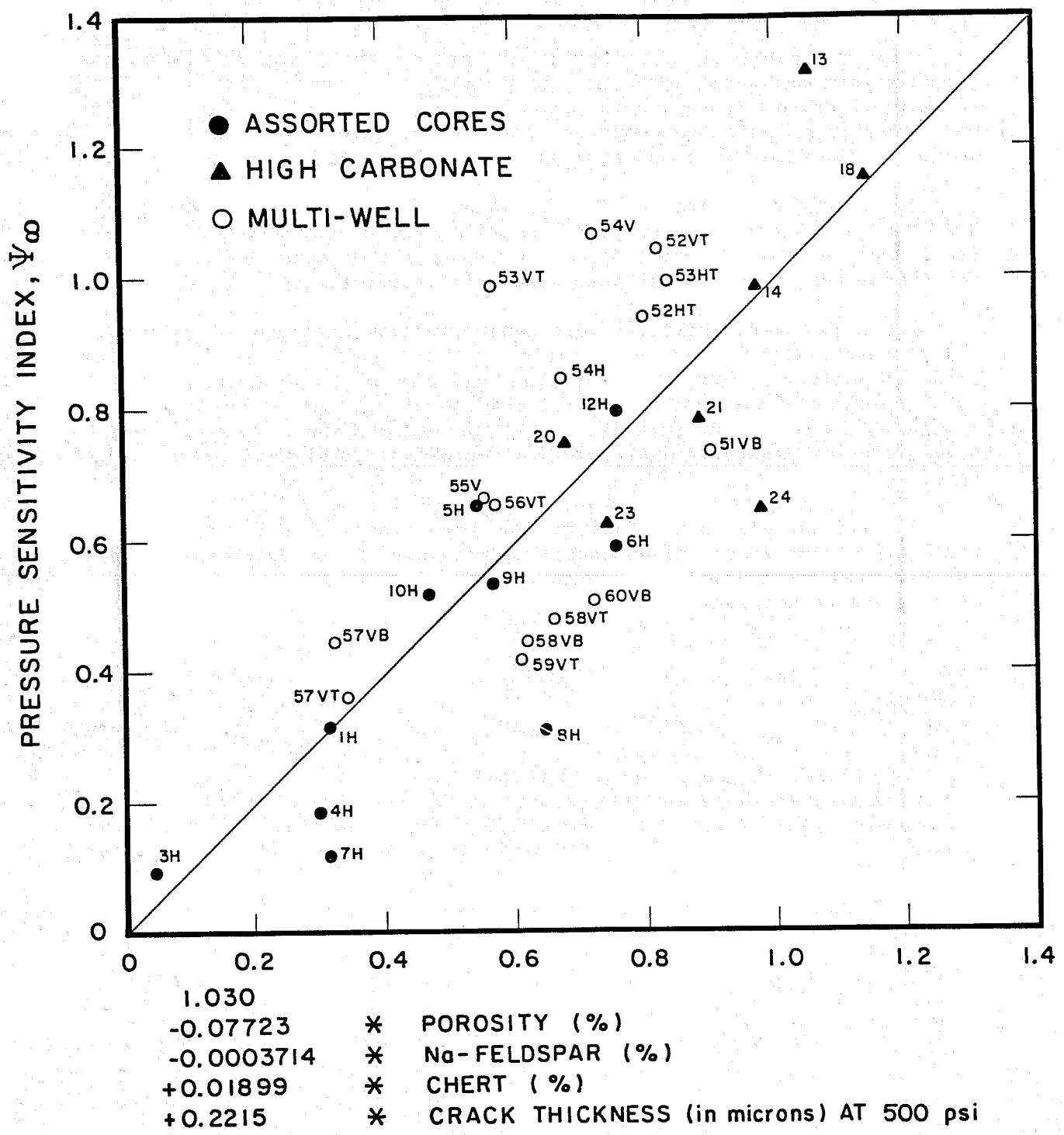

Fig. 1.23 Pressure sensitivity index vs. a linear combination of variables chosen using ridge regression. The indicated regression coefficients were obtained without adding any bias. Therefore, the coefficients represent the usual least squares estimated with this combination.

SECTION 2. THE EFFECT OF FLUID, CONFINING PRESSURE AND TEMPERATURE ON ABSOLUTE PERMEABILITIES OF LOW PERMEABILITY SANDSTONES

A paper containing all details of work on the above topic has been prepared for presentation[2.1] at the forthcoming Annual Meeting of the Society of Petroleum Engineers of AIME, Houston, September 16-19, 1984. We, therefore, limit presentation here to the conclusions of this work. Copies of the full SPE manuscript are available on request.

1. Absolute permeabilities of sandstones to gases and liquids decreased significantly with confining pressure but were essentially independent of temperature. In making permeability measurements, it does not appear necessary to duplicate reservoir temperatures.

2. Liquid permeabilities were generally less than gas permeabilities and decreased with increasing polarity of the liquid. Differences appear to be due mainly to dispersion of fine particles. In general, the effect of ultrasonication appears to cause additional release of fine particles which can disperse in aqueous solution and contribute to the reduced permeabilities generally observed for liquids as compared to those for gas flow.

3. Klinkenberg slip factors (and the slopes of Klinkenberg plots) for a given sample at a given confining pressure are proportional to $\mu\sqrt{T}$, as predicted by Adzumi's equation, rather than T, as follows from the Klinkenberg derivation.

REFERENCE

2.1 Wei, K.K., Morrow, N.R., and Brower, K.R., "The Effect of Fluid, Confining Pressure and Temperature on Absolute Permeabilities of Low Permeability Sandstones," paper SPE 13093 presented at 59th Annual Fall Technical Conference and Exhibition, Houston, TX, Sept. 16-19, 1984.

SECTION 3. EFFECT OF ACID LEACHING AND PRESENCE OF FRACTURES ON PRESSURE SENSITIVITY

An investigation of absolute permeabilities of tight sandstones to various liquids and gases has been reported previously.[1.1,3.1] Measurements of absolute permeabilities have now been extended to the following areas:

- Change in sensitivity of permeability to confining pressure caused by leaching of carbonate cements
- Effect of calcite-filled fractures on permeability and sensitivity to confining pressure

REMOVAL OF CARBONATE CEMENT

In order to help assess the role of carbonate cement on pressure sensitivity, the effect of removing carbonate from cores known to be high in carbonate was carried out by flushing the cores with a known volume of 20% acetic acid. The apparatus used in this work is shown in Fig. 3.1. Acetic acid was driven through the core by gas drive. Removal of carbonate was accompanied by marked increase in permeability. Four high carbonate cores have been tested to date.

RBE-01 (6923.3 ft)

Results are summarized in Table 3.1. This core had extremely low porosity (2.03%) and, after first loading, permeability could not be measured even at the lowest level of overburden. We, therefore, assume $K_{\infty,5000}$ to be < 0.0001 md. This implies pressure sensitivity, as given by the ratio $K_{\infty,500}/K_{\infty,5000}$ on first loading was approximately 34. A first treatment resulted in porosity increasing to 3.84% and permeability rising to 0.225 md at 500 psi confining pressure. Pressure sensitivity on second loading was only 2.15. A second treatment raised $K_{\infty,500}$ by almost a factor of ten, whereas $K_{\infty,5000}$ rose from 0.1 to 0.36 md. Thus, the pressure sensitivity was raised from 2.15 to 5.3 by the second acetic acid treatment. This was somewhat surprising. However, overall, leaching resulted in about an order of magnitude reduction in pressure sensitivity.

Mobil 26-7G (3309.0 ft)

Acetic acid treatment raised the porosity of this core from 4.82% to 7.82%. $K_{\infty,500}$ rose from 0.087 md to 5 md (see Table 3.2). First loading pressure sensitivity increased, but the more significant second loading value fell from 6 to 1.54. As with the RBE-01 core, removal of carbonate changed the core from being relatively pressure sensitive to relatively insensitive.

Arco-Exxon L-36 (3701.0 ft)

The behavior of this core was comparable to that of the Mobil 26-7G core. From Table 3.3 it is seen that a 1.75% increase in porosity from 3.42% to 5.17% by leaching increased K_{500} by 1,000 times. Pressure sensitivity for first loading was reduced from 35 to 3 and for second loading was reduced from 8.18 to 1.49.

RBE-01 (5863.6 ft)

Results for core RBE-01 are summarized in Table 3.4. A first treatment of this core increased the porosity by only 0.56% of the total sample volume but raised the permeability at 500 psi confining pressure (second loading) by a factor of 2.3. Pressure sensitivity decreased from 20.0 to 12.73. Further leaching increased the porosity from 5.46 to 5.89% and further reduced the pressure sensitivity, the change for second loading being from 12.73 to 7.69. This almost halved the second loading pressure sensitivity, but it was still high in comparison with the other treated cores.

Discussion

Mineral analysis of the tested samples (see Table 1.2) shows that the carbonate content of the core samples ranged from 8 to 20 times the amount of carbonate removed by acid leaching. Thus, only a relatively small amount of carbonate was removed. Inspection of thin sections prepared prior to leaching showed the sandstone matrix for the various samples had undergone varying degrees of compaction, prior to deposition of the carbonate.

The sample RBE-01 (6923.3 ft) had essentially no visible compaction of the sandstone grains prior to invasion by the carbonate, and this sample had the lowest initial porosity. Treatment with acid caused the pressure sensitivity to decrease, but then increase, indicating that the pathway developed by the leaching process also developed pressure sensitivity. This suggests that the paths leached out are themselves pressure sensitive and are likely to have high aspect ratios.

Thin sections of the samples Mobil 26-7G and Arco-Exxon L-36 showed the basic grain structure to be only lightly compacted. Both of these cores showed dramatic but similar increases in permeability and reductions in pressure sensitivity as a result of acid leaching.

The sample RBE-01 (5863.6 ft) was the most compacted suggesting late arrival of the carbonate cement. The reductions in pressure sensitivity from 20 to 12.73 and then after a second treatment to 7.69 is consistent with the compacted grain framework still providing significant sensitivity along with only relatively modest increases in permeability.

Conclusions

We conclude from these studies that the presence of carbonate cement may contribute very significantly to pressure sensitivity and that removal of a comparatively small volume of cement can result in dramatic increase in permeability and reduction in pressure sensitivity. These observations are qualitatively consistent with the identification of carbonate cement content as being important in correlations of pressure sensitivity with measurable core properties. However, because only a small fraction of the carbonate cement was removed by leaching, further investigation is needed to determine the nature of the etched flow paths and their relationship to the grain structure of the sample as revealed by thin sections. The extreme pressure sensitivity of cores high in carbonate suggests that their permeabilities are controlled by very high aspect ratio sheet pores given by carbonate overgrowth on the basic grain framework of the rock. Comparable tests will be run on the Multi-Well samples in order to determine the extent to which carbonate in these cores is responsible for their generally high pressure sensitivity.

EFFECT OF CALCITE-FILLED FRACTURES ON PERMEABILITY AND SENSITIVITY TO CONFINING PRESSURE

Permeabilities measured for rock matrix obtained from Mesa Verde rocks from the MWX site (Garfield County, Colorado) are generally very low. In contrast, production of gas from these wells is one to two orders of magnitude higher than predicted from models based on measured permeabilities. The whole core samples taken from these wells often show numerous fractures, most of which are filled by calcite cement. An investigation has therefore been undertaken into the flow properties of these fractures.

Several whole core samples have been obtained, which from inspection, contained calcite-filled fractures. All fractures lay in a direction close to the axis of the whole core samples. In some cases it was not possible to cut the test sample without fracturing the core along the naturally cemented fracture zone. Cores were cut with the fracture lying either along or across the main axis of the core plug, as shown in Fig. 3.2, and were designated as V* and H* respectively. Unfractured plugs were also cut adjacent and parallel to the fractured samples for the purpose of making comparative permeability measurements. These plugs were designated as horizontal, H, or vertical, V.

(MWX-1) 34-10

Results for the (MWX-1) 34-10 samples are presented in Table 3.5. The vertical plugs with and without fracture exhibited almost identical permeability behavior, suggesting that the fracture permeability was approximately or equal to the matrix permeability. Pressure sensitivity behavior was similar for both cores. The horizontal plug with the fracture was of lower permeability than the horizontal plug from the

matrix indicating that the fracture permeability may be less than the matrix. Pressure sensitivities were again similar for both cores.

(MWX-1) 21-4A

Results for this core, given in Table 3.6, show the fractured sample to be highly sensitive to overburden pressure on first loading. On second loading, pressure sensitivities were comparable. It appears that the calcite-filled fracture provides a relatively high permeability streak which is more sensitive to overburden pressure than the surrounding matrix, particularly on first loading.

(MWX-1) 13-18

Results for the (MWX-1) 13-18 samples are summarized in Table 3.7. Vertical permeabilities for the core with fractures are at least four times higher than those of the surrounding matrix. This core was highly pressure sensitive, the second loading ratio $K_{\infty,500}/K_{\infty,5000}$ of 30.4 being the highest we have yet observed.

The horizontal permeability and pressure sensitivity of the matrix were comparable to values observed for vertical plugs (i.e., plugs cut along the axis of the whole core samples). Flow rates were so low that measured pressure sensitivities should be regarded as approximations.

(MWX-1) 29-31

Results (see Table 3.8) for the vertical plug with fractures indicate that the fracture acted as a moderately high permeability streak which approximately doubled the permeability measured for the matrix. Pressure sensitivity was about the same as that of the matrix for both V* and V.

Treatment with Acetic Acid

A vertical plug was cut from sample (MWX-1) 13-18 with a fracture running along the core. Treatment of this sample by flushing with 1 PV of 20% acetic acid caused a 10,000-fold increase in permeability ($K_{\infty,5000}$) and dramatic decrease in pressure sensitivity ($K_{\infty,500}/K_{\infty,5000}$ for second loading fell from 30 to 2.1). Porosity was increased only from 4.06 to 5.41% (see Table 3.9). The effect of acetic acid on matrix permeability will be studied further through preparation of pore casts. Tests will also be made on vertical plugs which do not contain fractures in order to assess the contribution to permeability that resulted from partial leaching of the calcite contained in the fracture. Comparable results have also been obtained by acid leaching of cores that were high in carbonate content.

Conclusions

The reported data are for the first fractured samples to be tested. Results and their interpretation are preliminary. However, it does appear that a fracture neither acts as a severe permeability barrier for flow across the cement nor as a highly conductive region for flow along the fracture. Further testing is in progress. In particular, more detailed information is being obtained on the permeability of the calcite-filled zone and the possible presence of relatively high conductivity flow paths through a given core. The effect of connate water on flow in fractured cores will also be investigated.

REFERENCE

3.1 Morrow, N.R., Brower, K.R., and Kilmer, N.H., "Relationship of Pore Structure to Fluid BEhavior in Low Permeability Gas Sands," Western Gas Sands Subprogram Review Technical Proceedings, (K-H. Frohne, ed.) (Jan. 1984) 109-124.

Table 3.1 Summary of Core Properties (Measured at Ambient Temperature and 500 psi Overburden Pressure)

Core Sample and Depth (ft)	Length (cm)	Diameter (cm)	Porosity (%)	Permeability (md)	$\frac{K_{\infty,500}}{K_{\infty,5000}}$	K_w Brine (md)	K'_w Water (md)
Old Man Mountain #2 (4498)	2.33	1.275	14.58	5.84	1.87	3.21	-
10570 S BETC (10570)	2.68	1.275	4.27	0.00235	3.95	-	-
CIGE 21 (4403.3)	2.47	1.275	12.19	1.25	2.17	0.405	0.198
U78JP16 (8265.1)	2.175	1.275	7.47	0.0205	6.613	0.001	-
(MWX-2) 48-9 (5731)	2.16	1.28	8.31*	0.007	8.81	-	-
(MWX-2) 56-19 (7878.7)	3.35	1.345	6.97*	0.0029*	17.54*	0.002	-
(MWX-2) 56-19 Fired (7878.7)	3.36	1.345	-	-	-	0.001	-
Berea Sandstone	3.11	1.33	-	113.1	1.1333	94.48	46.47

* Core data from "Relationship of Pore Structure to Fluid Behavior in Low Permeability Gas Sands," Report No. DOE/BC/10216-14.

TABLE 3.2 RBE-01 (6923.3 ft)

EFFECT OF CARBONATE REMOVAL BY ACETIC ACID

Sample	% Porosity	First Loading			Second Loading		
		$K_{\infty},500$ (md)	$K_{\infty},5000$ (md)	$\frac{K_{\infty},500}{K_{\infty},5000}$	$K_{\infty},500$ (md)	$K_{\infty},5000$ (md)	$\frac{K_{\infty},500}{K_{\infty},5000}$
RBE-01 (Untreated)	2.03	<0.0034	0.0001	~34.0			
RBE-01 (Treated)*	3.84	0.225	0.10	2.25	0.198	0.092	2.15
RBE-01 (Treated)**	4.02	1.95	0.36	5.41	1.75	0.33	5.30

* Acetic acid treatment

** Second treatment

TABLE 3.3 MOBIL 26-7G (3309 ft)

EFFECT OF CARBONATE REMOVAL BY ACETIC ACID

Sample	% Porosity	First Loading			Second Loading		
		$K_{\infty},500$ (md)	$K_{\infty},5000$ (md)	$\frac{K_{\infty},500}{K_{\infty},5000}$	$K_{\infty},500$ (md)	$K_{\infty},5000$ (md)	$\frac{K_{\infty},500}{K_{\infty},5000}$
Mobil 26-7G (Untreated)	4.82	0.087	0.00084	10.4	0.048	0.008	6.00
Mobil 26-7G (Treated)	7.82	5.00	0.176	28.41	0.20	0.13	1.54

* Acetic acid treatment

TABLE 3.4 ARCO EXXON L-36 (3701 ft)

EFFECT OF CARBONATE REMOVAL BY ACETIC ACID

Sample	% Porosity	First Loading			Second Loading		
		$K_{\infty,500}$ (md)	$K_{\infty,5000}$ (md)	$\frac{K_{\infty,500}}{K_{\infty,5000}}$	$K_{\infty,500}$ (md)	$K_{\infty,5000}$ (md)	$\frac{K_{\infty,500}}{K_{\infty,5000}}$
Arco Exxon L-36 (Untreated)	3.42	0.012	0.00034	35.3	0.0018	0.00022	8.18
Arco Exxon L-36 (Treated)*	5.17	3.60	1.20	3.00	1.70	1.14	1.49

* Acetic acid treatment

TABLE 3.5 RBE-01 (5863.6 ft)

EFFECT OF CARBONATE REMOVAL BY ACETIC ACID

Sample	% Porosity	First Loading			Second Loading		
		$K_{\infty},500$ (md)	$K_{\infty},5000$ (md)	$\frac{K_{\infty},500}{K_{\infty},5000}$	$K_{\infty},500$ (md)	$K_{\infty},5000$ (md)	$\frac{K_{\infty},500}{K_{\infty},5000}$
RBE-01 (Untreated)	4.903	0.023	0.00054	43.2	0.012	0.0006	20.0
RBE-01 (Treated)*	5.46	0.065	0.0022	29.55	0.028	0.0022	12.73
RBE-01 (Treated)**	5.89	0.080	0.0045	17.78	0.040	0.0052	7.69

*Acetic acid treatment

**Second treatment

TABLE 3.6 MULTI-WELL FRACTURED SAMPLE MWX-1 34-10

(6002.3-6002.5 ft)

Core	% Porosity	First Loading			Second Loading		
		$K_{\infty,500}$ (md)	$K_{\infty,5000}$ (md)	$\frac{K_{\infty,500}}{K_{\infty,5000}}$	$K_{\infty,500}$ (md)	$K_{\infty,5000}$ (md)	$\frac{K_{\infty,500}}{K_{\infty,5000}}$
V*	4.57	0.0043	0.00032	13.44	0.0017	0.00032	5.31
V	4.50	0.0044	0.00024	18.33	0.0013	0.00029	4.48
H*	4.52	0.021	0.0012	17.50	0.0076	0.0011	6.91
H	4.97	0.060	0.0020	30.00	0.0180	0.0025	7.20

V* = Vertical; cored along the fracture
V = Vertical; without the fracture
H* = Horizontal; cored across the fracture
H = Horizontal; without the fracture

Porosities were all low; pressure sensitivities were not dependent on fracture

V* vs. V, Fracture K $\leq$ Matrix K; H* vs. H, Fracture K $<$ Matrix K

TABLE 3.7 MULTI-WELL FRACTURED SAMPLE MWX-1 21-4A

(5271.6-5272 ft)

Core	% Porosity	First Loading			Second Loading		
		$K_{\infty},500$ (md)	$K_{\infty},5000$ (md)	$\frac{K_{\infty},500}{K_{\infty},5000}$	$K_{\infty},500$ (md)	$K_{\infty},5000$ (md)	$\frac{K_{\infty},500}{K_{\infty},5000}$
V*	3.69	0.0115	0.00004	287.500	0.0024	0.00025	9.60
V	4.70	0.0011	0.00012	9.167	0.00113	0.00015	7.533

V* = Vertical; cored along the fracture

V = Vertical; without the fracture

Fracture K > Matrix K, mainly first loading

Very high pressure sensitivity on first loading of sample with fracture

TABLE 3.8 MULTI-WELL FRACTURED SAMPLE MWX-1 13-18

(4846.5-4847 ft)

Core	% Porosity	First Loading			Second Loading		
		$K_{\infty},500$ (md)	$K_{\infty},5000$ (md)	$\frac{K_{\infty},500}{K_{\infty},5000}$	$K_{\infty},500$ (md)	$K_{\infty},5000$ (md)	$\frac{K_{\infty},500}{K_{\infty},5000}$
V*	4.06	0.0152	0.000076	200.0	0.0031	0.000102	30.4
V	4.63	0.0030	0.0001	30.0			
H*	4.41	0.0088	0.00017	51.76	0.00085	0.00015	5.7
H	3.64	0.0026	0.0001	26.0			

V* = Vertical; cored along the fracture

V = Vertical; without the fracture

H* = Horizontal; cored across the fracture

H = Horizontal; without the fracture

V* vs. V, Fracture K > Matrix K; H* vs. H, Fracture does not inhibit flow

Fracture K > Matrix K but note low porosity of H sample

TABLE 3.9 MULTI-WELL FRACTURED SAMPLE MWX-1 29-31

(5730.9-5731.2 ft)

Core	% Porosity	First Loading			Second Loading		
		$K_{\infty},500$ (md)	$K_{\infty},5000$ (md)	$\frac{K_{\infty},500}{K_{\infty},5000}$	$K_{\infty},500$	$K_{\infty},5000$	$\frac{K_{\infty},500}{K_{\infty},5000}$
V*	7.01	0.036	0.0013	27.69	0.017	0.00105	16.19
V	7.10	0.0155	0.00055	28.18	0.007	0.00045	15.56

V* = Vertical; cored along the fracture

V = Vertical; without the fracture

Comparatively high porosity (>5%) but permeabilities are still low

Fracture K > Matrix K

Equally sensitive to overburden

TABLE 3.10 MULTI-WELL FRACTURED SAMPLE MWX-1 13-18
(4846.5-4847 ft)
EFFECT OF ACETIC ACID TREATMENT

Core	% Porosity	First Loading			Second Loading		
		$K_{\infty},500$ (md)	$K_{\infty},5000$ (md)	$\frac{K_{\infty},500}{K_{\infty},5000}$	$K_{\infty},500$ (md)	$K_{\infty},5000$ (md)	$\frac{K_{\infty},500}{K_{\infty},5000}$
V*	4.06	0.0152	0.000076	200.0	0.0031	0.000102	30.39
V*AT	5.41	4.50	1.40	3.21	2.10	1.0	2.10

V* = Vertical; cored along the fracture

V*AT = V* treated with acetic acid

Acid treatment increased porosity by 1.4%

Increased permeability by over 10,000 times

Cut pressure sensitivity from 30 to 2

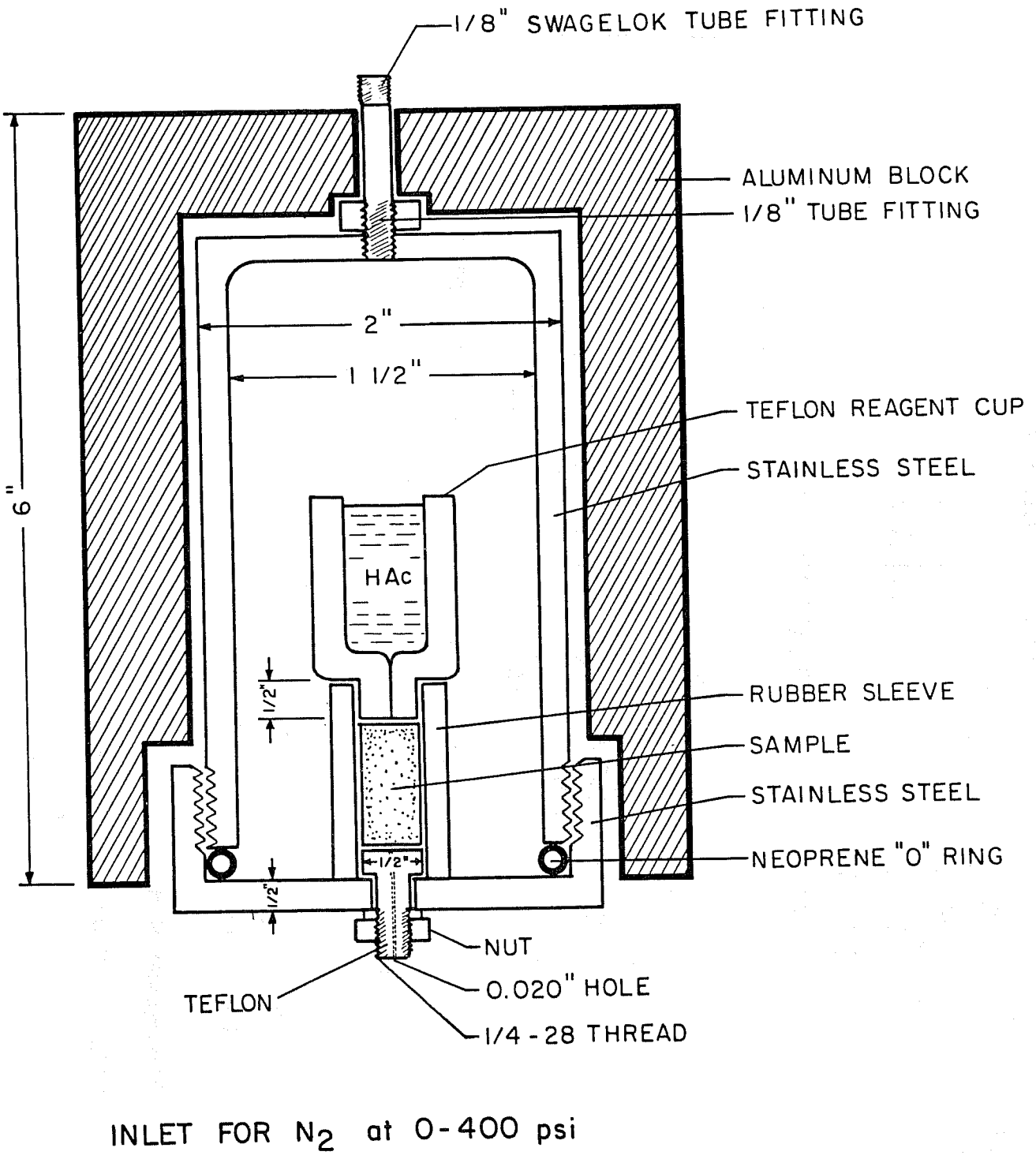

Fig. 3.1 Apparatus used to flush cores with acetic acid.

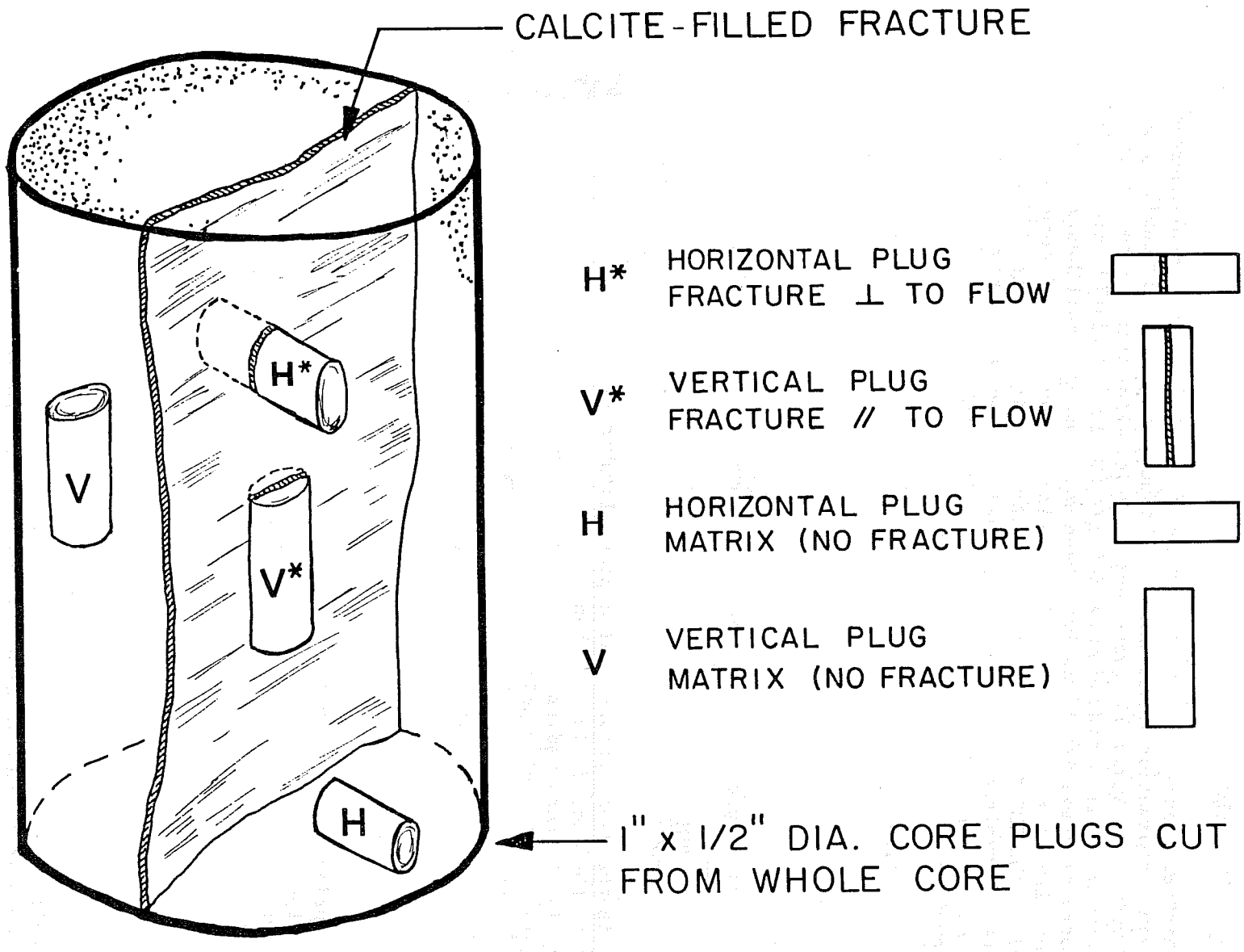

Fig. 3.2 Configuration of core cut from whole core sample which contains a calcite-filled fracture.

SECTION 4. ADSORPTION

It has been found that adsorption behavior provides a useful approach to obtaining information about the pore structure of low permeability gas sands. Cores are generally very hygroscopic with dried cores gaining weight rapidly in atmospheres of quite low (~50%) humidity. Adsorption-desorption isotherms have been measured by equilibrating cores at various levels of humidity. The surface areas of the core samples (measured by the BET method and by hydrogen-deuterium exchange[1.1]) are not sufficient to explain the observed amounts of water uptake as being surface adsorption. This, together with observed hysteresis, strongly suggest capillary condensation.

Relative humidity, H_R, is directly related to the vapor pressure, p, by

$$H_R = \frac{p}{p_o} 100 \tag{4.1}$$

Lowering of vapor pressure is related to curvature by the Kelvin equation

$$\frac{p}{p_o} = e^{\frac{-2\sigma M}{r\rho RT}} \tag{4.2}$$

where p_o is the vapor pressure at a plane interface
σ is the interfacial tension
r_c is the mean radius of curvature of the interface
M is the molecular weight
ρ is the density of the liquid

Since capillary pressure, P_c, is given by

$$P_c = \frac{2\sigma}{r} \tag{4.3}$$

the adsorption isotherms provide a method of obtaining capillary pressure relationships pertaining to the microporosity of the system. Micropores can be roughly defined as pores of less than 100 nm diameter. For a crack-shaped pore of width d, the capillary pressure is given by

$$P_c = \frac{2\sigma}{d} \tag{4.4}$$

Several interrelated topics which involve adsorption measurements are now being studied. These include: adsorption-desorption characteristics of tight sands for both water (polar) and organic (nonpolar) vapors; relationships between surface area, adsorption, microporosity and clay content; changes in gas permeability vs. water saturation (i.e., relative permeabilities to gas) with water content established by capillary condensation; obtaining capillary pressure relationships over an extremely wide range of pressures by combination of high-speed centrifuge measurements and desorption isotherms; and changes in permeability,

surface areas and adsorption behavior which accompany firing of core samples. Parts of this work, such as the centrifuge and relative permeability work, were begun quite recently and will be continued in proposed future work. Areas in which substantial progress or interesting preliminary observations have been made are described below.

EXPERIMENTAL

A series of relative humidity chambers were set up with humidity control being obtained by dilutions of concentrated sulfuric acid[4.1] (see Fig. 4.1). Concentrations were chosen to give humidity levels of 20%, 40%, 60%, 75%, 90%, 95% and 98%. Samples were weighed and were either initially dry or were saturated with distilled water. After weighing, the core was introduced into the desired humidity chamber and weighed periodically, typically at 2 to 3 day intervals. Once constant weight was achieved, the core was moved to the next desired humidity condition, and the process was repeated. The volume of sulfuric acid solution was such that change in relative humidity caused by uptake or loss of water from the core was negligible. Each chamber contained a control sample which, by maintaining constant weight, demonstrated that a desired humidity condition was maintained.

Adsorption data was also obtained for one core sample with heptane. Vapor pressure of the heptane was controlled by temperature. An apparatus was designed for suspending a core sample in a thermostatted space above a liquid reservoir which was maintained at a controlled lower temperature. By varying the temperatures from 0 to 50°C, it is possible to achieve a wide range of relative pressures. The Clapeyron equation was used to calculate the vapor pressures at the upper and lower temperatures, and the relative pressure, p/p_o, was derived therefrom. A core sample was dried under vacuum, weighed, and placed in the apparatus. The vapor space was evacuated, sealed, and allowed to equilibrate for several hours. The core sample was removed, and the weight increase was determined by weighing. The weighing was done as rapidly as possible in order to minimize change caused by evaporation. Measured rates of evaporation indicated that the change of weight during weighing was less than one milligram.

RESULTS

Adsorption Isotherms for Water

Three typical sets of adsorption-desorption isotherms for Multi-Well (MWX-2) core samples are shown in Fig. 4.2. Measurements were commenced using initially dry cores that were equilibrated at 20% relative humidity. Hysteresis was exhibited in all cases. At 90% relative humidity, pore space saturation ranged from 13% to 21%. This humidity corresponds to equivalent pore radii (assuming a circular capillary and contact angle of zero) of only about 10 nm.

A further series of desorption measurements were made beginning with a completely saturated (MWX-1) 42-25 core from which water was desorbed by equilibration at 98% relative humidity. Results are shown in Fig. 4.3. Associated liquid curvatures at this humidity correspond to pore radii of about 50 nm. It was found that the core retained a 42% water saturation in space which was either microporous or only accessible through microporous space. At 20% relative humidity, the water saturation was 4%. Adsorption onto a dry core gave 20% saturation at 90% relative humidity and hysteresis that was typical of that observed previously[1.1] MWX-2 cores (Fig. 4.2).

Desorption experiments from initially saturated cores were also carried out on the four cores listed in Fig. 4.4, and the results provide examples of high water saturations retained at 98% relative humidity. Samples of higher permeability (and porosity) retained much less water at both high and reduced humidities. One of these cores (6405) had a BET surface area which was close to those measured for the MWX samples (about 2 m^2/gm).

Heptane Adsorption

Results for sorption of heptane are shown in Fig. 4.5. These experiments were carried out on an (MWX-1) 14-14 core for which x-ray analysis had shown the presence of montmorillonite. Adsorption at low humidity indicated that the sample had roughly the same adsorptive capacity per unit surface area (BET method) as a sample of montmorillonite (Clay Spur, Wyoming). If the matter responsible for adsorption in the MWX sample were the same as the montmorillonite, it would be present in the amount of 7% by weight. This is unlikely. Thus, capillary condensation of heptane is the likely cause of the observed adsorption capacity.

Treatment with $(CH_3)_4NCl$

It is reported that replacement of adsorbed cations by tetramethylammonium ion increases the spacing of layered clays to such a degree that the interior becomes accessible to adsorption of nitrogen and even small hydrocarbon molecules.[4.2] We verified the phenomenon with heptane adsorption on the sample of Clay Spur montmorillonite (see Table 4.1).

A sample of (MWX-1) 14-14 (depth 4917.0-4917.9 ft) was treated with tetramethylammonium chloride. Heptane adsorption by this core sample after treatment is shown by open circles and the dashed line in Fig. 4.5. The weight of the core was 9.4025 g, as before. Results were compared with adsorption data obtained before treatment (see Fig. 4.5). There is an indication that some of the adsorption may be due to swellable layered minerals similar to montmorillonite. However, it appears for the most part that the heptane adsorption-desorption behavior is comparable to that observed for water. This again suggests that capillary condensation is the dominant mechanism for adsorption.

Effect of Firing

It is common laboratory practice to fire sandstones at about 1000°C in order to stabilize mineral matter that might otherwise give rise to inconsistent results in various types of flow experiments. Results of the effect of firing on stress sensitivity of permeability have been reported previously.[1.1] The most dramatic change in properties occurred in increasing the temperature of firing from 900 to 1000°C. Permeability over that of the original rock increased by a factor of 100 (at 500 psi overburden) to 400 (at 5000 psi overburden). This was accompanied by a very marked decrease in pressure sensitivity ($K_{\infty,500}/K_{\infty,5000}$ dropped from about 10 down to about 2).

Adsorption-desorption isotherms have been measured for four of these cores. Results are presented in Fig. 4.6. It is seen that the amount of water adsorbed at 90% relative humidity decreases systematically with increase in firing temperature, but for the temperature levels tested (500, 700 and 1000°C), the effect is relatively small except for the core fired at 1000°C. Firing at 1000°C reduced the amount of capillary condensation to less than 1% of the pore space, indicating that the microporosity was largely destroyed by the high temperature firing.

CONCLUSIONS

1. Adsorption-desorption isotherms can be measured for low permeability sandstones. Hysteresis in adsorption isotherms and their similarity for water and heptane (respectively polar and nonpolar liquids) suggest that adsorption is dominated by capillary condensation.

2. Measurement of desorption isotherms offers a useful method of extending capillary pressure curves measured, for example, by high speed centrifuge, to extremely high capillary pressures.

3. Up to 50% of the pore space of low permeability gas sands has been observed to retain water at 98% relative humidity, which corresponds to water held in spaces with pore entrance diameters of less than 100 nm. Water retained in microporosity, provided by material such as chert rather than clays, provides an explanation of the high connate water saturations generally associated with low permeability gas sands.

4. Sorption isotherm measurements provide valuable information on relationships between water retention and pore size, and are a useful complement to surface area and relative permeability measurements in developing an understanding of water distribution and its effect on gas flow. These measurements provide a particularly useful guide to the minimum amount of connate water likely to be found in a gas reservoir. The large proportion of pore space taken up by microporosity (somewhat arbitrarily defined as pores of less than 100 nm diameter, or pores only accessible by pores of this size) provides explanation of the relative

insensitivity of connate water saturation to height of closure in the reservoir.

5. Sorption isotherms for fired cores show that microporosity responsible for capillary condensation is essentially eliminated by firing a core at 1000°C.

REFERENCES

4.1 Weast, R.C., (ed.) and Astle, M.J. (assoc. ed.), "CRC Handbook of Chemistry and Physics," 63rd Edition, 1982-1983, CRC Press, Inc. (Boca Raton, FL, 1982) D-271 and E-43.

4.2 Barrer, R.M. and Kelsey, K.E., "Thermodynamics of Interlamellar Complexes. Part I. - Hydrocarbons in Methylammonium Montmorillonites," Trans. Faraday Soc. 57 (1961) 452-462.

Table 4.1 Effect on Heptane Adsorption of Treating Montmorillonite* with Tetramethylammonium Chloride

Relative pressure	Adsorption, mg/g	
	Untreated	Treated
0.62	21.0	67.2, 70.2
0.73	24.9	----
0.74	----	73.0 **

* Clay Spur, Wyoming

** At the same relative pressure, Barrer and Kelsey[4.2] report 80 mg/g for a treated montmorillonite.

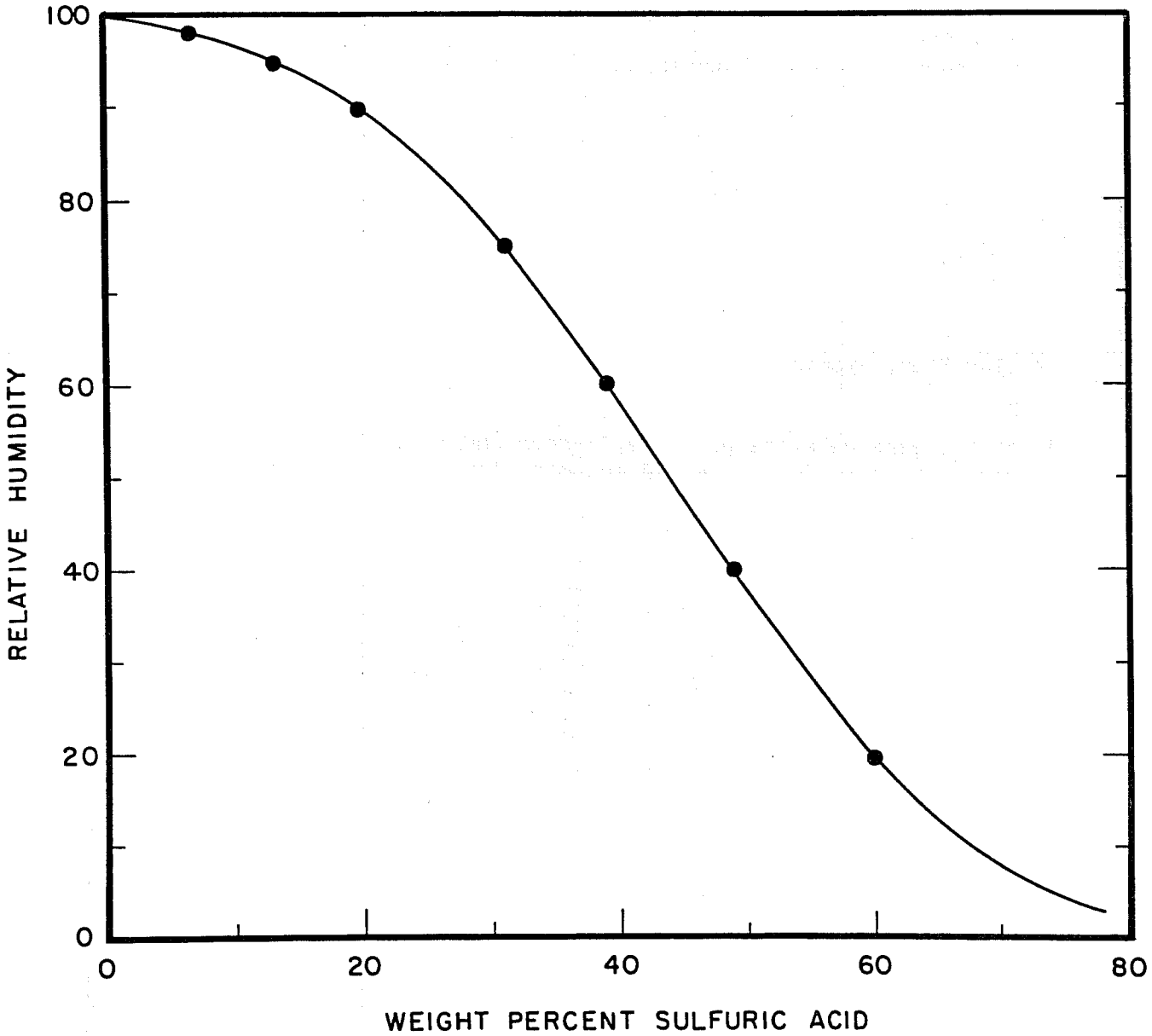

Fig. 4.1 Relative humidity of air in equilibrium with aqueous solutions of sulfuric acid.

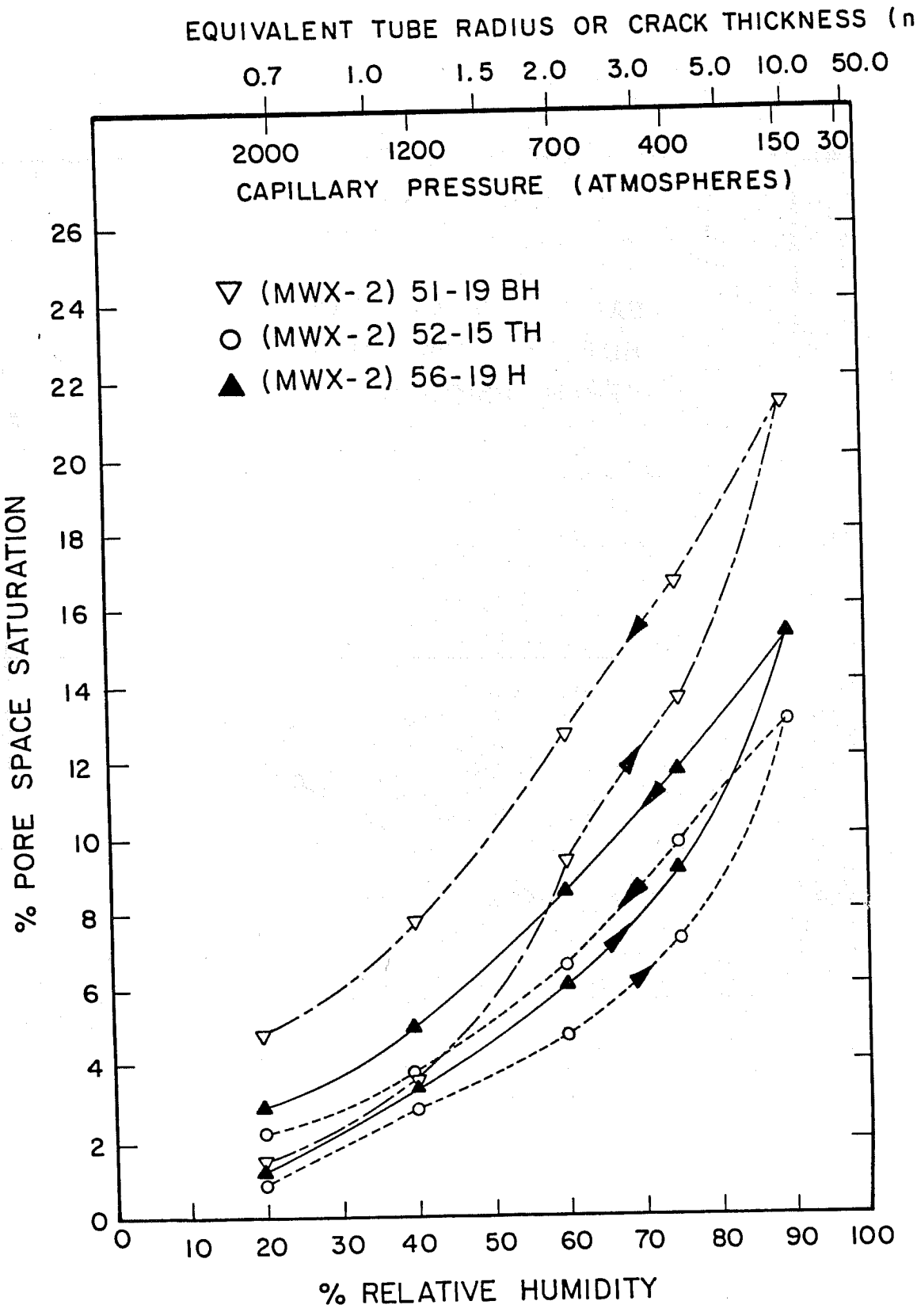

Fig. 4.2 Percent of pore space occupied by water vs. relative humidity of air that surrounds core. Top scales show values corresponding to those relative humidities for straight capillaries or cracks.

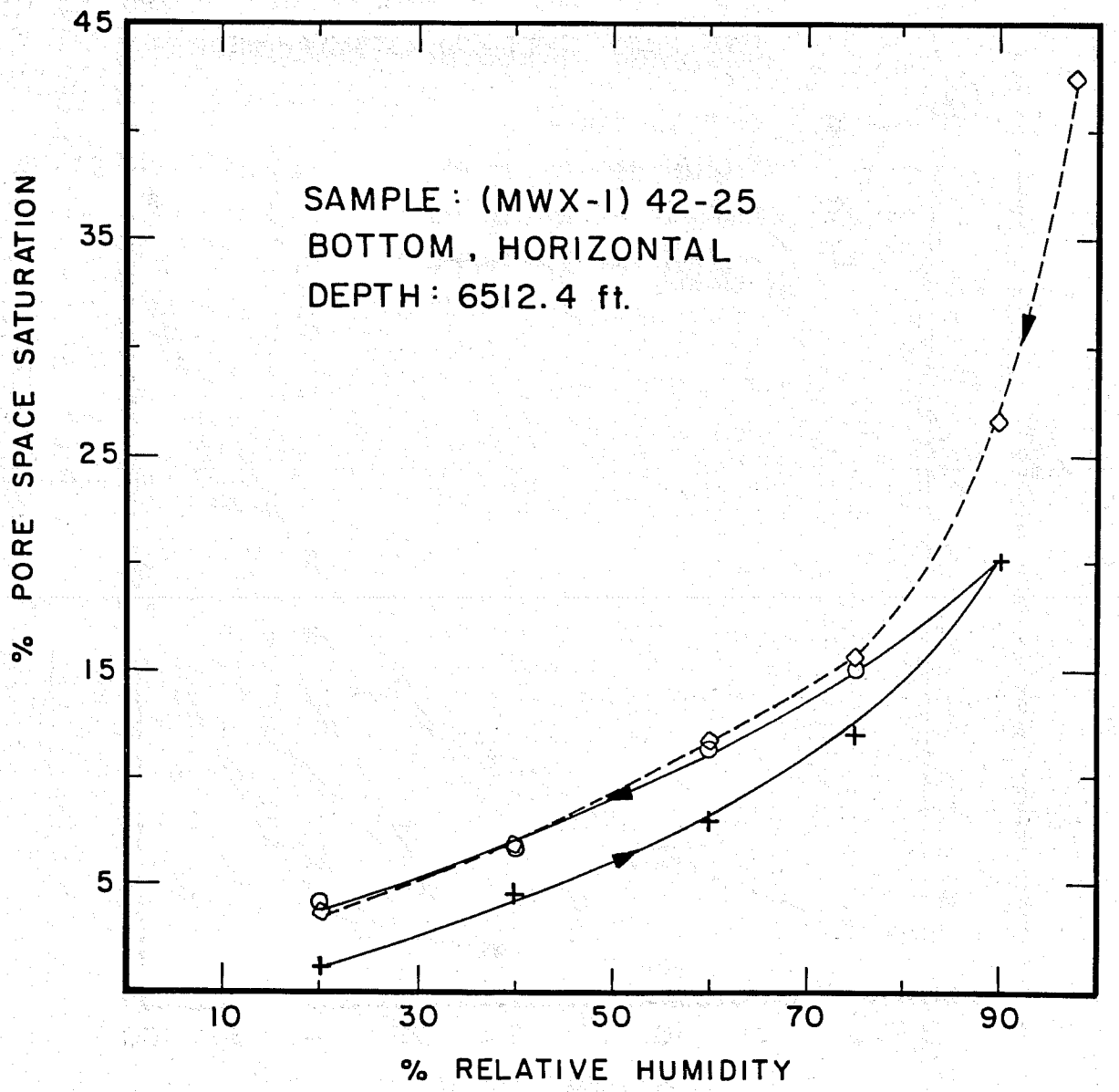

Fig. 4.3 Percent of pore space occupied by water vs. relative humidity of air surrounding core.

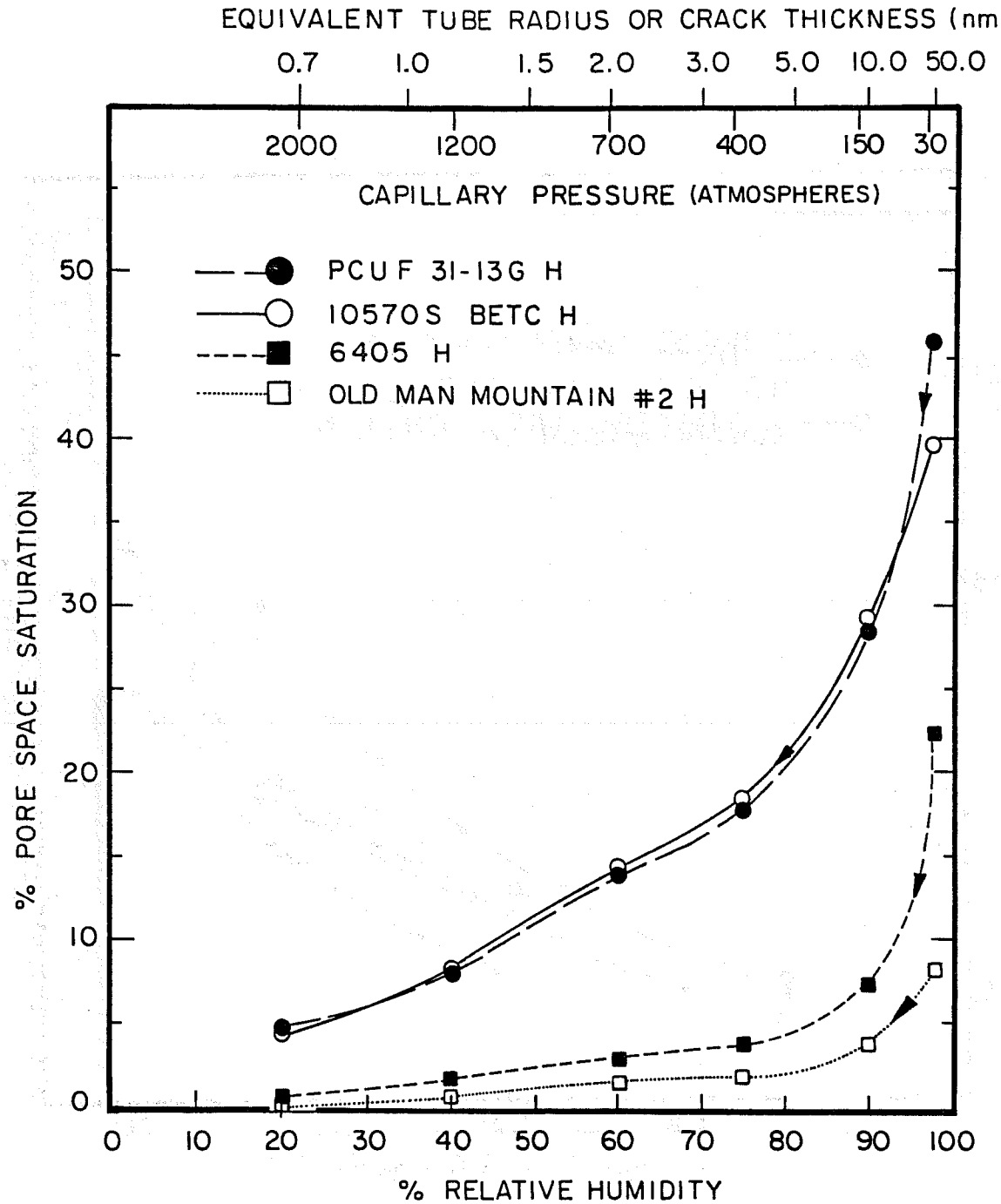

Fig. 4.4 Percent of pore space occupied by water vs. relative humidity of air that surrounds core.

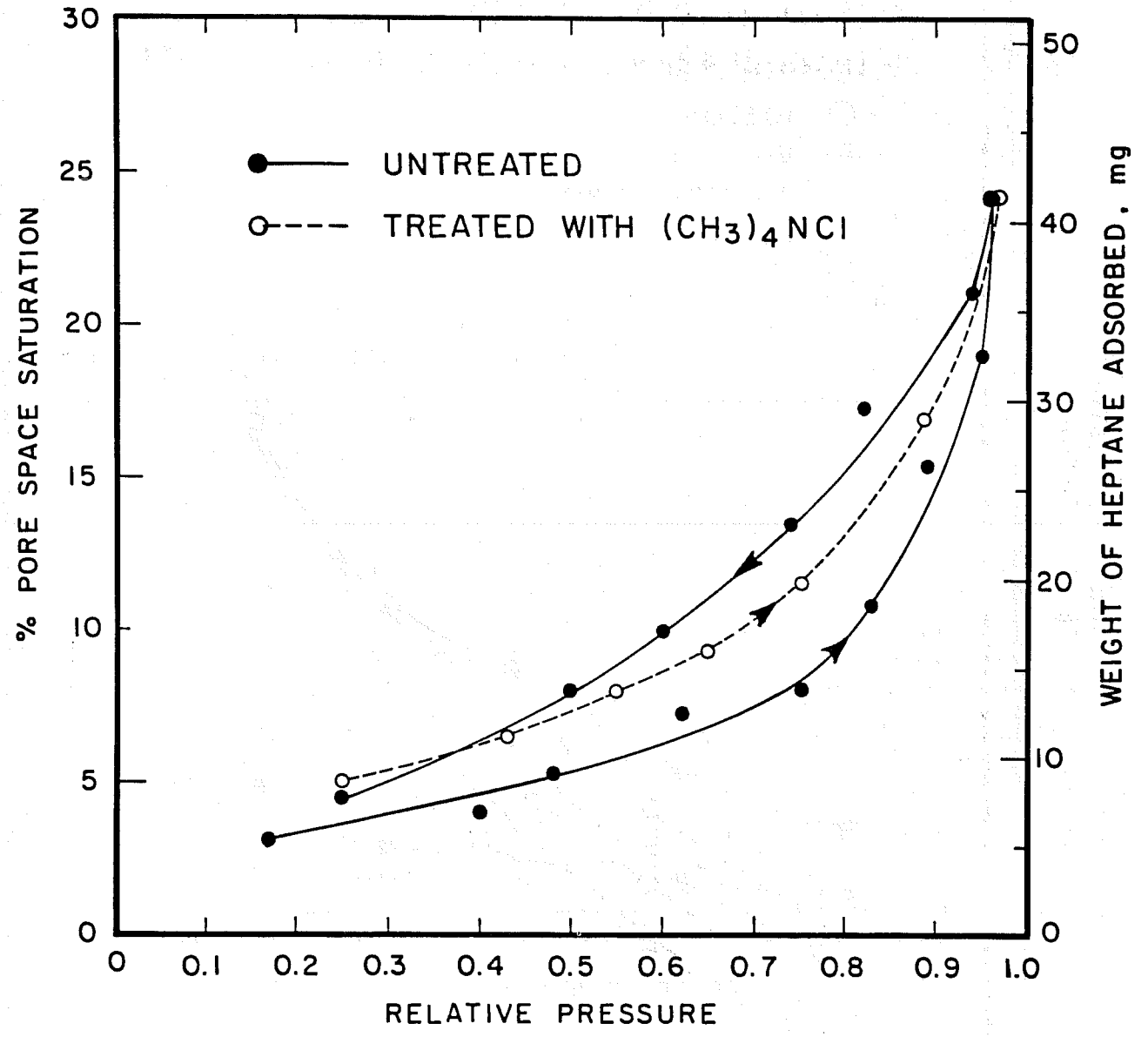

Fig. 4.5 Amount of sorbed heptane in an (MWX-1) 14-14 core sample before and after treatment by tetramethylammonium chloride. This amount is plotted against relative pressure of heptane vapor.

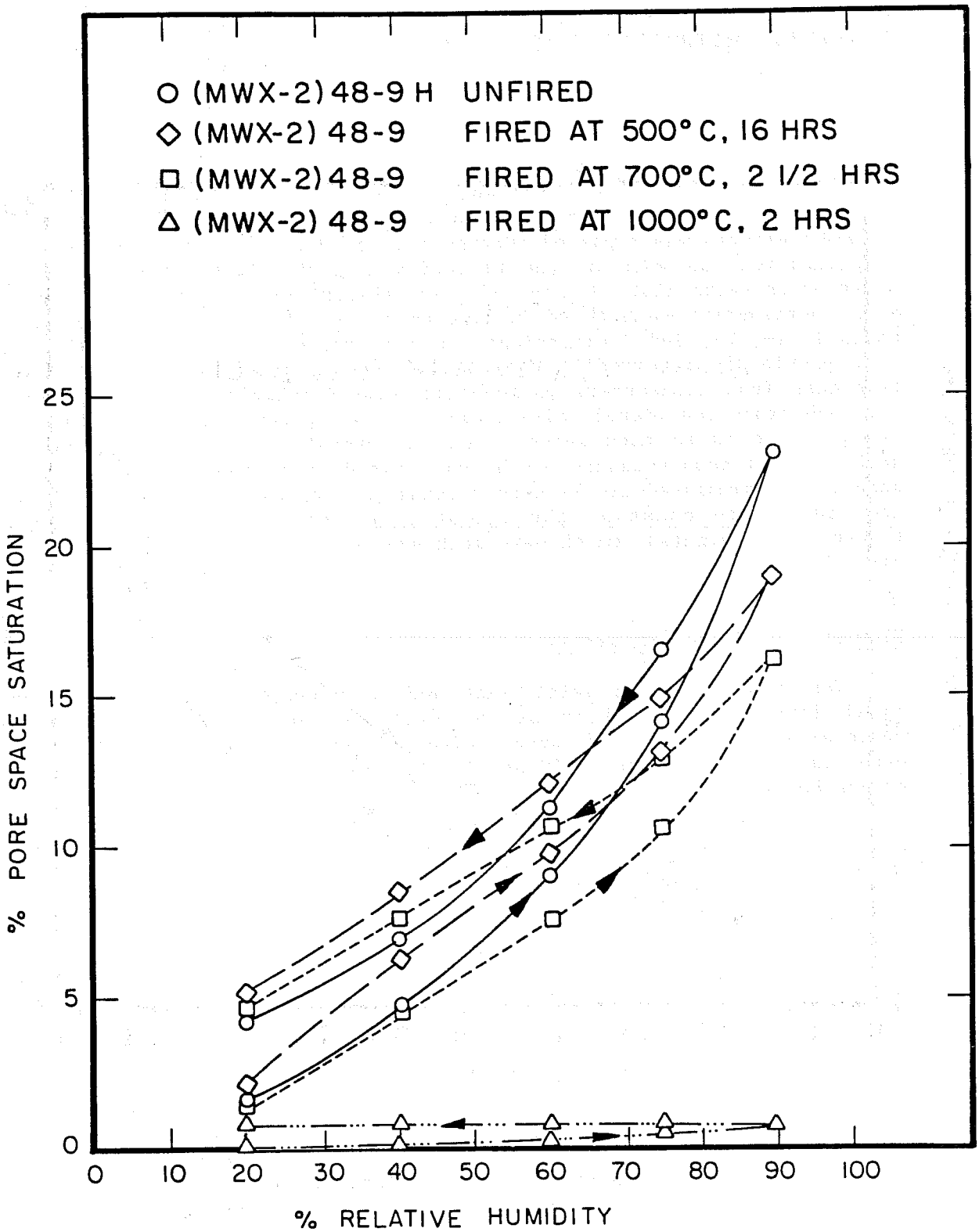

Fig. 4.6 Effect of firing on adsorption-desorption isotherms of (MWX-2) 48-9 core material.

Fluid Flow in Networks of Cracks

In developing an explanation of sensitivity of permeability to overburden pressure, special attention was given to flow in crack-shaped pores. A method of estimating an average crack thickness from gas slippage effects was reported previously.[1,2] More recently, a theoretical investigation was made of the effective crack thickness that would be given by assuming distributions of crack thicknesses in multi-crack models with coordination numbers of 2, 4, and 6 for the completely surrounded nodes in 1-, 2-, and 3-dimensional models, respectively. It was assumed that previously reported[1,2] equations for estimating an average crack thickness from Klinkenberg permeability and Klinkenberg slope are valid for each crack considered individually. It also was assumed that the mean gas pressure is so much larger than the overall pressure drop that the same value of mean pressure may be used for each of the cracks in a given model. The simulated cracks were rectangular prisms, for which the length and width were constant throughout a network. However, the crack thicknesses (heights), which were much smaller, were set by choice of size distribution.

Flow Through Cracks in Series

The most primitive multi-crack model, composed of many cracks of equal length connected in series (with no branching), was treated algebraically. Expressions were derived for the "average" crack thickness obtained from gas slippage effects in the entire series of cracks. If the cracks had the same length, but various thicknesses, then

$$H_{calc} = \frac{\sum_{i=1}^{n} \frac{1}{H_i^3}}{\sum_{i=1}^{n} \frac{1}{H_i^4}} \qquad (5.1)$$

where H_i is the actual thickness of the ith crack, n is the total number of cracks in series, and H_{calc} is the crack thickness calculated from a Klinkenberg plot. If there are a very large number of cracks, then the summations can be approximated by integrals. In this case,

$$H_{calc} \approx \frac{\int_0^{+\infty} \frac{\psi(H)\,dH}{H^3}}{\int_0^{+\infty} \frac{\psi(H)\,dH}{H^4}} \qquad (5.2)$$

where $\psi(H)$ is a normalized probability distribution function such that $\psi(H)dH$ is the probability of the crack thickness being between H and H + dH.

If $\psi(H)$ obeyed a log-normal distribution, then

$$\frac{\psi dH}{d \ln H} = \frac{1}{(\ln \sigma_g) \sqrt{2\pi}} \exp \left[-\frac{1}{2} \left(\frac{\ln H - \ln H_g}{\ln \sigma_g} \right)^2 \right] \tag{5.3}$$

and the integration

$$\int_o^{+\infty} \frac{\psi(H)dH}{H^k}$$

could be performed by a procedure analogous to one given by Allen.[5.1] The result is

$$\int_o^{+\infty} \frac{\psi(H)dH}{H^k} = \exp \left[\frac{k^2}{2} (\ln \sigma_g)^2 - k \ln H_g \right] \tag{5.4}$$

Using 3 and 4 for k and substituting the resulting equations into Eq. 5.2 gives

$$H_{calc} \approx \left[H_g \right] \exp \left[-\frac{7}{2} (\ln \sigma_g)^2 \right] \tag{5.5}$$

This expression was used to determine the effect of the distribution of crack thicknesses on the calculated average crack thickness obtained from gas slippage effects. With crack thicknesses described by a log-normal distribution, the calculated average crack thickness was sensitive to both the geometric mean and the geometric standard deviation of the actual crack thicknesses. For a given value of the actual geometric mean, increase in geometric standard deviation led to decrease in the calculated average crack thickness. Results for standard deviations of the natural logarithm of H_i of 0.3, 0.5, and 0.7 are presented in Fig. 5.1. Values of average crack thickness calculated for purely viscous flow are also indicated for comparison. In Fig. 5.2, the simulated estimates of crack thickness are plotted against the standard deviation of the logarithm of crack thickness.

It is recognized that this model is a limiting case which will overestimate the importance of very narrow cracks. In an actual core

sample, the narrower cracks would tend to be bypassed. Therefore, this investigation was extended to consider the effects of branching.

Flow in Crack Networks

(a) Two-Dimensional Networks

242-Bond Network

Each network used in the first part of an investigation of two-dimensional networks contained 10 rows of 12 nodes in each row (see Fig. 5.3). The coordination number was 4 except for 20 nodes which had a coordination number of 3 because they were at the left or right-hand boundary. The choice of network size decreased the average coordination number from 4 (for an infinite network) to 3.833.

Apart from the boundary nodes, each central node was associated with four bonds (simulated cracks), but each bond was common to two neighboring nodes. Crack thicknesses were assigned as though each of 12 x 12 = 144 matrix elements had two bonds identified with it. Thus, 288 crack thicknesses were calculated to approximate closely a log-normal distribution. The resulting thicknesses were randomly assigned; 46 of these 288 values represented "bonds" that did not affect calculations. These "bonds" were associated with the inlet and outlet faces and left and right boundaries. (The inlet face was considered to be the first of the 12 rows, and the outlet face was considered to be the last row; however, pressures at points in the first and last rows were not allowed to change.) The effective discarding of 46 crack thickness values was a random process, since crack thicknesses were assigned randomly. For a given run of the overall simulated experiment, the population mean and population standard deviation of log (crack thickness) were varied, but the same set of random numbers was used. Therefore, during one complete run, the quantity

$$\frac{\text{Log (crack thickness)} - \text{Population Mean}}{\text{Population Standard Deviation}}$$

remained constant for a given bond, although absolute thicknesses changed with the changing values of the population mean and population standard deviation. (For example, the two sets of circles in Figs. 5.5 - 5.8 represent two complete runs.)

The conductance of a single bond is defined[5.2] such that

$$\text{Rate of fluid flow} = \text{Conductance} \times \text{Pressure difference} \qquad (5.6)$$

The conductance of each bond was calculated for both viscous and diffusive flow. Equations were essentially the same as used previously.[1.2]

When both viscous and diffusive flow are included, conductance of a given bond varies with pressure. For an iterative procedure to be strictly accurate, conductances would have to be recalculated as pressure values are refined. However, two approximations were used: one pressure value was used as the mean pressure for calculating all of the bond conductance values. Then once the bond conductances were calculated, they remained the same throughout a single network simulation at a given mean pressure P_m. To assure that these approximations would not cause a very large error, the inlet and outlet pressures were set at 1.005 P_m and 0.995 P_m, respectively.

For each mean pressure, the node pressures were determined by Gauss-Seidel iteration. Convergence was always obtained if the standard deviation of the population of log of crack thicknesses was 0.2 or smaller. Convergence occurred for some, but not all, of the simulations for which this standard deviation was 0.3. After the pressure at each node was found, flow into the network was determined by calculating (from Eq. 5.6) the flow through each of the 12 inlet bonds and summing. Flow out of the network was determined likewise. The arithmetic mean of these two flows (which were equal for all practical purposes if convergence had occurred) was used in calculating the permeability to gas at the given mean pressure. (Even when convergence did not occur, the inlet and outlet flow rate estimates from the final iteration were reasonably close to each other. The mean of these two estimates was used to calculate the permeability.)

200-Bond Network

The second part of this study differed from the first in that:

1. There were only 10 x 10 nodes besides the inlet and outlet faces (see Fig. 5.4). The coordination number of 80 of these nodes was 4. The other 20 nodes were on the left- or right-hand boundary and had a coordination number of 3. Therefore, the average coordination number of those 100 nodes was exactly 3.8.

2. Every one of the 200 bonds whose simulated crack thicknesses were specified actually was used in the network.

3. Equations were set up so that the rate of flow out of the network was one of the unknowns. Cramer's rule was used to solve for this one unknown in such a way that the factors resulting from reducing two 102 x 102 numerator determinants and one 102 x 102 denominator determinant to 2 x 2 determinants would generate like factors in the numerator and denominator down to the remaining 2 x 2 determinants. Those like factors were therefore discarded. This procedure lessened the possibility of underflow or overflow in the computer calculations. Computational details have been reported[1.1] for the 10 x 10 square grid model.

(b) Three-Dimensional Cubic Model:

A 285-Bond Network (Treated Numerically)

A three-dimensional cubic network model, which also had 100 nodes besides the inlet and outlet faces, was used in this phase of the study. These nodes were in a 5 x 5 x 4 pattern. Of these 100 nodes, only 36 were completely surrounded by other nodes or the inlet or outlet face and therefore had a coordination number of 6. Faces parallel to fluid flow contained 48 nodes that had a coordination number of 5. The remaining 16 nodes at edges had a coordination number of 4. The average coordination number of these 100 nodes was 5.2. Simulated permeabilities were determined by solving directly for rate of flow out of the network according to the method indicated above for part two of the two-dimensional phase of this study. Following calculation of the bond conductances, details of computing permeabilities were identical to those reported[1.1] for a 285-bond cubic network model. However, in the present model, bond conductances also included contributions from diffusive flow, rather than viscous flow alone.

(c) Distributions Used

Most of the distributions of crack thicknesses used in the computations were approximately log-normal. A relatively small amount of work was done (with a two-dimensional model) using sets of crack thicknesses whose values occurred in packets at certain discrete values. Such distributions will be referred to as "packet" distributions below. In all cases, the simulated crack thickness values were assigned randomly to the various positions.

(d) Crack Thickness from Viscous Flow

In another approach, an average crack thickness was estimated from purely viscous flow by assuming simple crack geometry and using an equation for flow in slits analogous to the Hagen-Poiseuille equation.

Assume that there are n crack segments connected in series parallel to the general direction of fluid flow. Each segment is of length L and width W cm. Thus, the entire channel is nL cm long. Assume that the cross-sectional area of interest (which can include both pore space and solid rock) is SW square cm. End effects and complications arising from gas entering an abruptly smaller or larger crack are neglected. H_i is used to designate the thickness of crack i. The H_i values are not necessarily all equal. However, it is assumed that the H_i values are so much smaller than W that the $2n\ H_iL$ contributions to the total surface area can be neglected when compared to the 2n WL contributions. Q is the flow rate for purely viscous flow (no gas slippage) in ml per second. In the following derivation, the overall pressure drop is represented simply by ΔP.

The fraction ϕ_c of the sample's volume that is crack porosity is the overall volume of crack porosity divided by the total volume. In this model, after the common factor WL is divided out of the numerator and denominator, this ratio can be expressed as

$$\text{Crack porosity} = \phi_c = \frac{\sum_{i=1}^{n} H_i}{nS} \tag{5.7}$$

Solving this equation for S gives

$$S = \frac{\sum_{i=1}^{n} H_i}{n\,\phi_c} \tag{5.8}$$

Equating

$$Q = \frac{K_\infty SW\Delta P}{\mu nL} \tag{5.9}$$

(which follows from the definition of permeability) to

$$Q = \frac{W(H_{est})^3 \Delta P}{12\,\mu\,n\,L} \tag{5.10}$$

(an equation which is obtained if the flow is considered to occur through one idealized crack shaped like a rectangular prism having length nL, width W, height H_{est}, and sufficiently high aspect ratio ($W >> H_{est}$) to neglect interaction with the narrow sides), where H_{est} is a kind of "average" crack thickness estimated from purely viscous flow, leads to

$$H_{est} = (12\,K_\infty S)^{1/3} \tag{5.11}$$

This result would also be obtained for a bundle of N_{ch} identical, parallel, non-interacting channels, since multiplying the right hand sides of both Eqs. 5.9 and 5.10 by N_{ch} would also lead to Eq. 5.11.

Substitution of Eq. 5.8 into Eq. 5.11 gives

$$H_{est} = \left(\frac{12\,K_\infty \sum_{i=1}^{n} H_i}{n\,\phi_c} \right)^{1/3} \tag{5.12}$$

Define S_v as the total surface area of cracks in square cm per cubic cm of volume. Using the assumption $W >> H_i$ enables one to neglect H_i in writing this approximate equation for S_v:

$$S_v = \frac{2\ W\ n\ L}{S\ W\ n\ L} = \frac{2}{S} \tag{5.13}$$

(The factor 2 in the numerator results from including both large surfaces of each crack in calculating S_v. Also, this treatment continues to be valid for the bundle of parallel, identical, non-interacting channels model, since the factor N_{ch} is common to both the numerator and denominator and divides out.)

Substituting Eq. 5.8 into Eq. 5.13 produces

$$S_v = \frac{2\ n\ \phi_c}{\sum_{i=1}^{n} H_i} \tag{5.14}$$

which can be rearranged to become

$$\frac{1}{n} \sum_{i=1}^{n} H_i = \frac{2\ \phi_c}{S_v} \tag{5.15}$$

According to Underwood,[5.3]

$$S_v = \left(\frac{4}{\pi}\right) L_A \tag{5.16}$$

where L_A is the total length of crack boundaries in cm per square cm of plane section area.

Substituting Eq. 5.16 into Eq. 5.15 gives

$$\frac{1}{n} \sum_{i=1}^{n} H_i' = \frac{\pi\ \phi_c}{2\ L_A} \tag{5.17}$$

Substituting Eq. 5.17 into Eq. 5.12 produces

$$H_{est} = \left(\frac{6\ \pi\ K_\infty}{L_A} \right)^{1/3} \tag{5.18}$$

If L_A' is the total crack length per unit area (cm per cm^2) obtained from plane section (or SEM) by counting only one side of each crack (as was done in the present work), then

$$H_{est} = \left(\frac{3\ \pi\ K_\infty}{L_A'} \right)^{1/3} \tag{5.19}$$

The crack thickness values obtained from this equation should be regarded as approximate, since the equation applies to an idealized system for which no tortuosity factor is included.

(e) Conclusions

For two-dimensional network models, internal nodes of which have a coordination number of four, both the method using Klinkenberg effects[1,2] and the method using purely viscous flow while disregarding tortuosity provided excellent estimates of the geometric means of log-normal distributions and the arithmetic mean of "packet" distributions when the variance was not large. (Packet distributions having very large variances were not studied.) For log-normal distributions having relatively large variances, the estimates were a little less accurate, but were still considered good.

Results for simulated Klinkenberg experiments for two-dimensional models having simulated crack thicknesses that follow log-normal distributions are shown in Figs. 5.5 and 5.6. Results for models having a simulated geometric mean crack thickness of 0.1 micron are shown in Fig. 5.5. It is seen that good estimates of the arithmetic and geometric means were obtained for both models when the standard deviation of the logarithm of simulated crack thickness was small. When this standard deviation was increased somewhat, good estimates continued to be obtained for the geometric mean, but not for the arithmetic mean. Even when this standard deviation was increased to 0.5, estimates of the geometric mean were reasonably good. As shown in Fig. 5.6, similar results were obtained for models having a simulated geometric mean crack thickness of 1 micron, although simulated experiments did not succeed as well in estimating the geometric mean when the standard deviation of the logarithm of simulated crack thickness was relatively large. For all of these two-dimensional networks studied, simulated estimates of crack thicknesses were considerably smaller than the arithmetic mean when the standard deviation of the logarithm of simulated crack thickness was relatively large.

Simulated estimates of crack thickness from purely viscous flow according to Eq. 5.19 are plotted for the same networks in Figs. 5.7 and 5.8. Comparison of Figs. 5.5 and 5.7 reveals very similar behavior for a geometric mean crack thickness of 0.1 micron. In Fig. 5.8, it is seen that simulated estimation of crack thickness from purely viscous flow remained good even for models having relatively large standard deviations of log (crack thickness) when the geometric mean crack thickness was 1 micron.

Results for the 285-bond three-dimensional network model are plotted in Fig. 5.9. It is seen that the method using Klinkenberg effects[1,2] again gave excellent estimates of geometric and arithmetic means of log-normal distributions when the standard deviation of log (crack thickness) was small. With larger values of the standard deviation of log (crack thickness), this method consistently gave values larger than the geometric mean. However, these values were reasonably good estimates of

the arithmetic mean for log-normal distributions having up to about 0.4 for the standard deviation of log (crack thickness). The method using purely viscous flow while ignoring tortuosity gave rather poor results, indicating that tortuosity should be considered for that method with this geometry. The method using Klinkenberg effects[1.2] does not require a tortuosity factor; this is one of the advantages of that method.

When the algebraic results for a coordination number two model are considered with numerical results for models having coordination numbers of four and six, it is seen that the influence of narrow cracks decreases with increasing coordination number and dimensionality. This effect is expected, since having a larger coordination number and dimensionality provides more opportunities for avoiding the most narrow cracks via channeling.

Crack Thicknesses from Experimental Data

The Klinkenberg slope together with the Klinkenberg permeability can be used to estimate an average crack thickness.[1.2] Values so obtained for Suite 2 (high carbonate) samples are given in Table 5.1 and plotted in Fig. 5.10. Results for first and second loading of the cores at 500 and 5000 psi overburden pressure are included in this plot. The points are, not surprisingly, somewhat scattered. A slope of 2.14 was found for the linear regression line of the log of the Klinkenberg permeability vs. the log of the crack thickness (dashed line in Fig. 5.10). When only those samples giving very close to straight line Klinkenberg plots (that is, Klinkenberg data having a square of estimate of correlation between K_p and $1/P_m$ of at least 0.99) were used, a slope of 2.33 was found for the least squares line (solid line in Fig. 5.10). This is somewhat closer to the value of 3 that would be expected for an idealized system of high aspect ratio cracks.

Since estimates of crack length per unit area of plane section were obtained from scanning electron micrographs of pore casts for most of the Suite 1 (assorted cores) samples,[1.1] crack thicknesses could also be estimated from purely viscous flow according to the derivation for an idealized system provided in this section. The crack thickness values obtained from purely viscous flow should be regarded as very approximate, since the calculation method applies to a highly idealized system; for example, no tortuosity factor is included. Results are presented in Table 5.2. Also listed in the same table are crack thicknesses estimated by a previously reported method[1.2] using Klinkenberg slope and Klinkenberg permeability.

Whenever comparison could be made of the crack thicknesses calculated by the two methods, the crack thickness estimated from viscous flow was always larger than that calculated from the Klinkenberg permeability and slope. This difference could be due to underestimation of total crack length.

Correlations between Klinkenberg Permeabilities and B Factors

Five low-permeability samples were studied extensively.[5.4] From resulting data, the relationship between the logarithm of Klinkenberg slip factor (B, which is inversely proportional to an average crack thickness), and the logarithm of Klinkenberg permeability (K_∞) was investigated and compared with previously published correlations. The results were close to, but different from, that of Jones and Owens[1.5]

$$B = 0.86\ K_\infty^{-0.33} \tag{5.20}$$

and that of Heid, et al.[1.6]

$$B = 0.777\ K_\infty^{-0.39} \tag{5.21}$$

The Jones and Owens correlation[1.5] came from a study of tight gas sands core samples, most of which had Klinkenberg permeabilities less than 0.1 md. In that study, measurements were made at net confining pressures equalling estimated values of reservoir net overburden. During Klinkenberg permeability determinations (which usually were made by extrapolating permeabilities measured at 100 psig and 1000 psig upstream pressure and atmospheric pressure downstream), confining pressure was increased sufficiently to offset average increase in pore pressure to keep net confining pressure essentially constant.

The relationship of Heid et al.[1.6] involved a large selection of core samples, most of which had Klinkenberg permeabilities greater than 1 md. In that study, core samples had been mounted in Lucite under a pressure of 200 psi during heating and 1000 psi during cooling, and Klinkenberg permeabilities had been determined at mean gas pressures ranging from slightly greater than one atmosphere to approximately four atmospheres.

The confining pressure and temperature were varied in an extensive study[5.4] connected with the present work. From resulting data, effects of these variables on the relationship between the Klinkenberg B factor and the Klinkenberg permeability were investigated. Klinkenberg permeabilities and slopes determined for Old Man Mountain #2 (4498 ft), 10570 S BETC (10570 ft), CIGE 21 (4403.3 ft), U78JP36 (8262.3 ft), and (MWX-2) 48-9 bottom (5731 ft) core samples at several temperatures and several levels of confining pressure gave:

$$B = 0.644\ (10^{1.52 \times 10^{-5} P + 0.0018 T})\ K_\infty^{-0.28} \tag{5.22}$$

B is the Klinkenberg B factor in atmospheres, P is the confining pressure in psi, T is the temperature in degrees Celsius, and K_∞ is the Klinkenberg permeability in millidarcies. Experimental values of the Klinkenberg B factor are plotted against values predicted by Eq. 5.22 in Fig. 5.11.

Subsets of this data set were used such that, for each subset, the temperature and confining pressure were constant. Linear regression was performed on each of these subsets of log B vs. log K_∞ data. The values of C and n so obtained for

$$B = C\,K_\infty^{\,n} \tag{5.23}$$

are listed in Table 5.3. The relationship between C and confining pressure and temperature is also shown in Fig. 5.12.

Data from the same overall data set also were divided into subsets in a different manner. Each of these subsets contained data for only one sample at one temperature and six confining pressures. Thus, linear regression on each of these subsets reflected the change in B with K_∞ when the changing K_∞ was associated with changing confining pressure. The exponent n obtained by this procedure showed more variation, and the absolute values of n were generally larger than those obtained by considering different samples subjected to the same confining pressure and temperature. Results are shown in Table 5.4.

Subsets of data obtained in the present work for Suite 2 (first and second loading) and Suite 3 (first loading) samples giving Klinkenberg plots that were reasonably close to straight lines (i.e., square of estimate of correlation between $1/P_m$ and K_p is at least 0.9) led to the relationships given by Eq. 5.24 - 5.26. When data sets from both of these suites were treated together,

$$B = 0.432\,K_\infty^{-0.36} \tag{5.24}$$

As is typical for this type of correlation, our data exhibited considerable scatter. Data from many of the samples from Suites 2 and 3 were used in determining this equation. When data sets from Suites 2 and 3 were each treated separately, high carbonate samples (Suite 2) gave

$$B = 0.537\,K_\infty^{-0.32} \tag{5.25}$$

and Multi-Well samples (Suite 3) gave

$$B = 0.288\,K_\infty^{-0.43} \tag{5.26}$$

A set of data for a single sample [(MWX-1) 14-14] subjected to six levels of overburden pressure gave very close to straight line Klinkenberg plots (the square of estimate of correlation between $1/P_m$ and K_p ranged from 0.994 to 0.9998). Results for this single sample gave

$$B = 13.3\,K_\infty^{-0.406} \tag{5.27}$$

Effect of Solution Porosity on Permeability in Simple Models

In order to help estimate the effect of solution (vugular) porosity on permeability of a network of sheet pores, a simple cubic model[1,2] was considered, and simple rectangular networks were simulated. In the simple cubic model, it was assumed that sheet pores between individual cubes (grains in the model) were so much thinner than the cubes that resistance to flow through solution pores could be neglected when compared to resistance to flow through sheet pores. It was assumed that the model was

sufficiently large that small sample effects could be neglected. It was also assumed that flow occurred in only one direction, which was perpendicular to two faces of any given cube. (This simplifying assumption of not allowing flow from one channel to another is similar to flow restriction in a bundle of capillaries model.) Geometric considerations have shown that the effect of removing a small number of isolated cubes from this cubic model having zero solution porosity is described by

$$\frac{d\left(\frac{K - K_c}{K_c}\right)}{d\,\phi_1} \approx 2 \tag{5.28}$$

where K_c is the permeability in the absence of any solution pores (i.e., the permeability due to sheet pores) and

$$\phi_1 = \frac{\text{Solution porosity (fraction)}}{\text{Solution porosity (fraction)} + \text{Volume fraction occupied by grains}} \tag{5.29}$$

or

$$\phi_1 = \frac{\text{Volume occupied by solution porosity}}{\text{Total volume (excluding cracks)}} \tag{5.30}$$

Thus ϕ_1 is the fraction of cubes removed in this model. Notice that this relation applies in the limit of zero solution porosity.

This relationship can be visualized by using a model whose cubes all have edges one unit long and by considering the effect of removal of one cube. Let the model be x cubes wide and y cubes high perpendicular to the direction of fluid flow and z cubes long in the direction of flow, where x, y, and z are so large that boundary effects can be neglected. Let h be the crack thickness. Removal of one cube decreases the total volume of sheet pores parallel to the direction of fluid flow by 4h out of the original volume of 2hxyz. Removal of that cube also decreases the total solid volume xyz by one unit. Comparing $4h/2hxyz = 2/xyz$ with $1/xyz$ indicates that the fractional increase of permeability is twice as great as the fractional increase of vugular porosity at the limit of zero vugular porosity.

In rectangular network simulations, one or two simulated grains were replaced with solution (vugular) pores in each network. Results from these simulations indicate that this simple treatment underestimates the effect of an isolated solution pore on permeability. Flow being diverted from neighboring channels into the channel containing the pore increases the effect the lone pore has on permeability. For 2-dimensional square networks, the additional flow resulting from creating one solution pore in the center of the network is 1.5755 times (for a 22 x 24 network calculated with double precision) or 1.565 times (for a 38 x 40 network

calculated with single precision) that predicted by a limiting case of the simple cube model which is only one cube thick in the y direction.

REFERENCES

5.1 Allen, T., Particle Size Measurement, third edition, Chapman and Hall, London and New York (1981).

5.2 Koplik, J., "Creeping Flow in Two-Dimensional Networks," J. Fluid Mech., 119 (1982) 219-247.

5.3 Underwood, E. E., "Quantitative Stereology," Addison-Wesley Publishing Co. (Reading, MA; Menlo Park, CA; London; Don Mills, Ontario, 1970). Eq. 2.2 on p. 24.

5.4 Wei, K. K., "Effect of Confining Pressure and Temperature on Low Permeability Sandstones," M.S. thesis, New Mexico Institute of Mining and Technology, Sept. 1983.

Table 5.1 The Effect of Overburden on Permeability and Crack Thickness of Suite 2 Samples (High in Carbonate Cement)

Group ID	Origin ID	Depth (feet)	Loading	Overburden pressure: 500 psi K_∞ (md)	500 psi Crack thickness (microns)	5000 psi K_∞ (md)	5000 psi Crack thickness (microns)	$K_{\infty,500} / K_{\infty,5000}$
13	RBE-01	5863.6	1	0.0232	0.20	0.00054	0.14	43.2
13	RBE-01	5863.6	2	0.0116	0.28	0.00056	0.17	20.5
14	RBE-01	5898.5	1	0.0129	0.34	0.00016	0.03	80.0
14	RBE-01	5898.5	2	0.0027	0.16	0.00016	0.03	16.7
17	PTS 22-12	6403.0	1	0.0635		0.0013	0.07	49.3
17	PTS 22-12	6403.0	2	0.0302	0.35	0.0014	0.09	21.6
18	PTS 22-12	6431.0	1	0.0137	0.32	0.00036	0.05	38.2
18	PTS 22-12	6431.0	2	0.0075	0.22	0.00037	0.05	20.3
19	PTS 22-12	6509.6	1	0.0103		0.00010	0.09	105.3
19	PTS 22-12	6509.6	2	0.00037	0.11	0.00010	0.10	3.7
20	Mobil 45-14G	5140.	1	0.0451	0.33	0.0028	0.09	16.1
20	Mobil 45-14G	5140.	2	0.0237	0.34	0.0029	0.09	8.1
21	Mobil 26-7G	3309.	1	0.0873	0.50	0.0084		10.4
21	Mobil 26-7G	3309.	2	0.0405	0.11	0.0081		5.0
22	Mobil 26-7G	2924.	1	0.0108		0.00022	0.06	49.7
22	Mobil 26-7G	2924.	2	0.0018	0.09	0.00024	0.07	7.7
23	OMM #2 Colo	5457.	1	0.0299	0.23	0.0022	0.10	13.4
23	OMM #2 Colo	5457.	2	0.0143		0.0021	0.09	6.9
24	OMM #2 Colo	5469.4	1	0.0037	0.36	0.00010	0.08	36.2
24	OMM #2 Colo	5469.4	2	0.00039	0.05	0.00010	0.08	3.8
25	Arco-Exxon L-36	3701.	1	0.0121		0.00034	0.05	35.3
25	Arco-Exxon L-36	3701.	2	0.0018	0.10	0.00033	0.05	5.5
26	3014-15		1	0.0190	0.20	0.0019	0.09	10.0
26	3014-15		2	0.0094	0.12	0.0019	0.10	4.9

OMM = Old Man Mountain

Table 5.2 Crack Thicknesses Estimated for Suite 1 Samples (Assorted Cores)

Origin ID and cut direction		Depth (feet)	Crack thickness in microns estimated from:		Pressure sensitivity index
			purely viscous flow	Klinkenberg intercept and slope	
10570 S BETC	V	10570.0	0.242	-----	0.464
Old Man Mtn. #2	H	4498.0	2.022	0.430	0.094
Old Man Mtn. #2	V	4498.0	2.398	-----	0.066
Ralston Core	H	3713.0	1.299	0.120	0.184
Ralston Core	V	3713.0	1.365	-----	0.112
BC-1-25	H	7277.0	0.315	0.215	0.649
PCUF31-13G	H	8493.0	0.246	0.161	0.586
CIGE 21	H	4403.3	1.336	0.284	0.117
CIGE 21	V	4403.3	1.683	-----	0.119
CIGE 21	H	8492.0	0.391	0.212	0.308
CIGE 21	H	6503.0	0.726	0.568	0.530
Wilkin Ridge	H	10298.7	0.380	0.268	0.795
Wilkin Ridge	V	10298.7	0.431	-----	0.945

Table 5.3 C and n Values Determined for Old Man Mountain #2, 10570 S BETC, CIGE 21, U78JP36, and (MWX-2) 48-9 core samples at the Indicated Temperatures and Confining Pressures.

These can be used to predict the Klinkenberg B factor according to

$$B = C K_{\infty}^{n}.$$

Temperature (deg C)	Confining pressure (psi)	C	n
0	500	0.663	-0.28
0	1000	0.685	-0.28
0	2000	0.693	-0.28
0	3000	0.707	-0.27
0	4000	0.742	-0.28
0	5000	0.775	-0.30
24	500	0.726	-0.28
24	1000	0.749	-0.28
24	2000	0.769	-0.28
24	3000	0.782	-0.27
24	4000	0.806	-0.28
24	5000	0.820	-0.28
38	500	0.763	-0.28
38	1000	0.798	-0.28
38	2000	0.811	-0.28
38	3000	0.824	-0.27
38	4000	0.852	-0.28
38	5000	0.884	-0.28
63	500	0.848	-0.28
63	1000	0.874	-0.28
63	2000	0.893	-0.28
63	3000	0.918	-0.27
63	4000	0.943	-0.28
63	5000	0.998	-0.30

Table 5.4 C and n Values Obtained for a Single Sample at a Single Temperature but Varying Confining Pressures

Origin ID	Depth (feet)	Temperature (deg C)	C	n
Old Man Mountain #2	4498	0	0.963	-0.51
Old Man Mountain #2	4498	24	1.074	-0.53
Old Man Mountain #2	4498	38	1.145	-0.53
Old Man Mountain #2	4498	63	1.247	-0.53
Old Man Mountain #2	4498	90	1.368	-0.53
10570 S BETC	10570	0	0.496	-0.36
10570 S BETC	10570	24	0.609	-0.35
10570 S BETC	10570	38	0.690	-0.34
10570 S BETC	10570	63	0.730	-0.34
CIGE 21	4403.3	0	0.781	-0.28
CIGE 21	4403.3	24	0.860	-0.31
CIGE 21	4403.3	38	0.905	-0.31
CIGE 21	4403.3	63	1.003	-0.30
CIGE 21	4403.3	90	1.106	-0.27
U78JP36	8262.3	0	0.197	-0.50
U78JP36	8262.3	24	0.490	-0.31
U78JP36	8262.3	38	0.384	-0.37
U78JP36	8262.3	63	0.244	-0.50
(MWX-2) 48-9, bottom	5731	0	0.357	-0.39
(MWX-2) 48-9, bottom	5731	24	0.401	-0.38
(MWX-2) 48-9, bottom	5731	38	0.428	-0.38
(MWX-2) 48-9, bottom	5731	63	0.497	-0.37

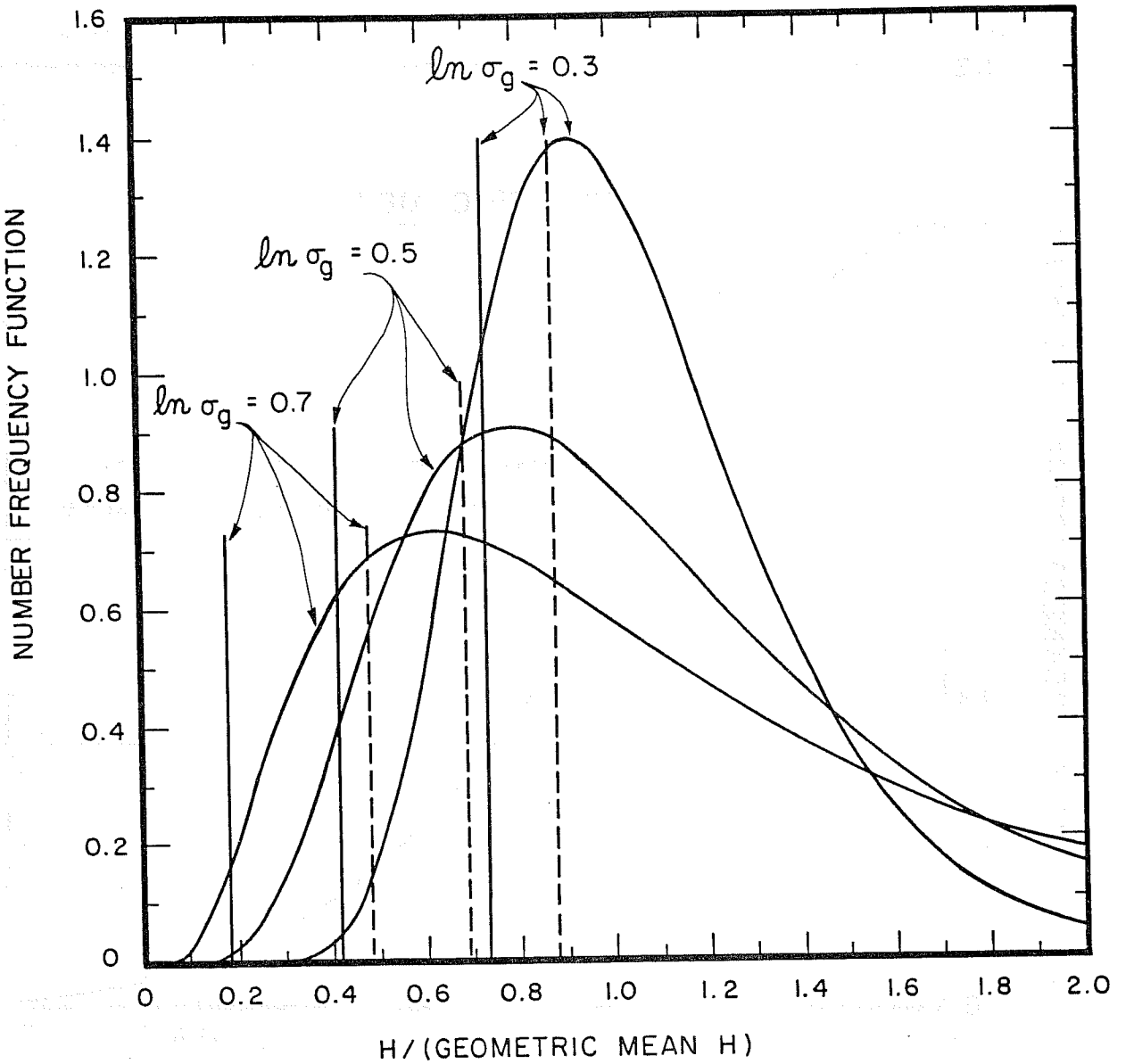

Fig. 5.1 Log-normal number distributions of simulated crack thickness and corresponding estimated crack thicknesses* calculated from algebraic expressions derived for the no-branching model. Crack size distributions are plotted for the indicated values of the standard deviation of the natural logarithm of crack thickness ($\ell n\ \sigma_g$).

*Solid vertical lines indicate results expected if both the Klinkenberg slope and intercept data are used. Dashed vertical lines indicate results expected if data for purely viscous flow are used.

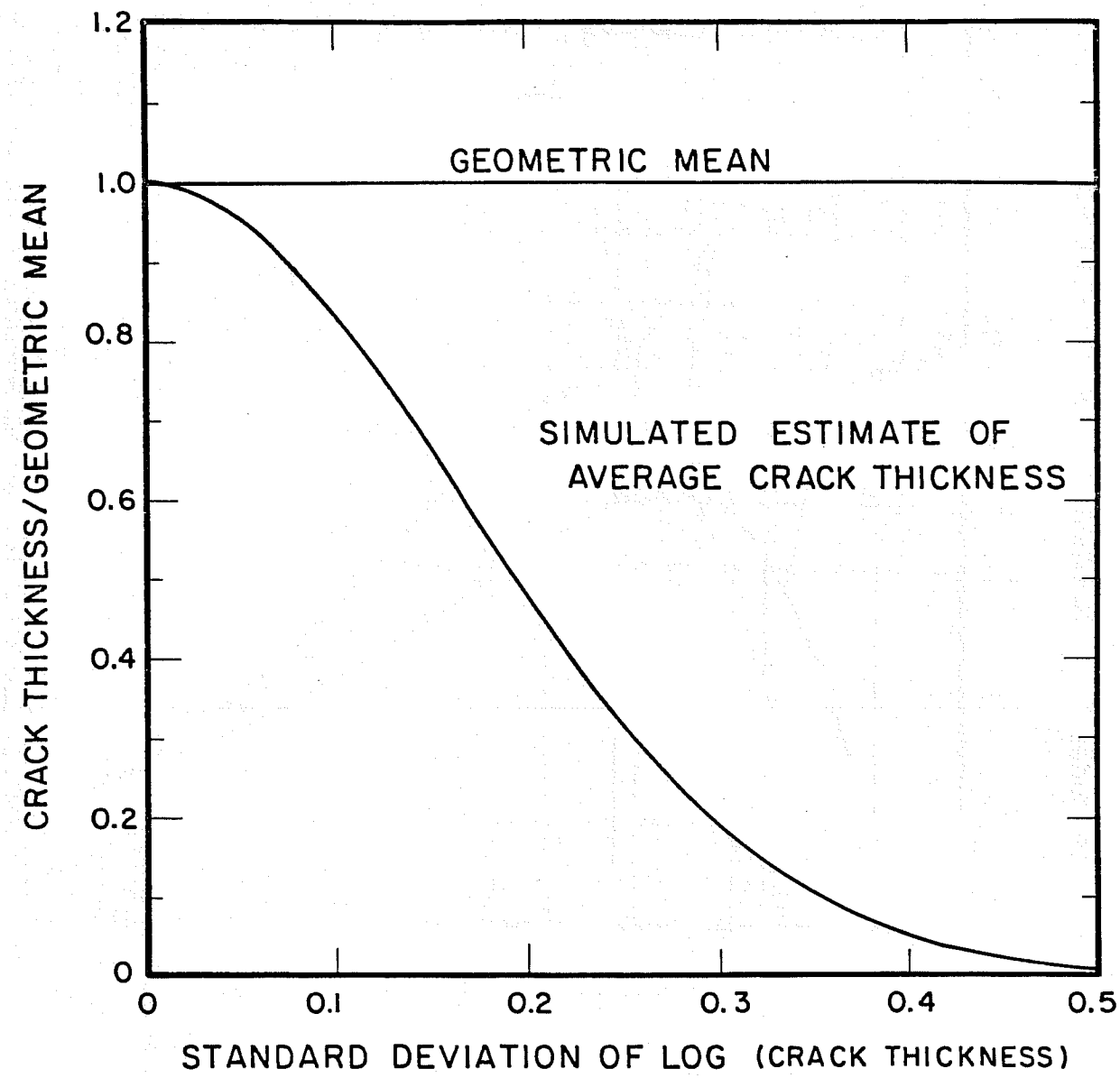

Fig. 5.2 Comparison of simulated estimate (curved line) of crack thickness from gas slippage with the actual geometric mean (straight line) for model of cracks connected in series (no branching). In this model, thicknesses of cracks follow a log-normal distribution. It is seen that narrow cracks exert a disproportionately large influence on the simulated estimate of crack thickness.

Inlet Face: Pressure is equal at all inlet face nodes.
Outlet Face: Pressure is equal at all outlet face nodes.
Node: Has negligible resistance to flow.
Bonds: Represent sheet pores and account for all of the resistance to flow.

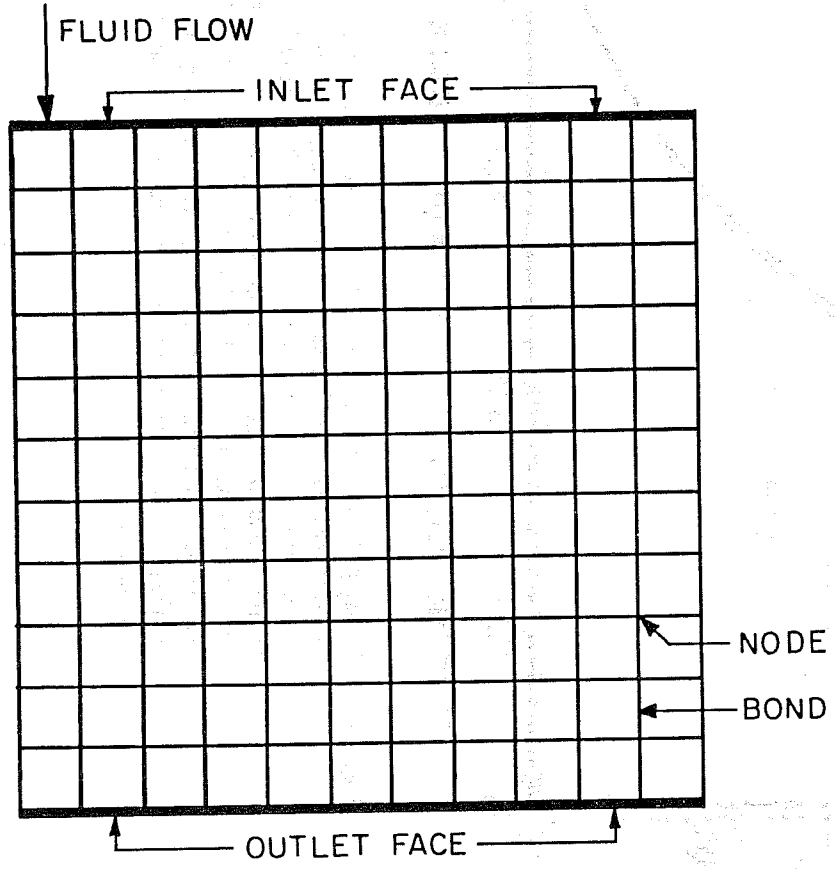

Fig. 5.3 Representation of 242-bond rectangular network.

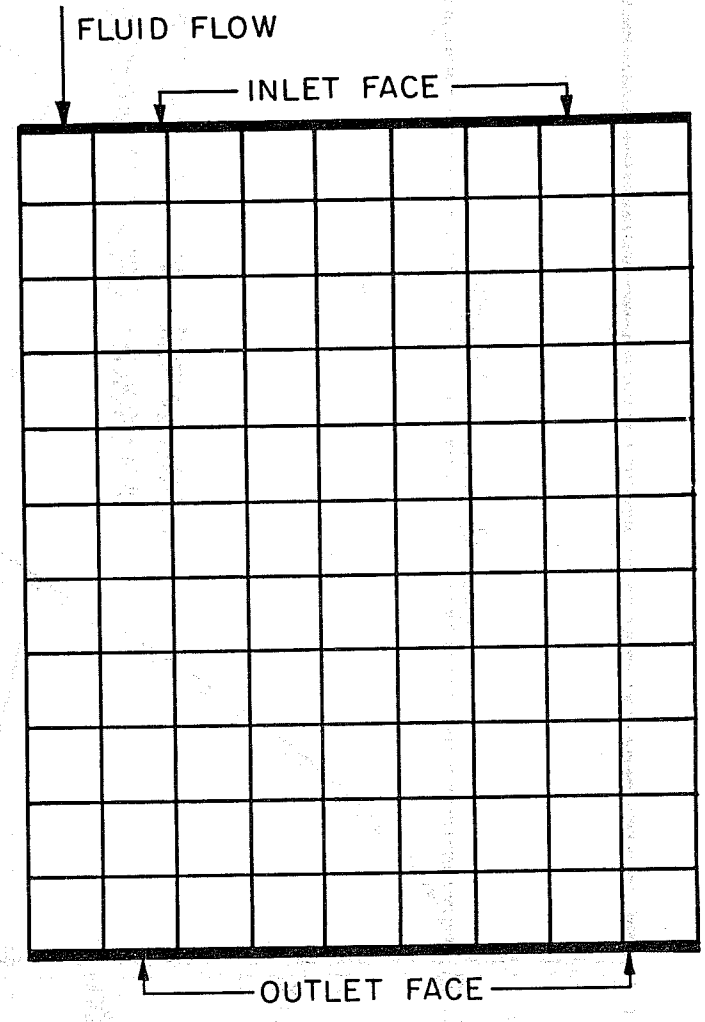

Fig. 5.4 Representation of 200-bond rectangular network.

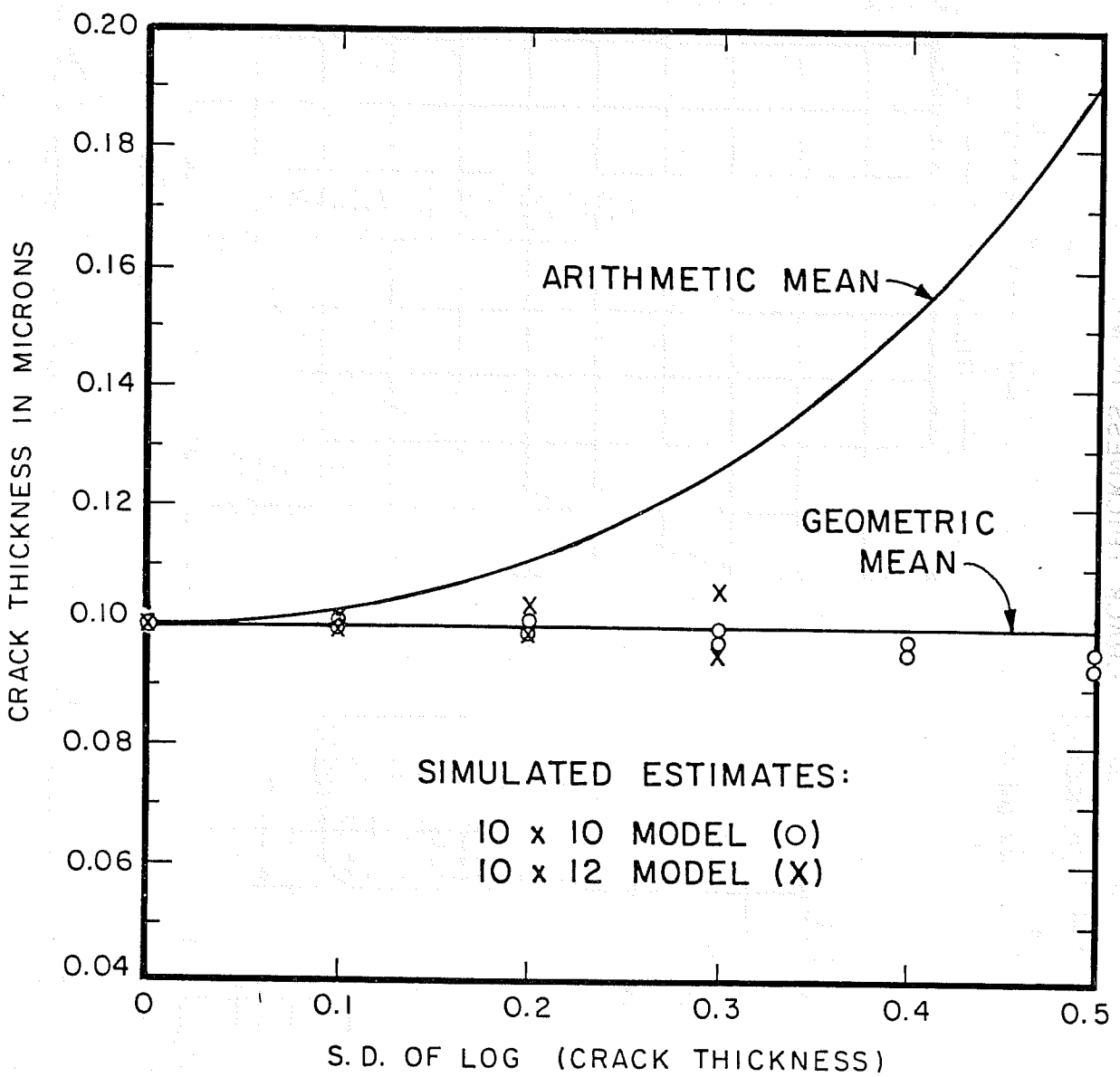

Fig. 5.5 Comparison of simulated estimates (points) of crack thickness from gas slippage with the actual geometric and arithmetic means (solid lines) for two-dimensional network models. For both models, the simulated measurements provide good estimates of the geometric mean. However, the arithmetic mean is estimated well only when the standard deviation of the logarithm of crack thickness is small.

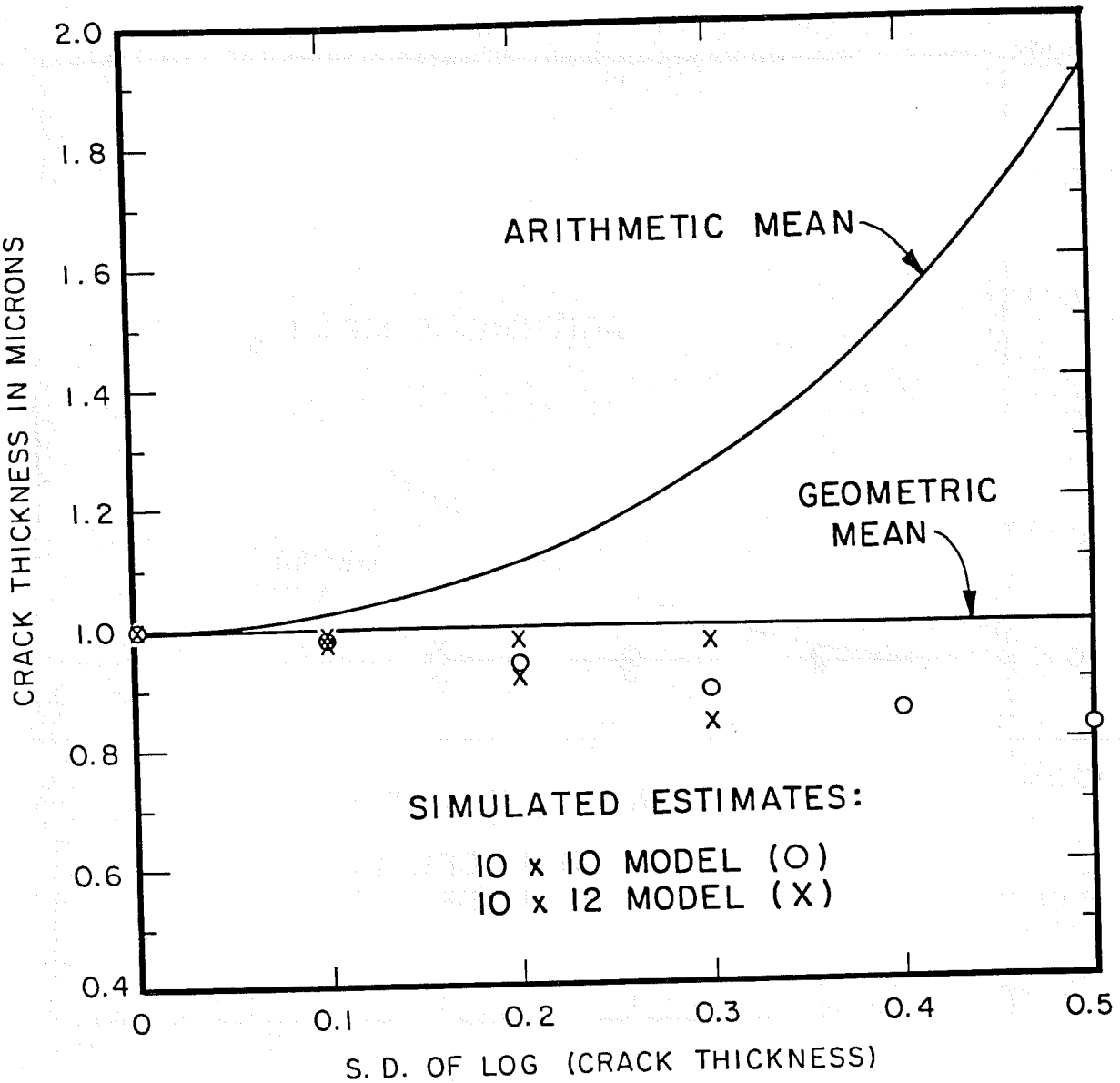

Fig. 5.6 Comparison of simulated estimates (points) of crack thickness from gas slippage with the actual geometric and arithmetic means (solid lines) for two-dimensional network models. For both models, the simulated measurements provide good estimates of means when the standard deviation of the logarithm of crack thickness is small. With larger values of the standard deviation, fair estimates of the geometric mean, but not the arithmetic mean, are obtained.

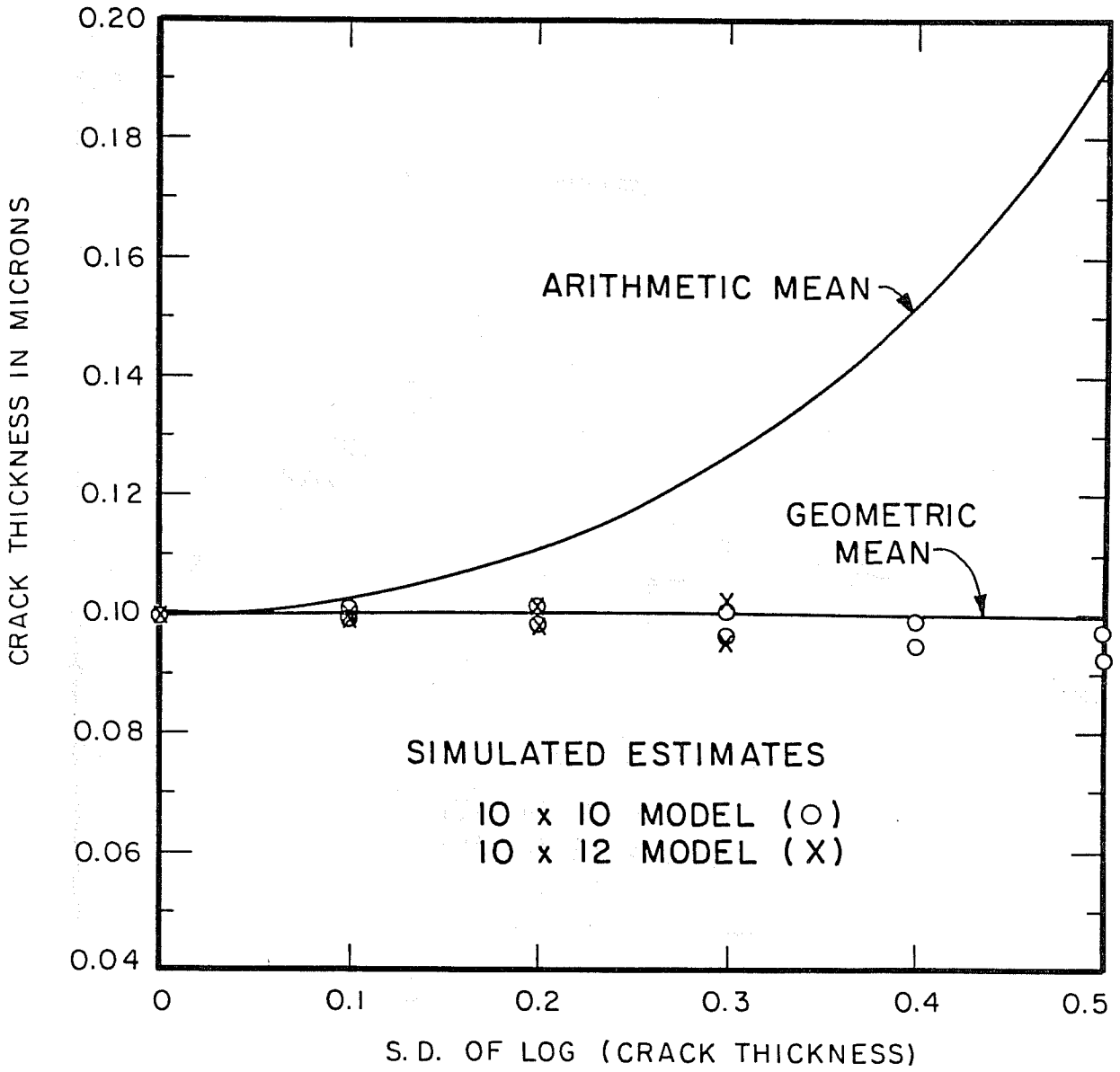

Fig. 5.7 Comparison of simulated estimates (points) of crack thickness from purely viscous flow with the actual geometric and arithmetic means (solid lines) for two-dimensional network models. For both models, the simulated measurements provide good estimates of the geometric mean. However, the arithmetic mean is estimated well only when the standard deviation of the logarithm of crack thickness is small.

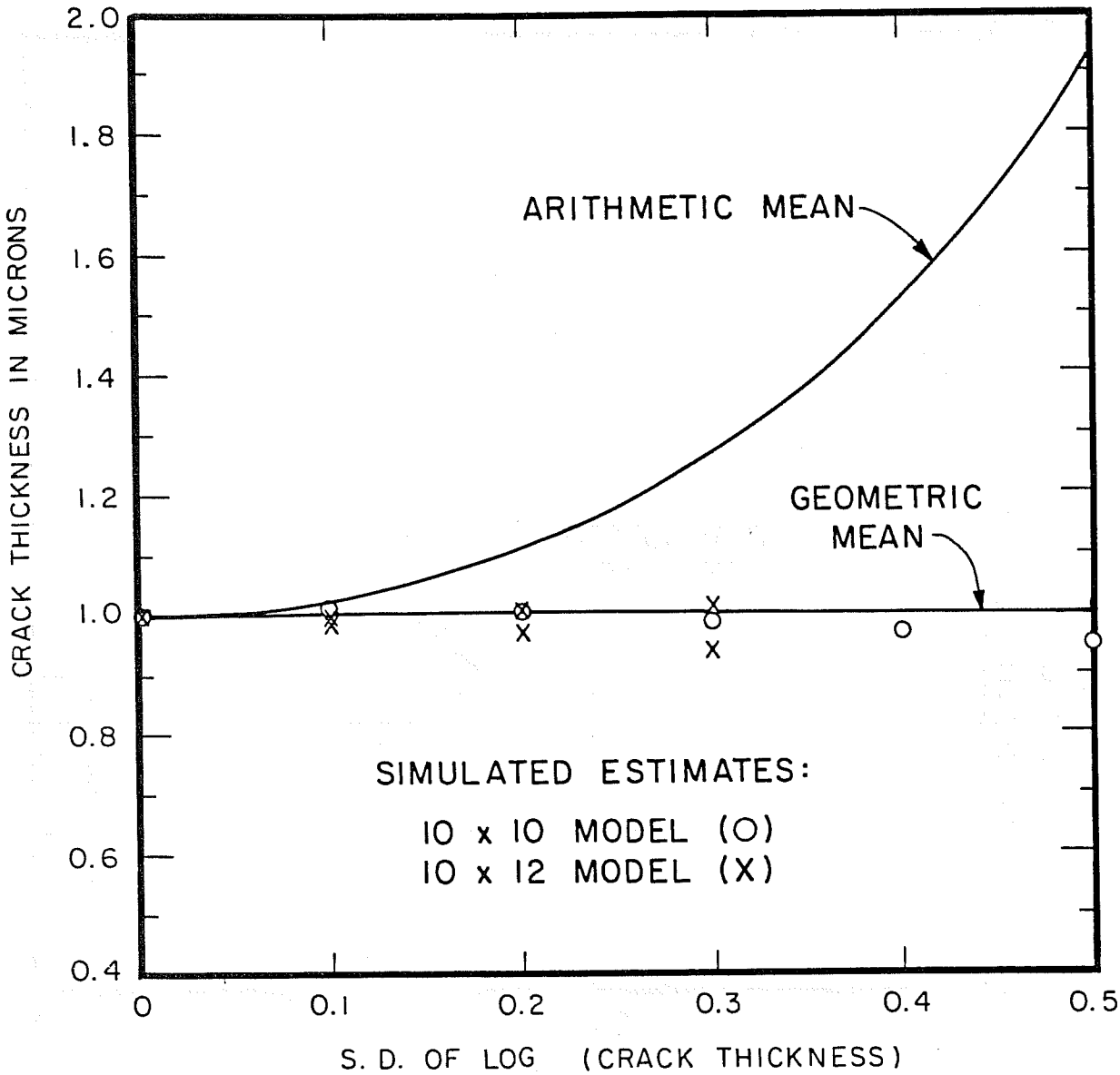

Fig. 5.8 Comparison of simulated estimates (points) of crack thickness from purely viscous flow with the actual geometric and arithmetic means (solid lines) for two-dimensional network models. For both models, the simulated measurements provide good estimates of the geometric mean. However, the arithmetic mean is estimated well only when the standard deviation of the logarithm of crack thickness is small.

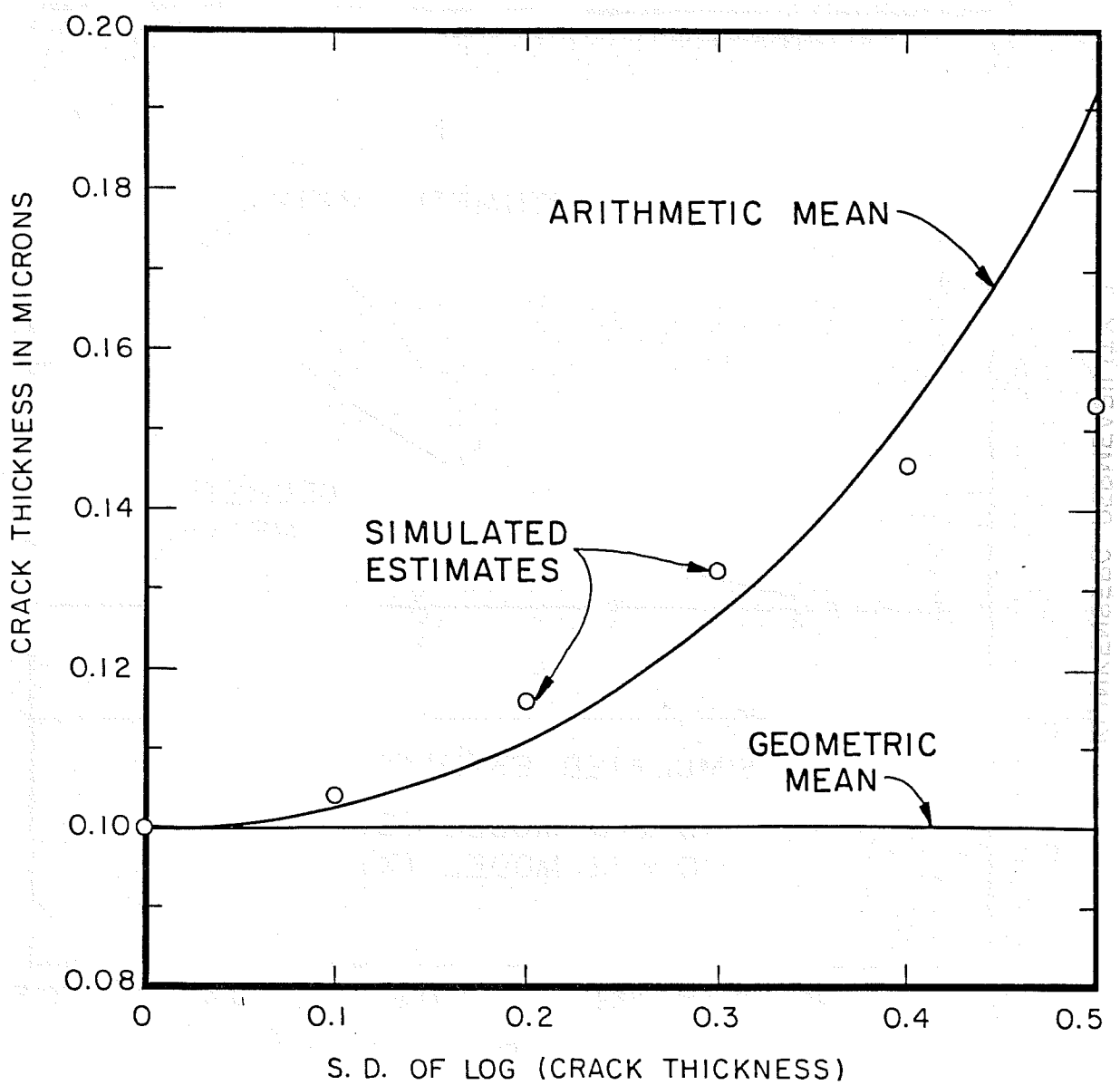

Fig. 5.9 Comparison of simulated estimates (points) of crack thickness from gas slippage with the actual means (solid lines) for the 285-bond three-dimensional network model. The simulated measurements provide good estimates of means when the standard deviation of the logarithm of crack thickness is small. When this standard deviation is between about 0.1 and 0.4, reasonably good estimates of the arithmetic mean, but not the geometric mean, are obtained.

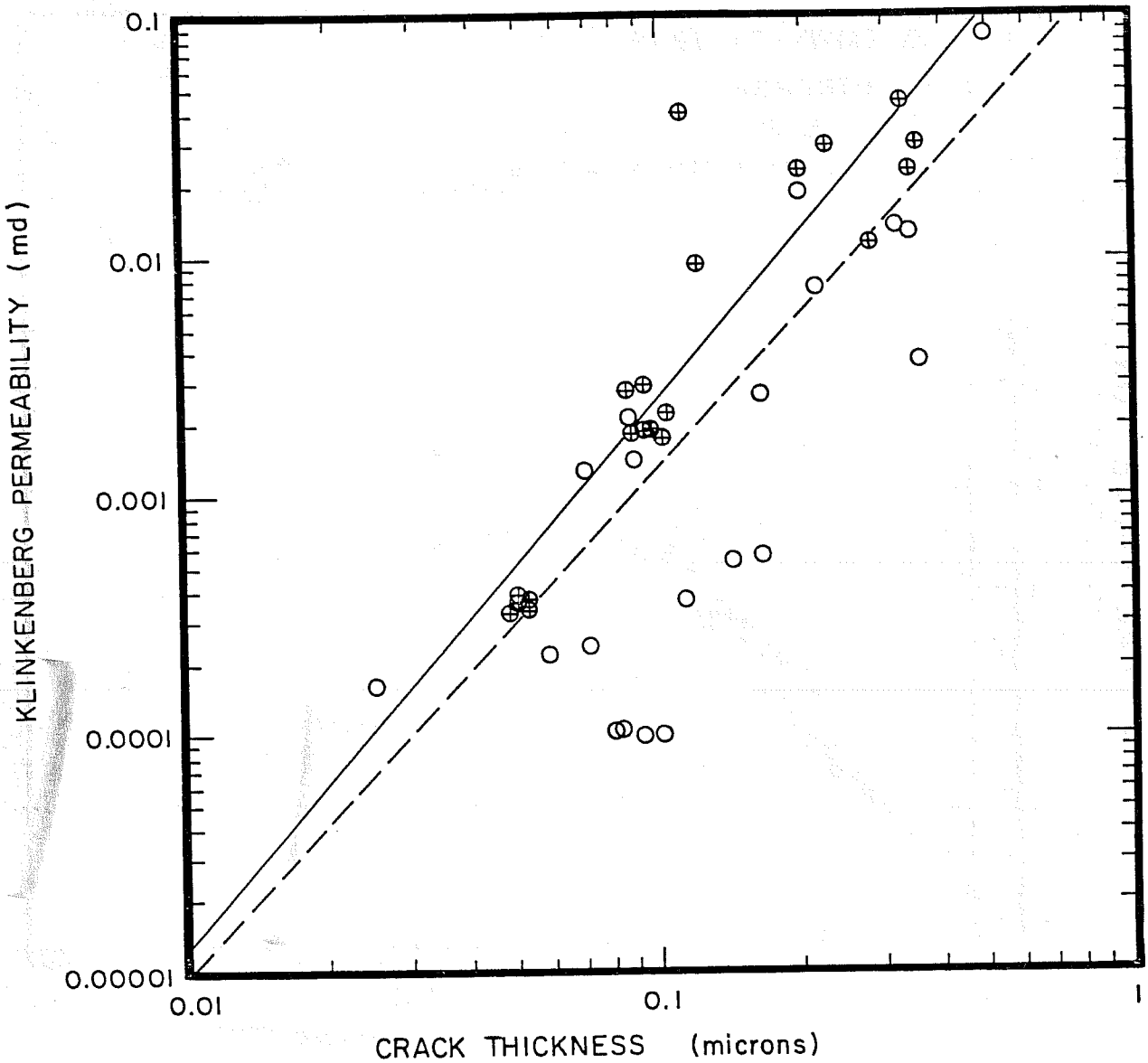

Fig. 5.10 Suite 2 samples (with high carbonate cement)

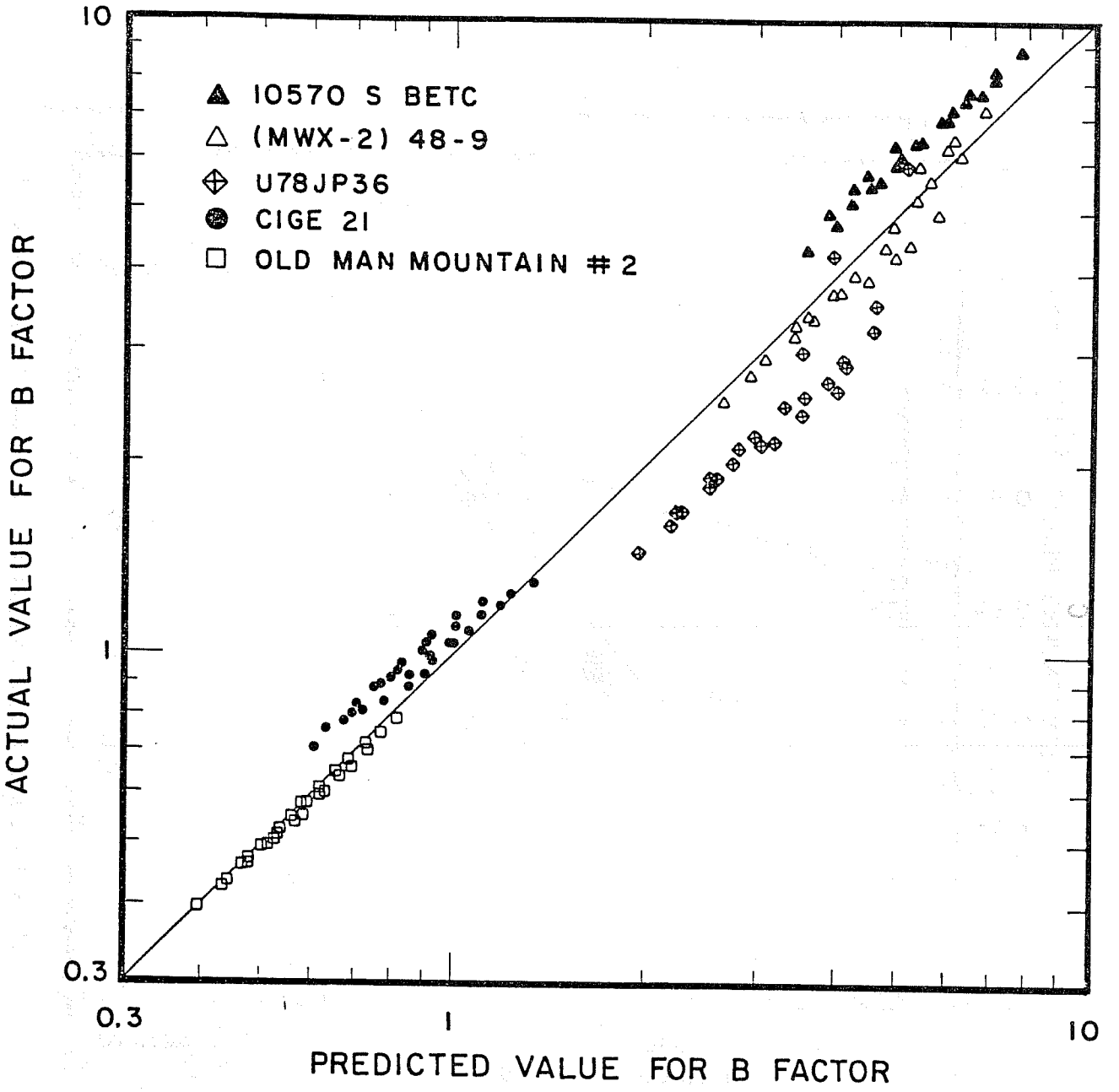

Fig. 5.11 Points represent actual values of Klinkenberg B factor vs. values predicted by Eq. 5.22 for five core samples at various temperatures and confining pressures. The solid line shows where points would lie if Eq. 5.22 predicted the B factor values perfectly.

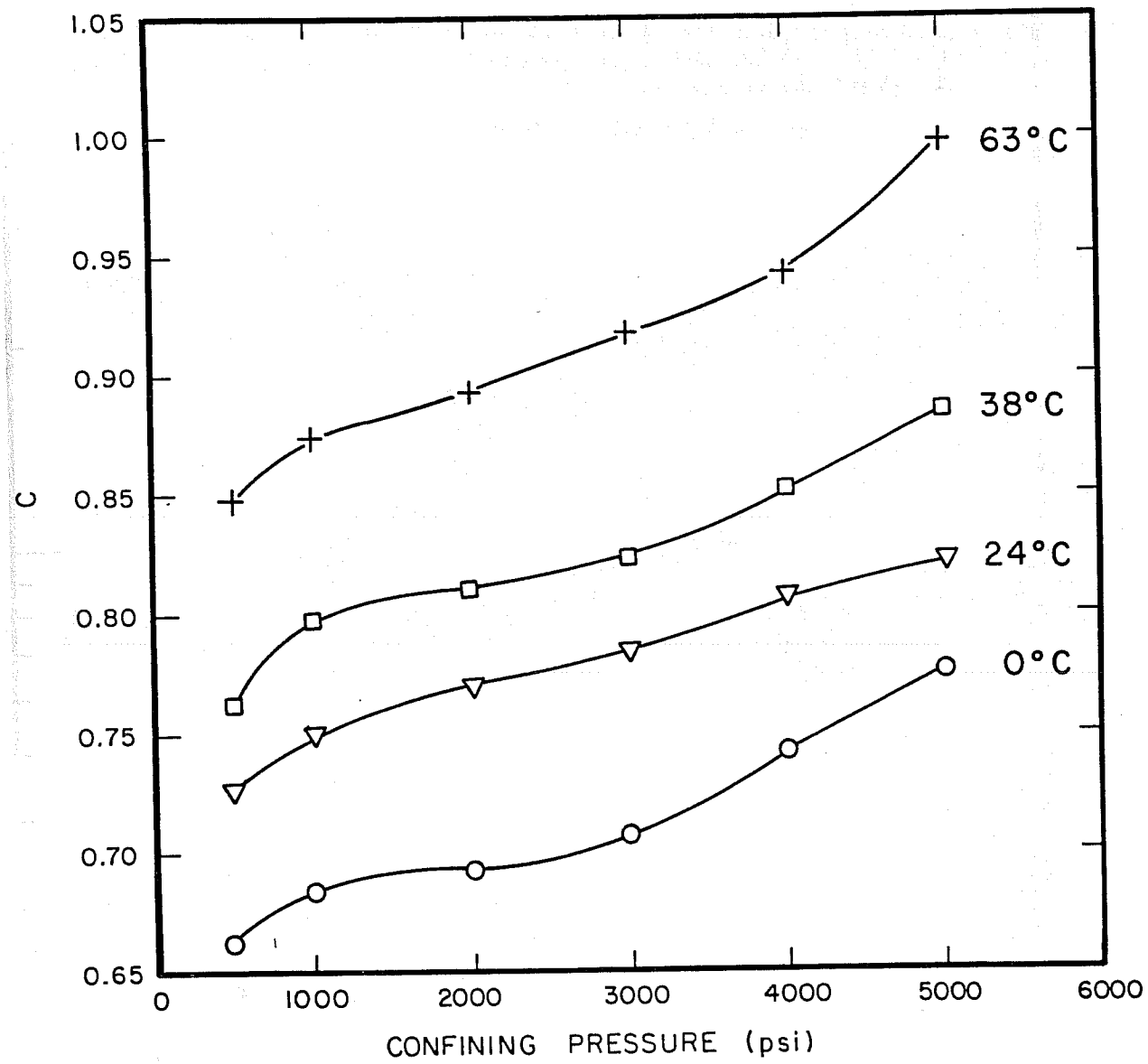

Fig. 5.12 The relationship between C (in Eq. 5.23, which is a correlation involving the Klinkenberg B factor) and temperature and confining pressure. At a given temperature, C increases with increasing confining pressure. At a given confining pressure, C increases with increasing temperature.

APPENDIX 1. PERMEABILITY VS. CONFINING PRESSURE RELATIONSHIPS

This appendix provides the data bank of permeability vs. confining pressure relationships from which the measures of pressure sensitivity presented in Section 1 were derived. (see Figs. A1.1-A1.47)

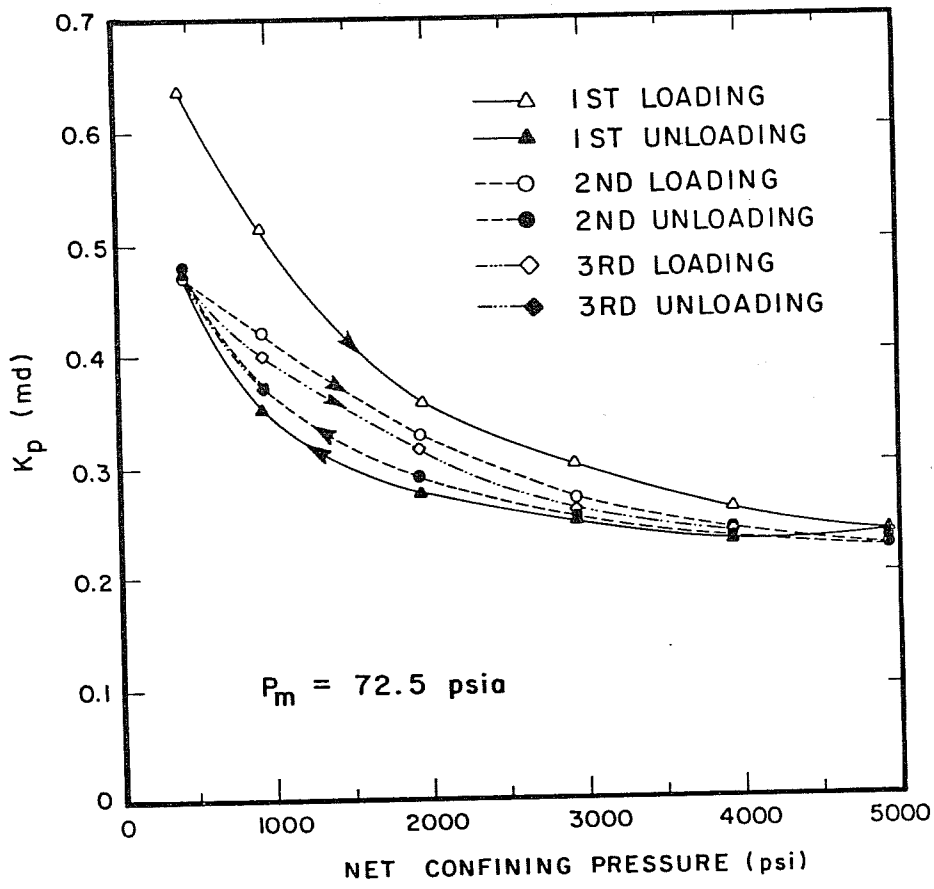

Fig. A1.1 Permeability vs. net confining pressure for 6405 core sample (Group ID 1; depth 6405.0 ft; horizontal cut)

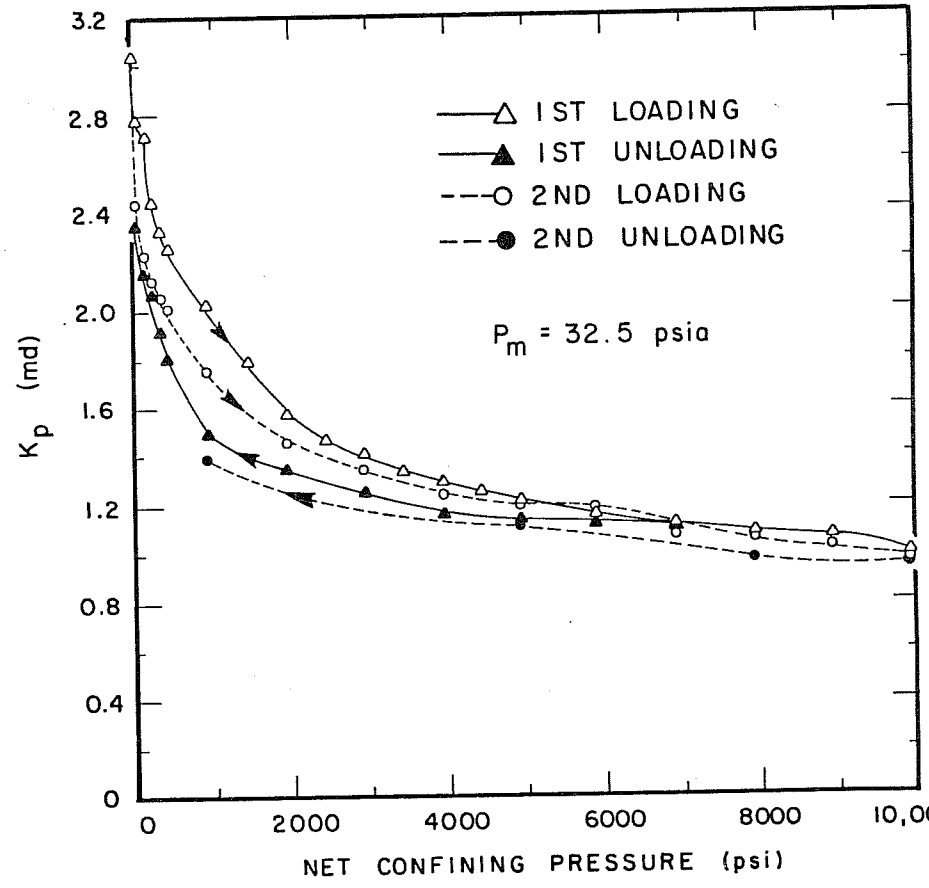

Fig. A1.2 Permeability vs. net confining pressure for 6405 core sample (Group ID 1; depth 6405.0 ft; vertical cut)

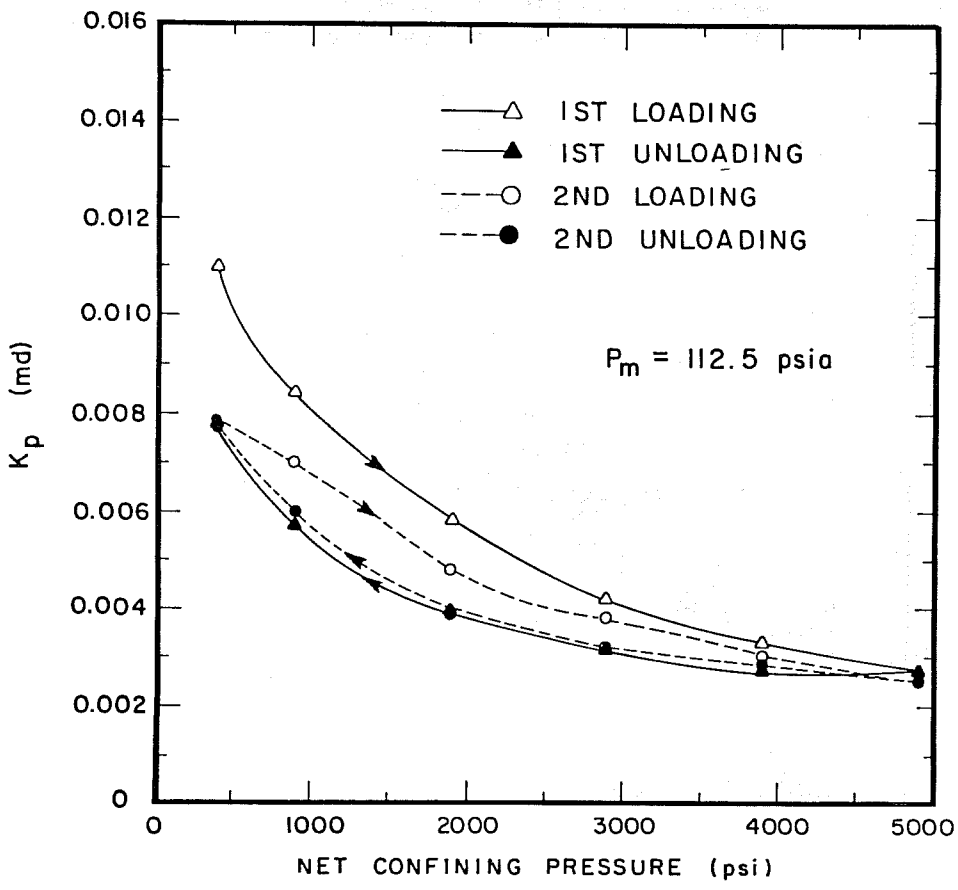

Fig. A1.3 Permeability vs. net confining pressure for 10570 S BETC core sample (Group ID 2; depth 10570.0 ft; horizontal cut)

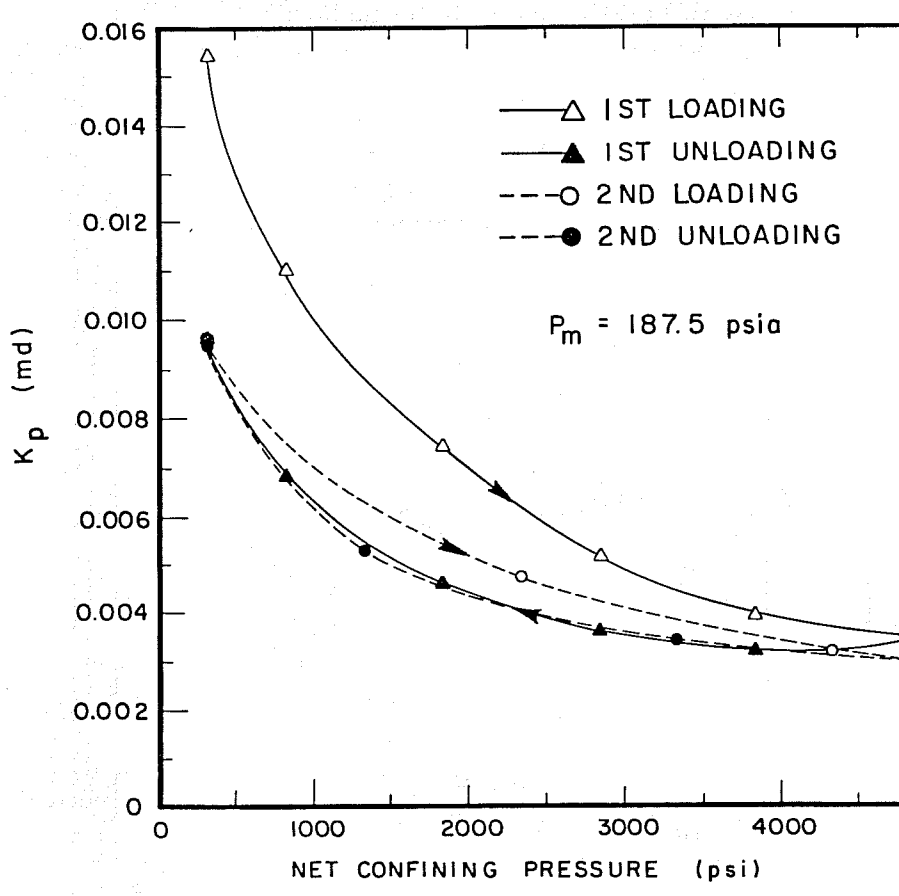

Fig. A1.4 Permeability vs. net confining pressure for 10570 S BETC core sample (Group ID 2; depth 10570 ft; vertical cut)

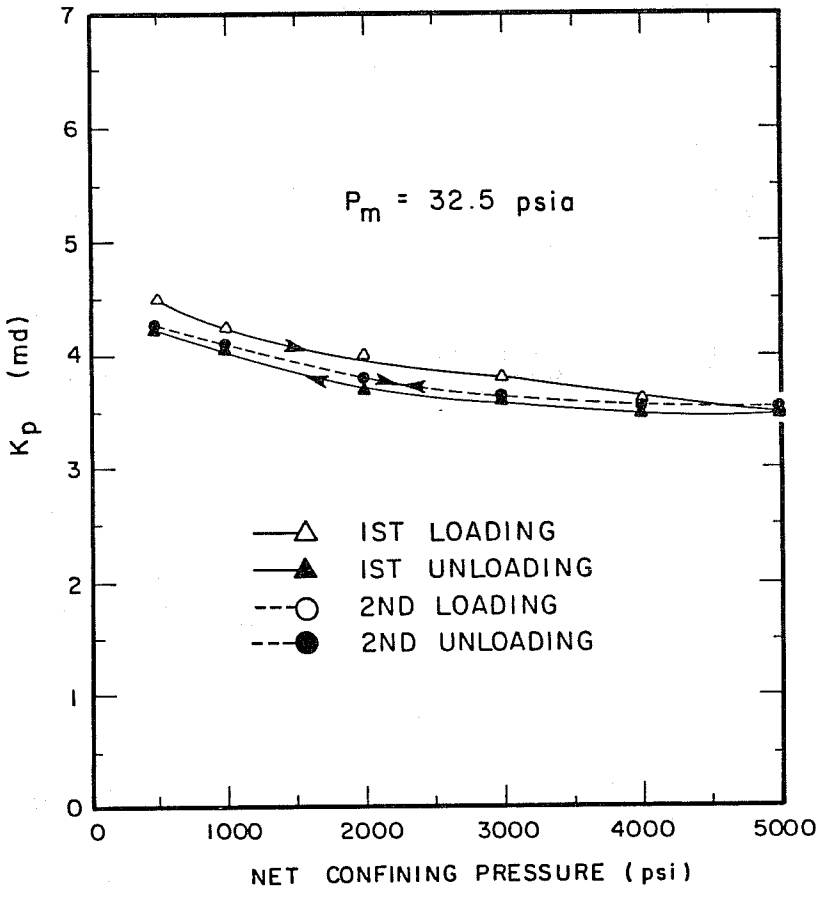

Fig. A1.5 Permeability vs. net confining pressure for Old Man Mountain #2 core sample (Group ID 3; depth 4498.0 ft horizontal cut)

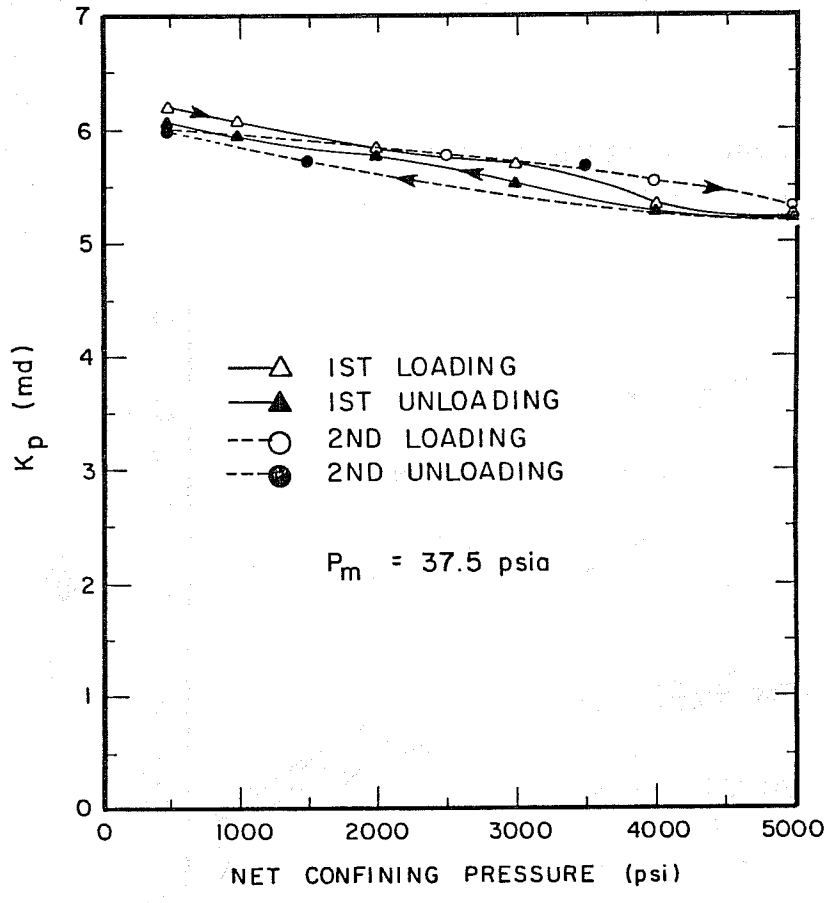

Fig. A1.6 Permeability vs. net confining pressure for Old Man Mountain #2 core sample (Group ID 3; depth 4498.0 ft; vertical cut)

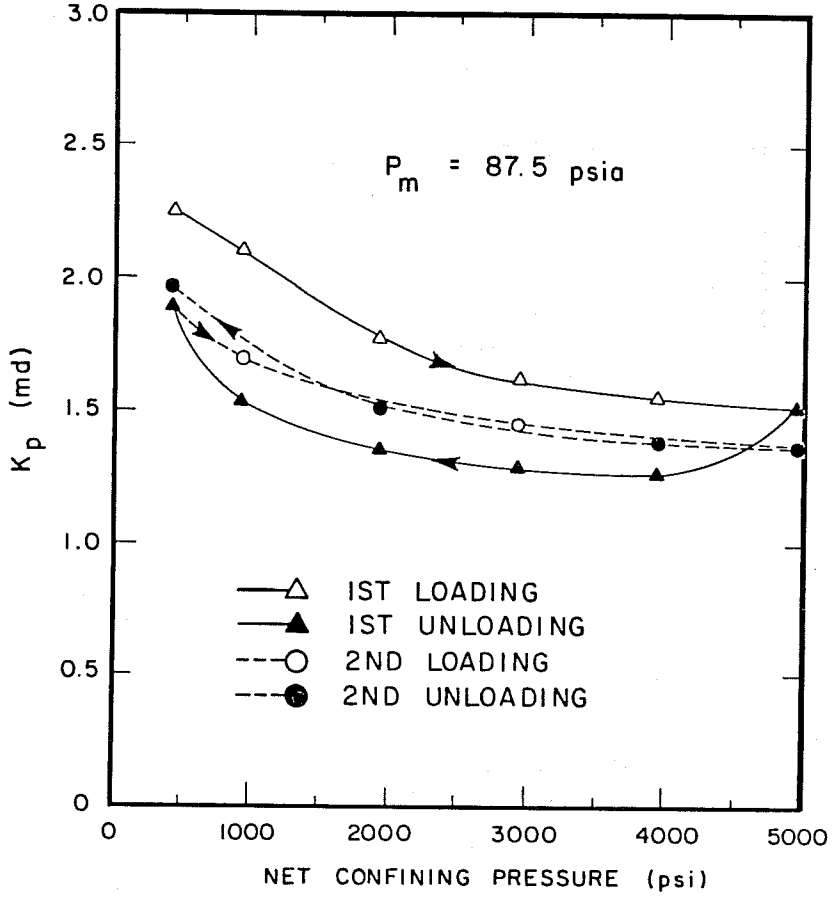

Fig. A1.7 Permeability vs. net confining pressure for Ralston Core sample (Group ID 4; depth 3713.0 ft; horizontal cut)

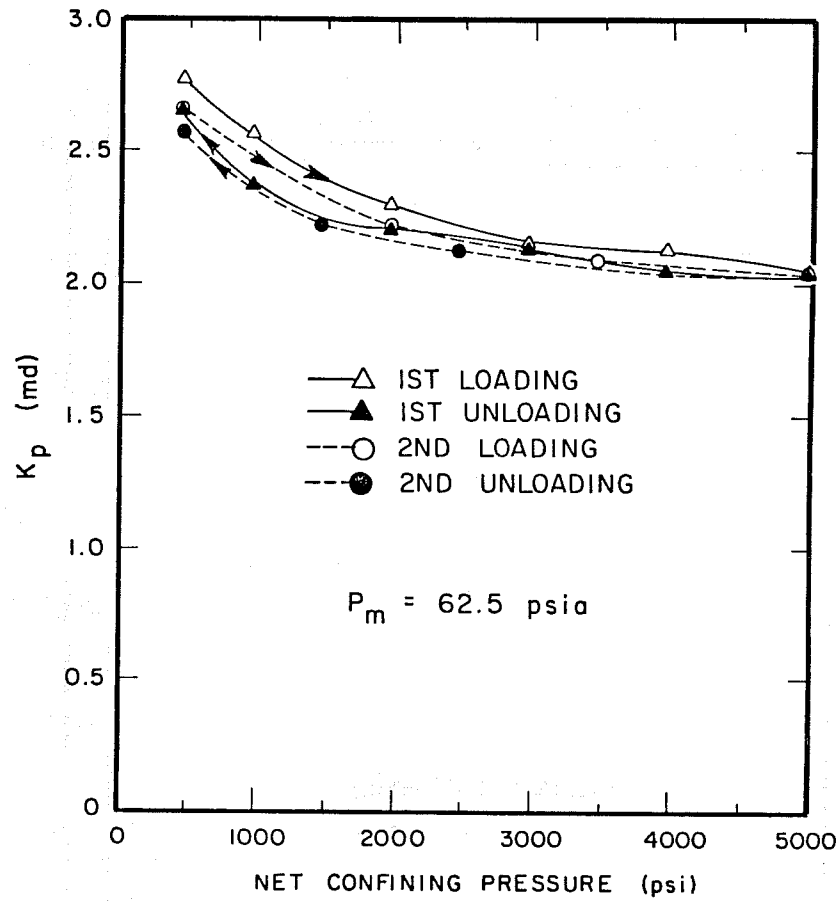

Fig. A1.8 Permeability vs. net confining pressure for Ralston Core sample (Group ID 4; depth 3713.0 ft; vertical cut)

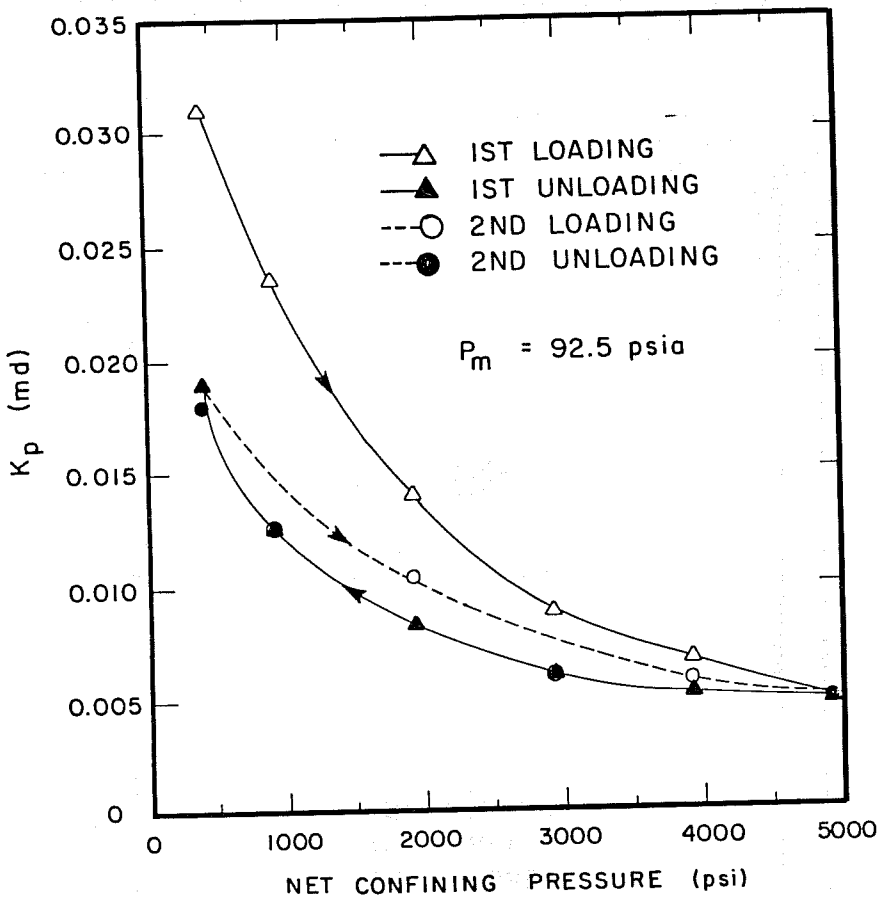

Fig. A1.9 Permeability vs. net confining pressure for BC-1-25 core sample (Group ID 5; depth 7277.0 ft; horizontal cut)

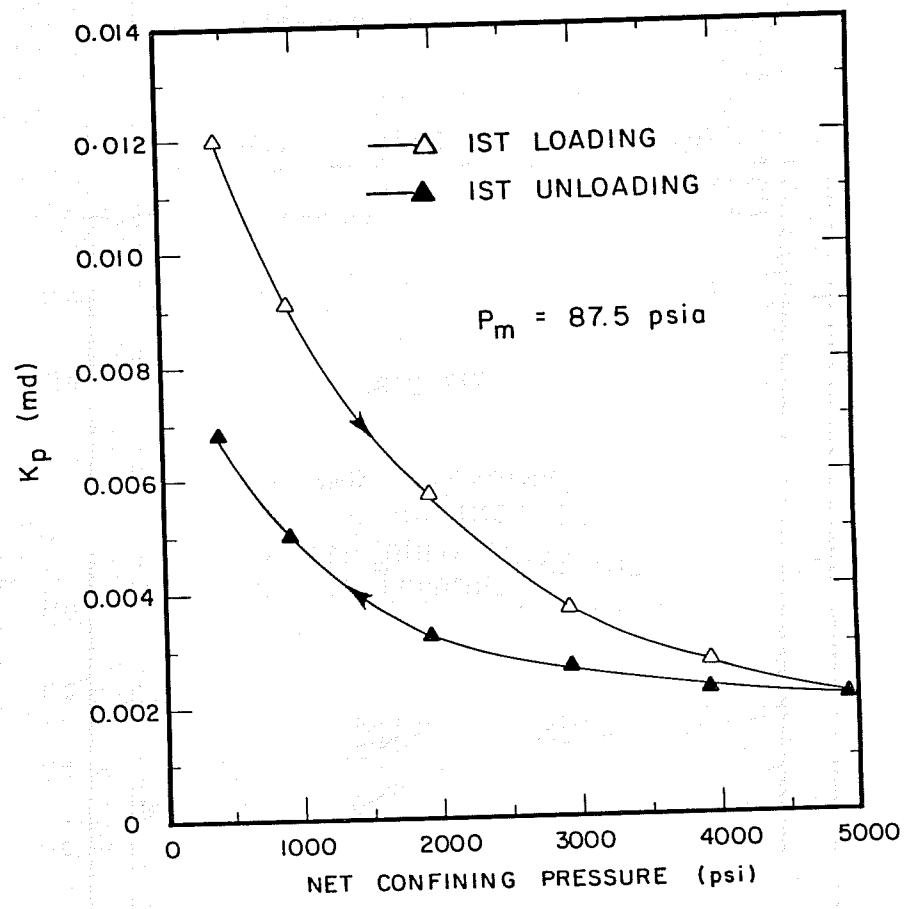

Fig. A1.10 Permeability vs. net confining pressure for PCUF31-13G core sample (Group ID 6; depth 8439.0 ft; horizontal cut)

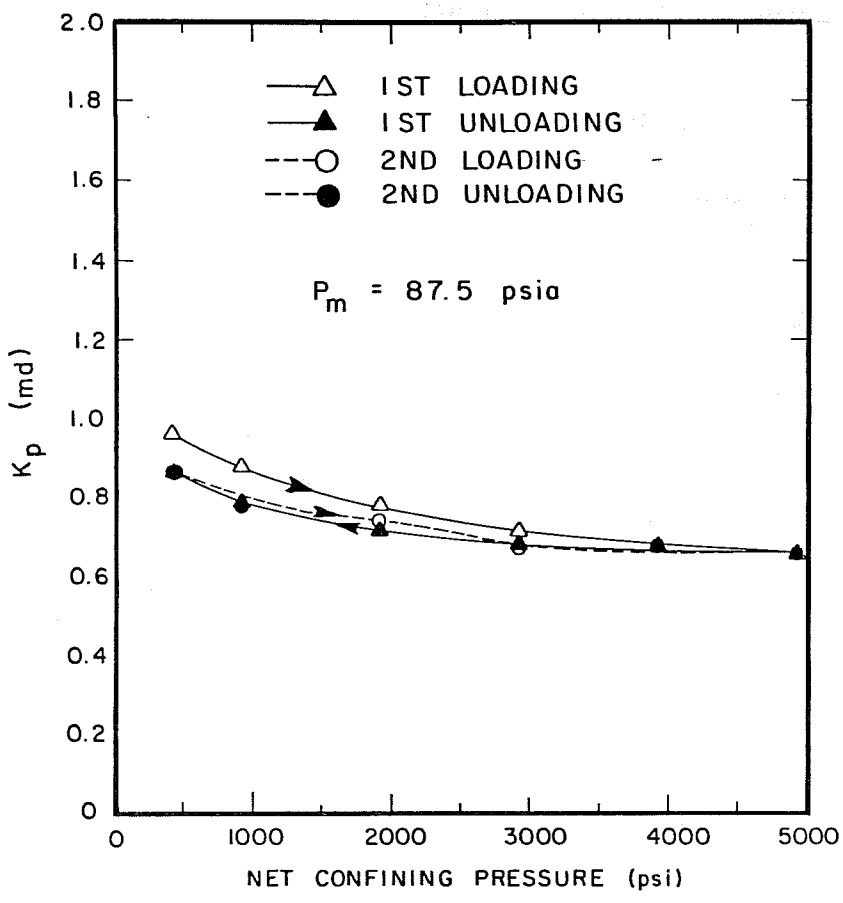

Fig. A1.11 Permeability vs. net confining pressure for CIGE 21 core sample (Group ID 7; depth 4403.3 ft; horizontal cut)

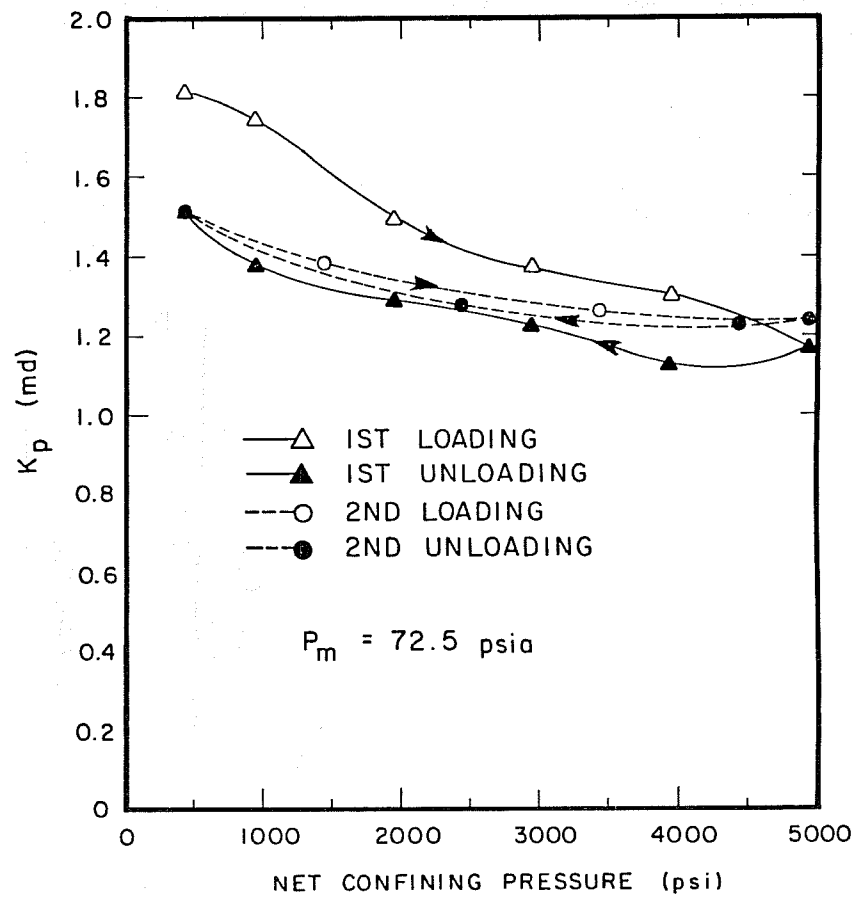

Fig. A1.12 Permeability vs. net confining pressure for CIGE 21 core sample (Group ID 7; depth 4403.3 ft; vertical cut)

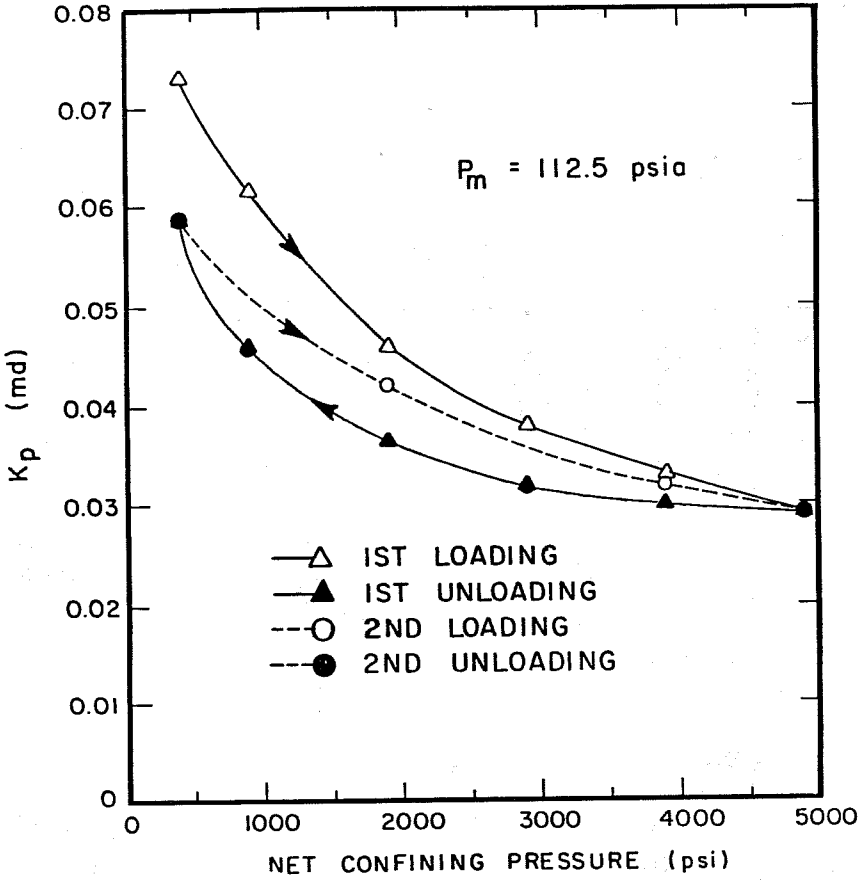

Fig. A1.13 Permeability vs. net confining pressure for CIGE 21 core sample (Group ID 8; depth 8492.0 ft; horizontal cut)

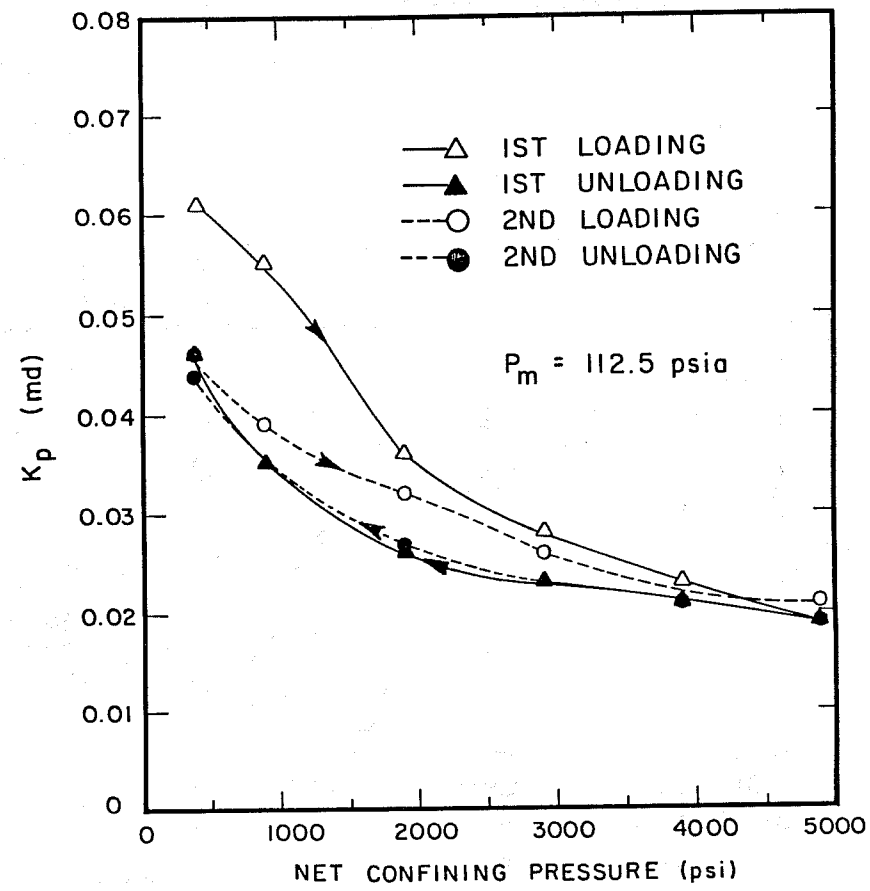

Fig. A1.14 Permeability vs. net confining pressure for CIGE 21 core sample (Group ID 8; depth 8492.0 ft; vertical cut)

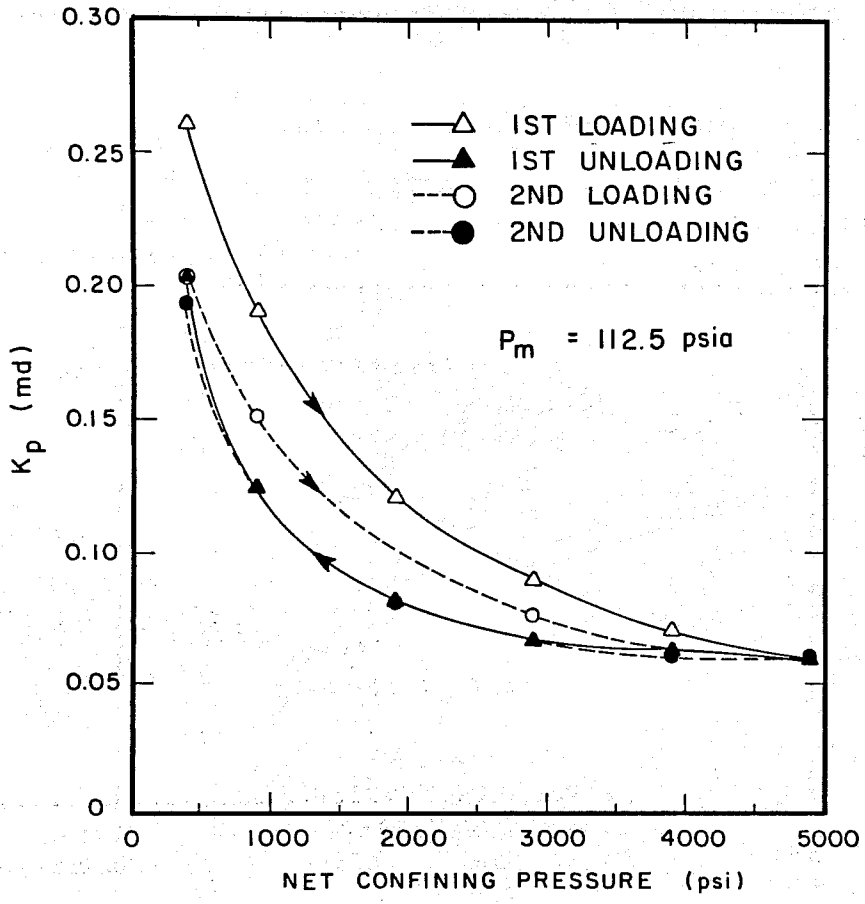

Fig. A1.15 Permeability vs. net confining pressure for CIGE 21 core sample (Group ID 9; depth 6503.0 ft; horizontal cut)

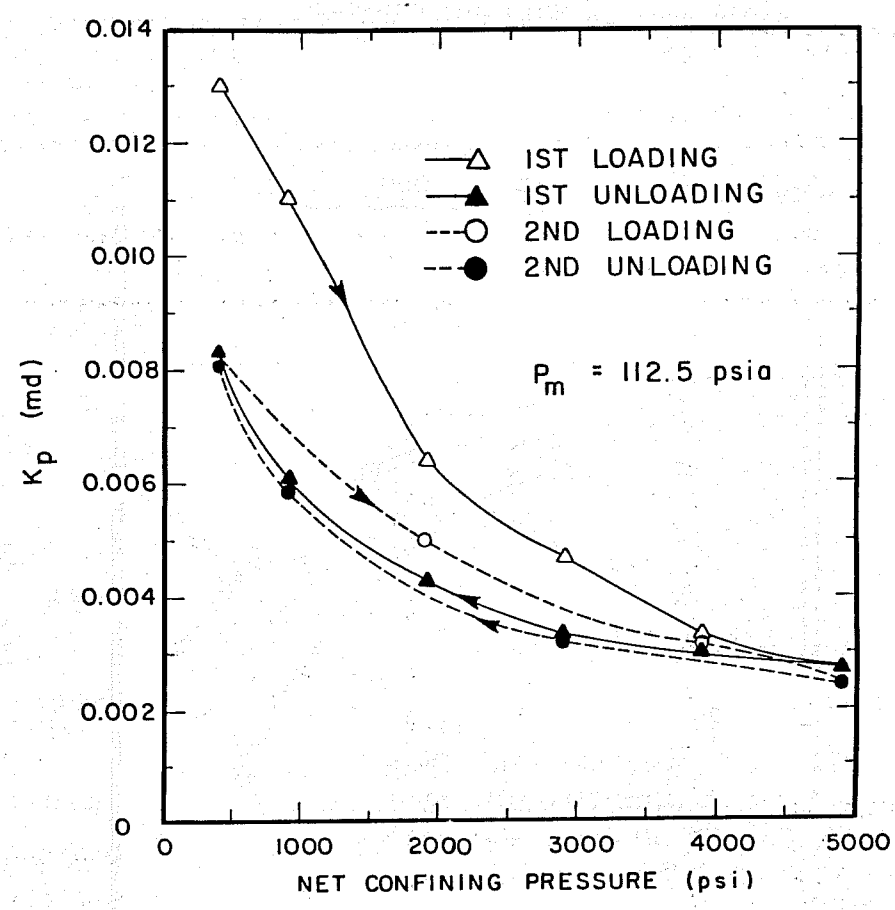

Fig. A1.16 Permeability vs. net confining pressure for U78JP16 core sample (Group ID 10; depth 8265.1 ft; horizontal cut)

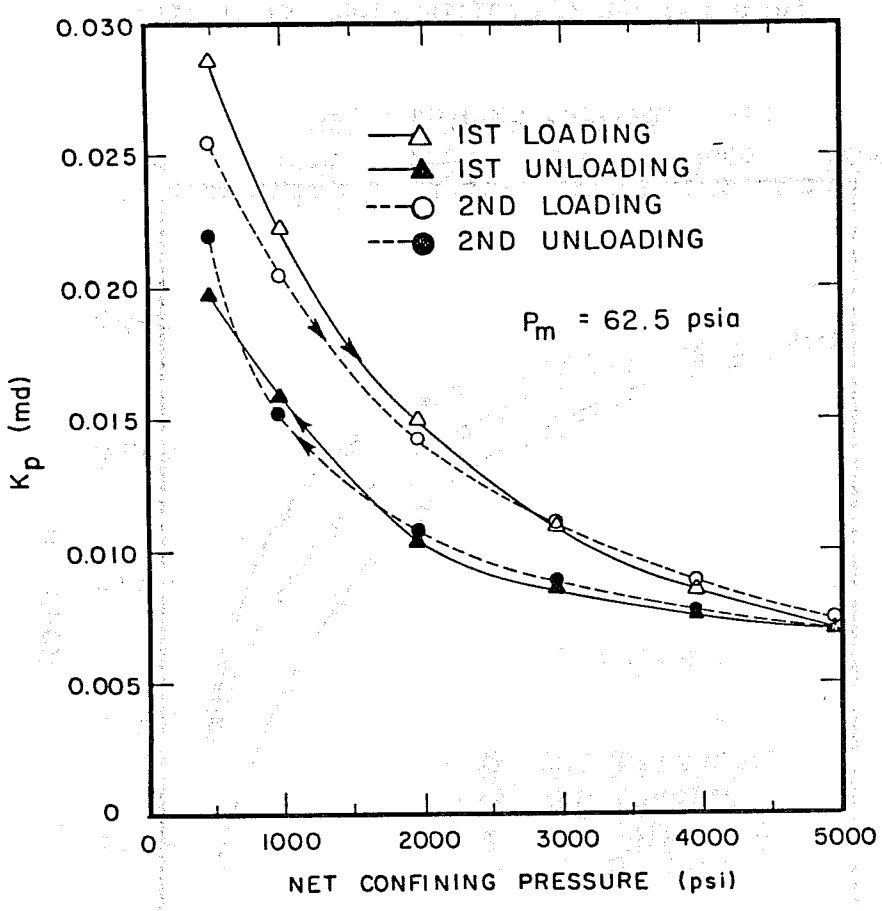

Fig. A1.17 Permeability vs. net confining pressure for U78JP36 core sample (Group ID 11; depth 8262.3 ft; horizontal cut)

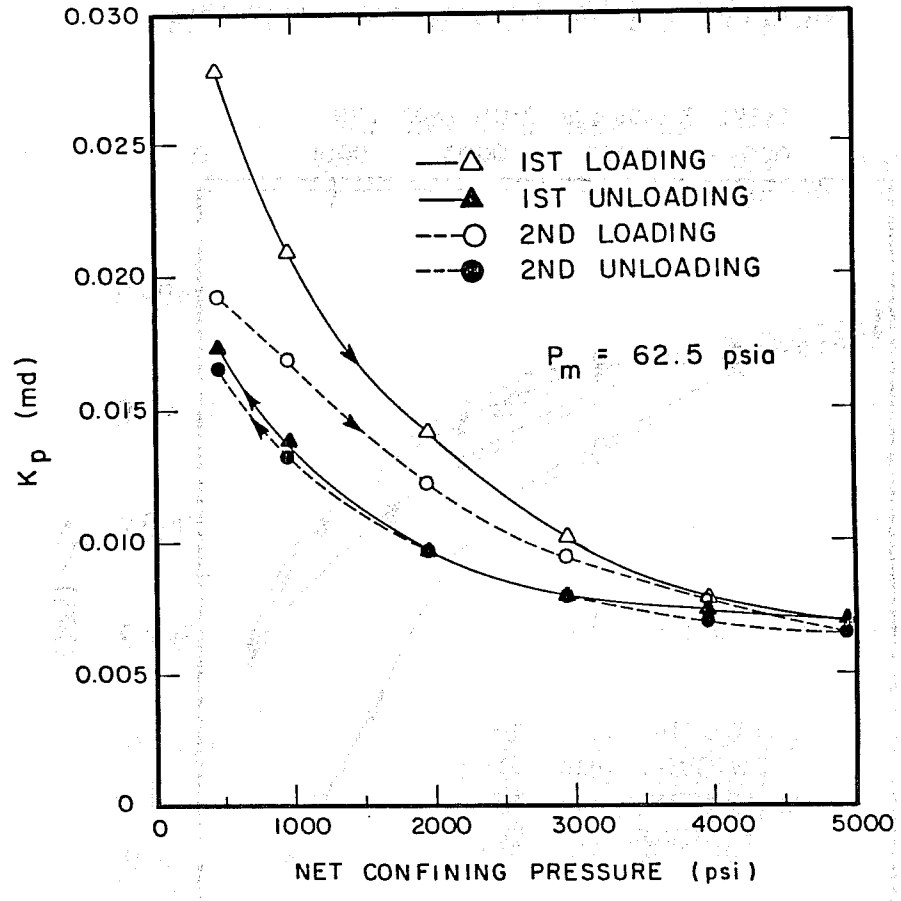

Fig. A1.18 Permeability vs. net confining pressure for U78PJ36 core sample (Group ID11; depth 8262.3 ft; vertical cut)

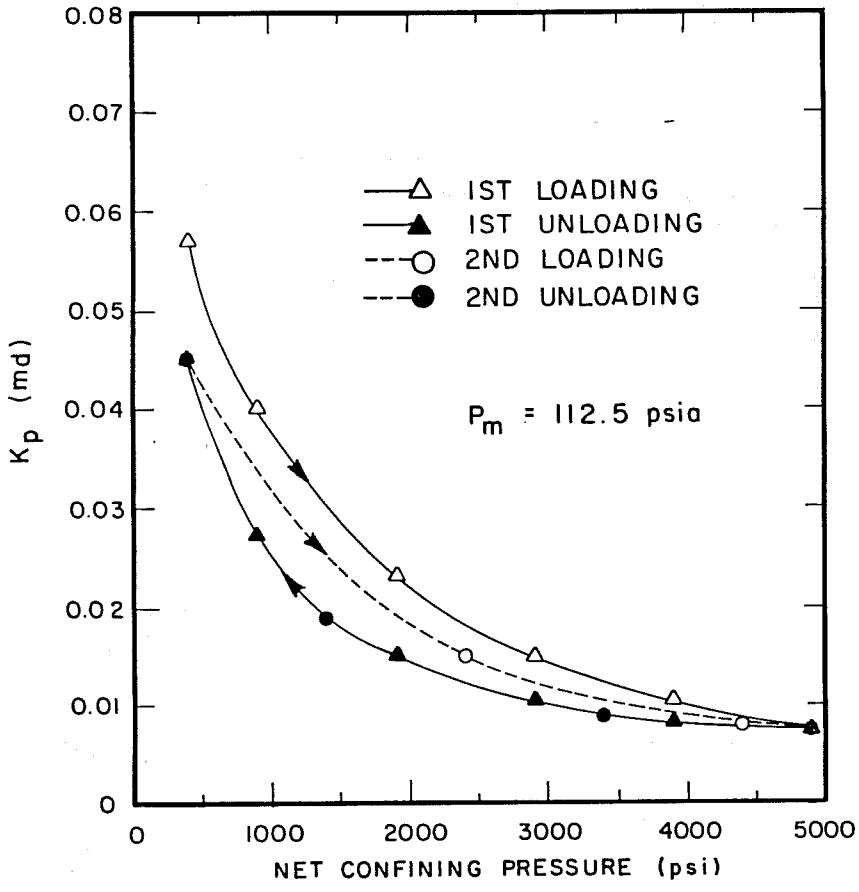

Fig. A1.19 Permeability vs. net confining pressure for Wilkin Ridge core sample (Group ID 12; depth 10298.7 ft; horizontal cut)

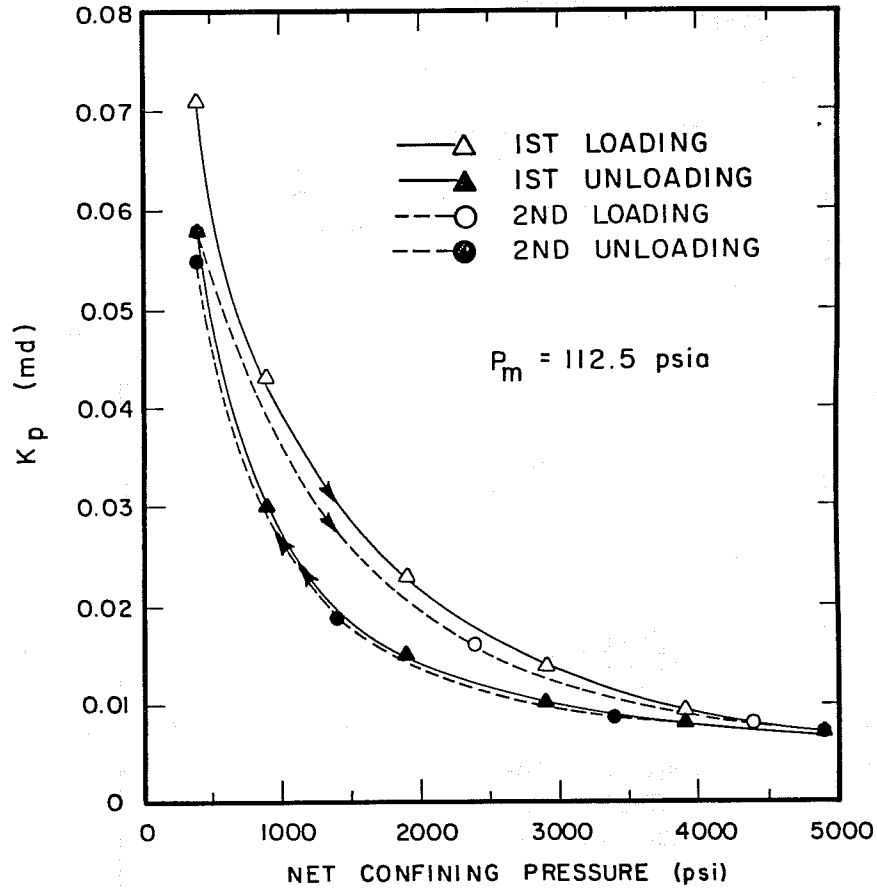

Fig. A1.20 Permeability vs. net confining pressure for Wilkin Ridge core sample (Group ID 12; depth 10298.7 ft; vertical cut)

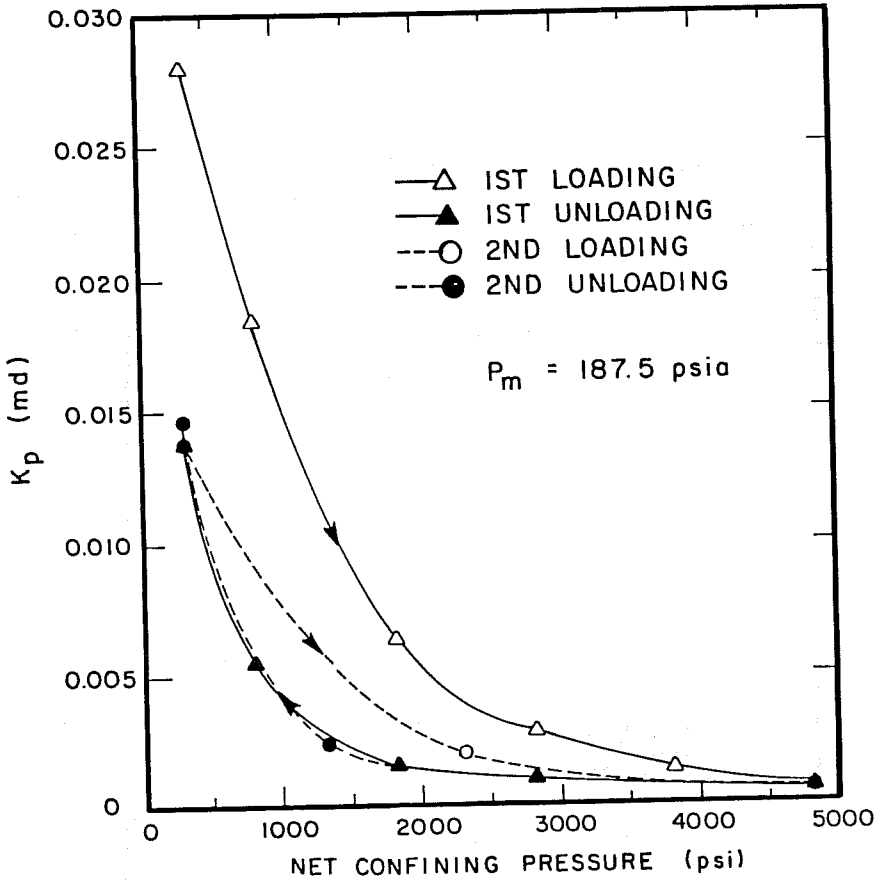

Fig. A1.21 Permeability vs. net confining pressure for RBE-01 core sample (Group ID 13; depth 5863.6 ft)

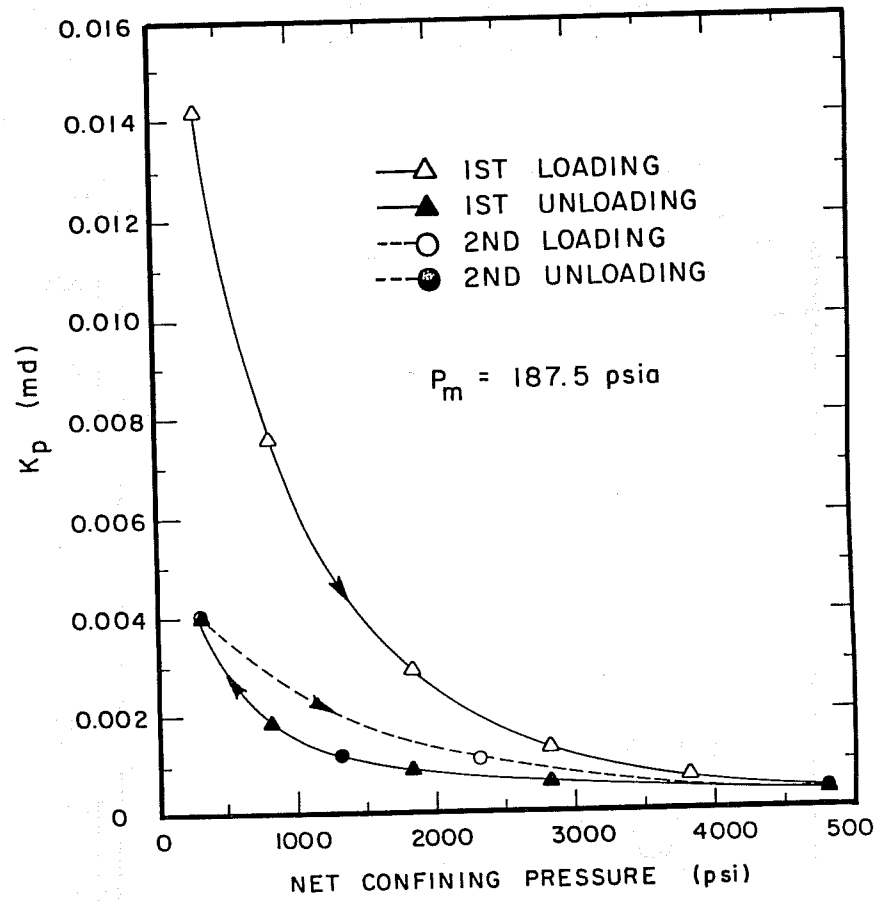

Fig. A1.22 Permeability vs. net confining pressure for RBE-01 core sample (Group ID 14; depth 5898.5 ft)

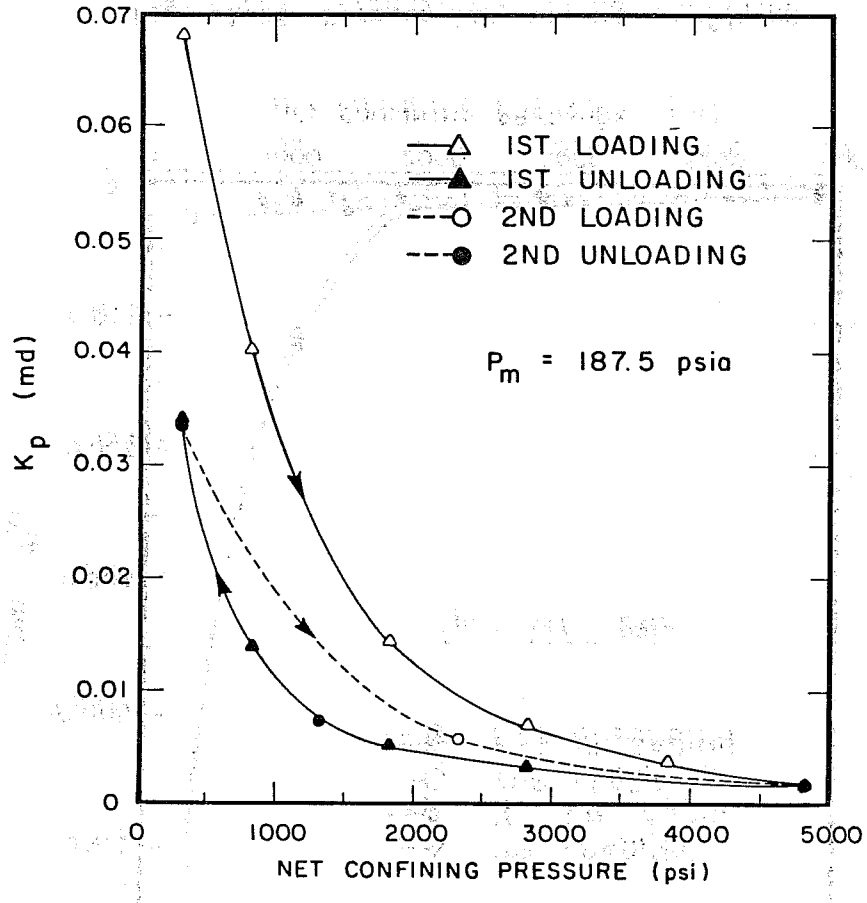

Fig. A1.23 Permeability vs. net confining pressure for PTS 22-12 core sample (Group ID 17; depth 6403.0 ft)

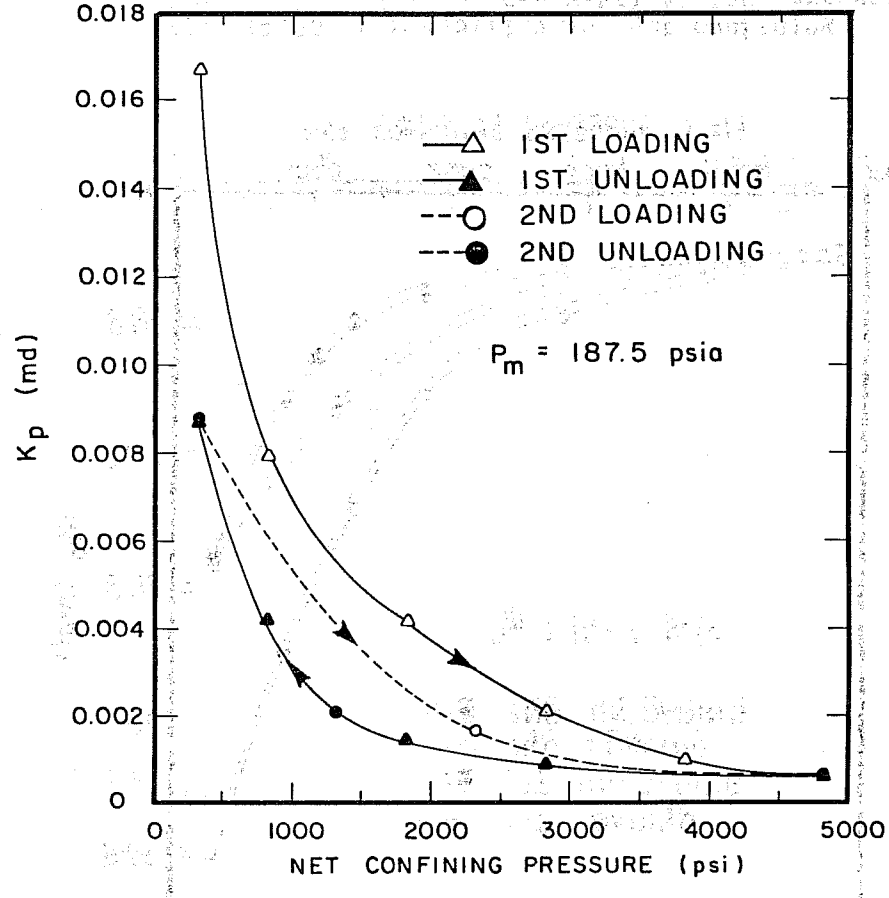

Fig. A1.24 Permeability vs. net confining pressure for PTS 22-12 core sample (Group ID 18; depth 6431.0 ft)

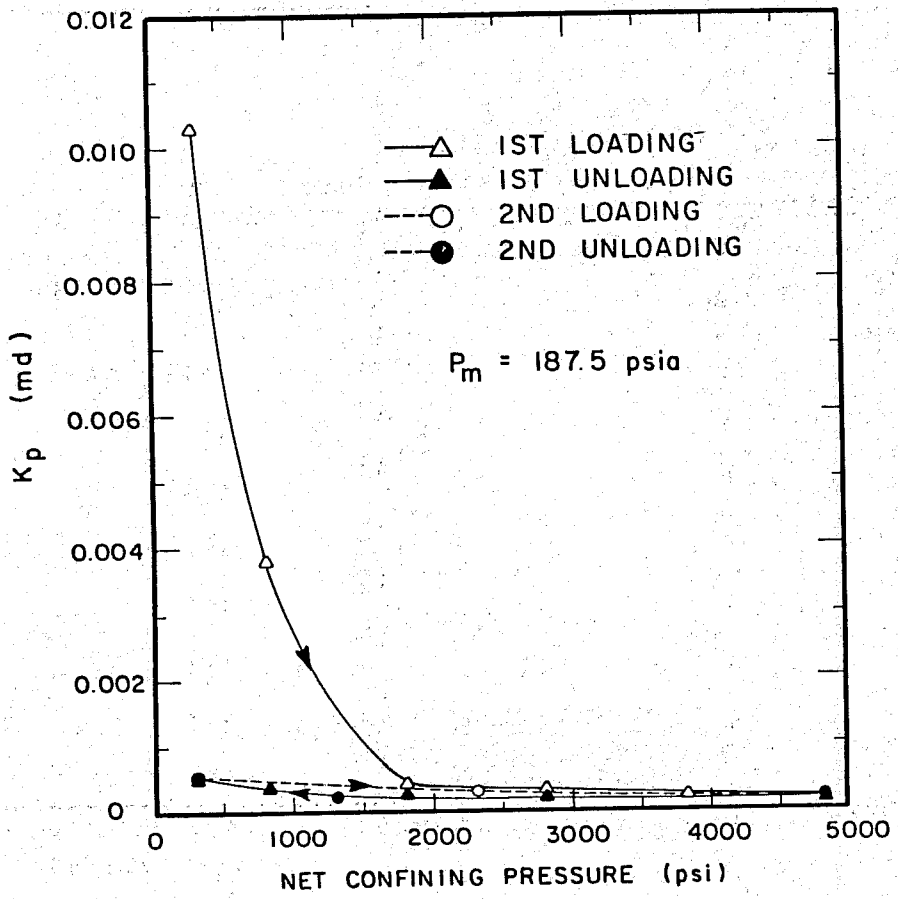

Fig. A1.25 Permeability vs. net confining pressure for PTS 22-12 core sample (Group ID 19; depth 6509.6 ft)

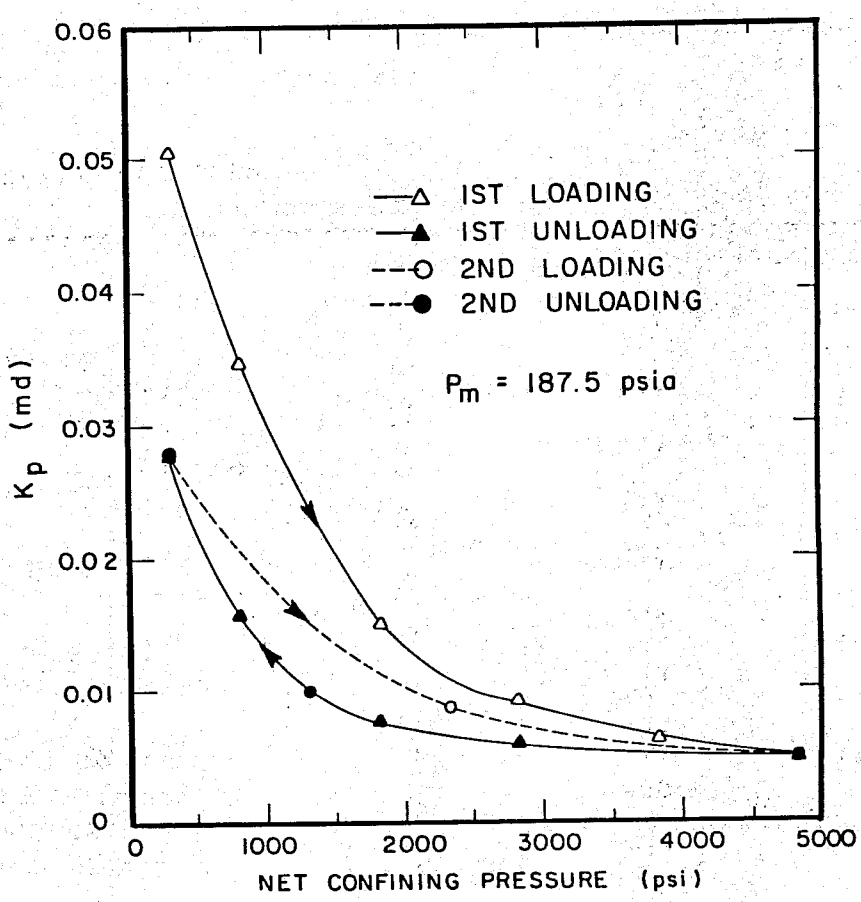

Fig. A1.26 Permeability vs. net confining pressure for Mobil 45-14G core samp (Group ID 20; depth 5140.0 ft)

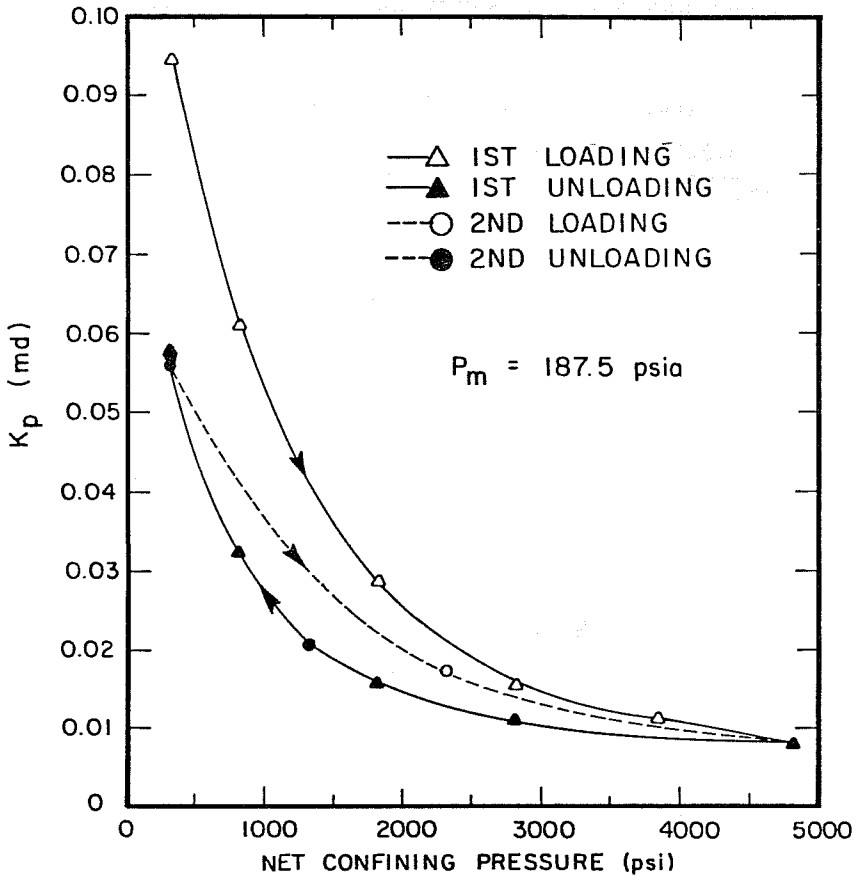

Fig. A1.27 Permeability vs. net confining pressure for Mobil 26-7G core sample (Group ID 21; depth 3309.0 ft)

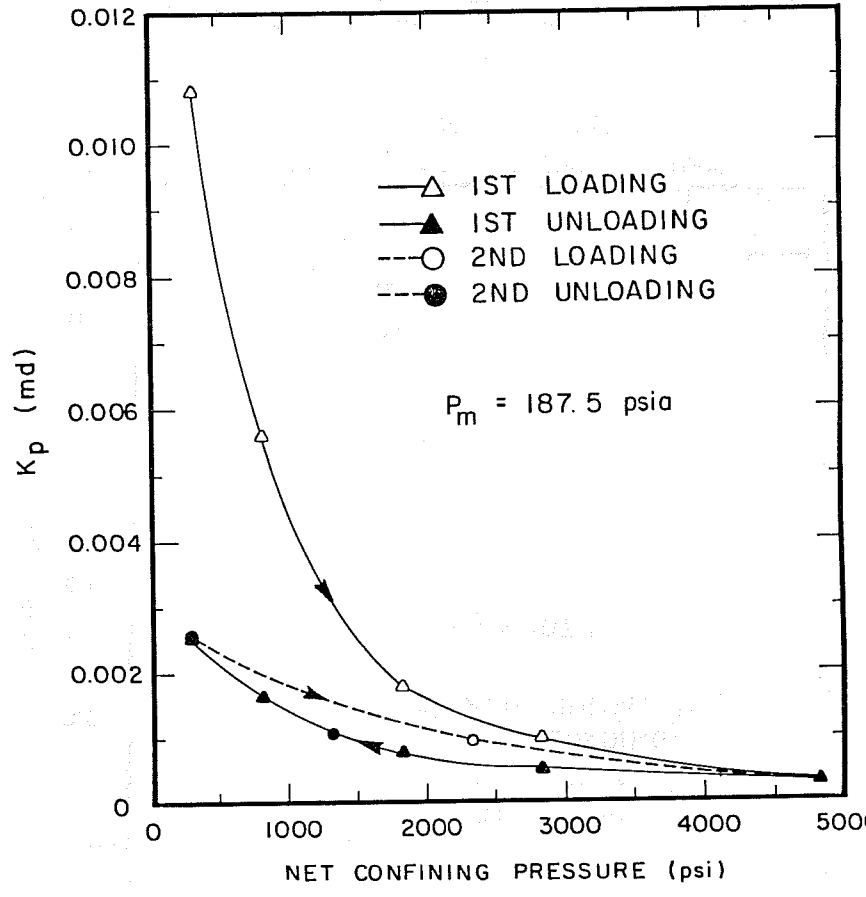

Fig. A1.28 Permeability vs. net confining pressure for Mobil 26-7G core samp (Group ID 22; depth 2924.0 ft)

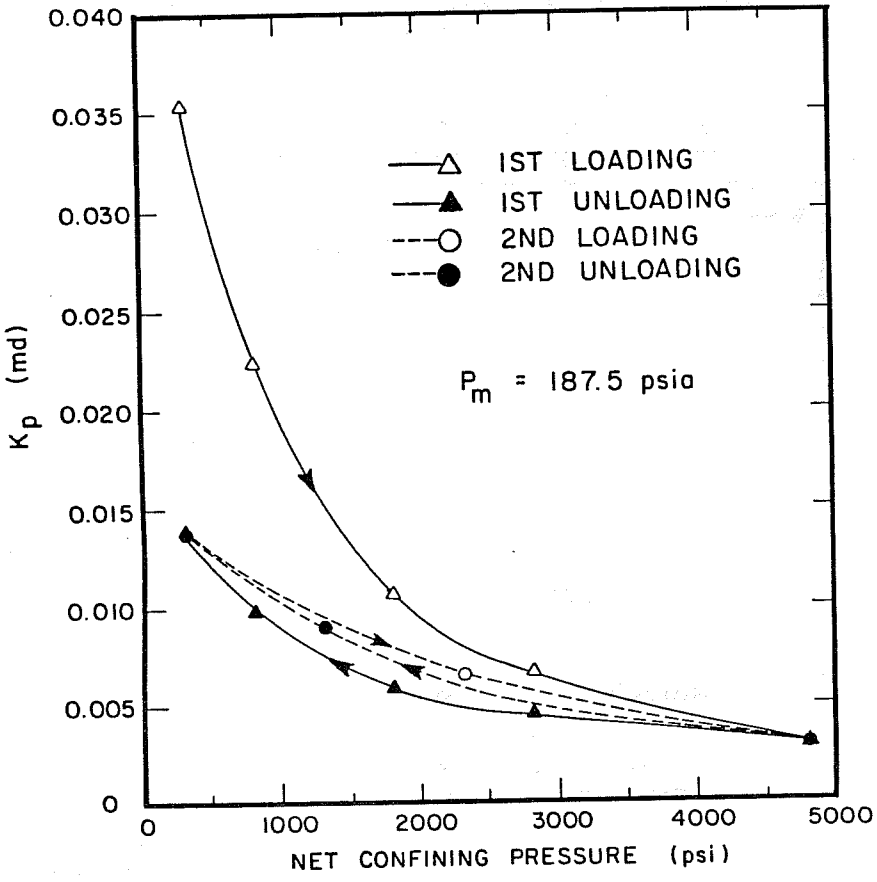

Fig. A1.29 Permeability vs. net confining pressure for OMM #2 Colo core sample (Group ID 23; depth 5457.0 ft)

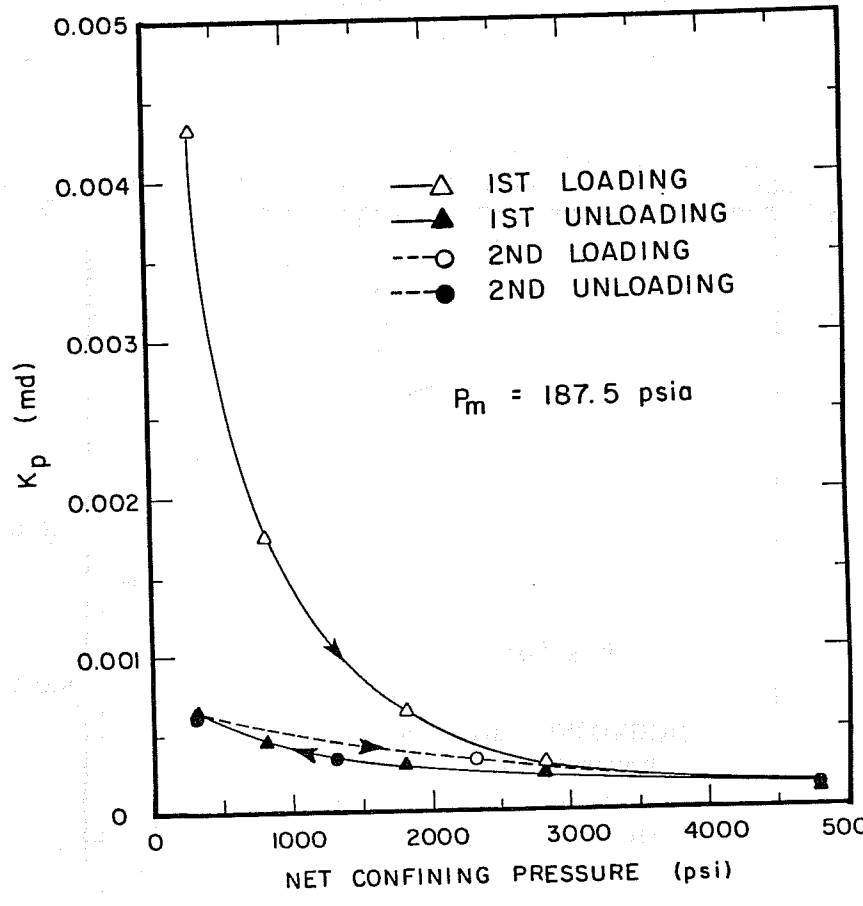

Fig. A1.30 Permeability vs. net confining pressure for OMM #2 Colo core sampl (Group ID 24; depth 5469.4 ft)

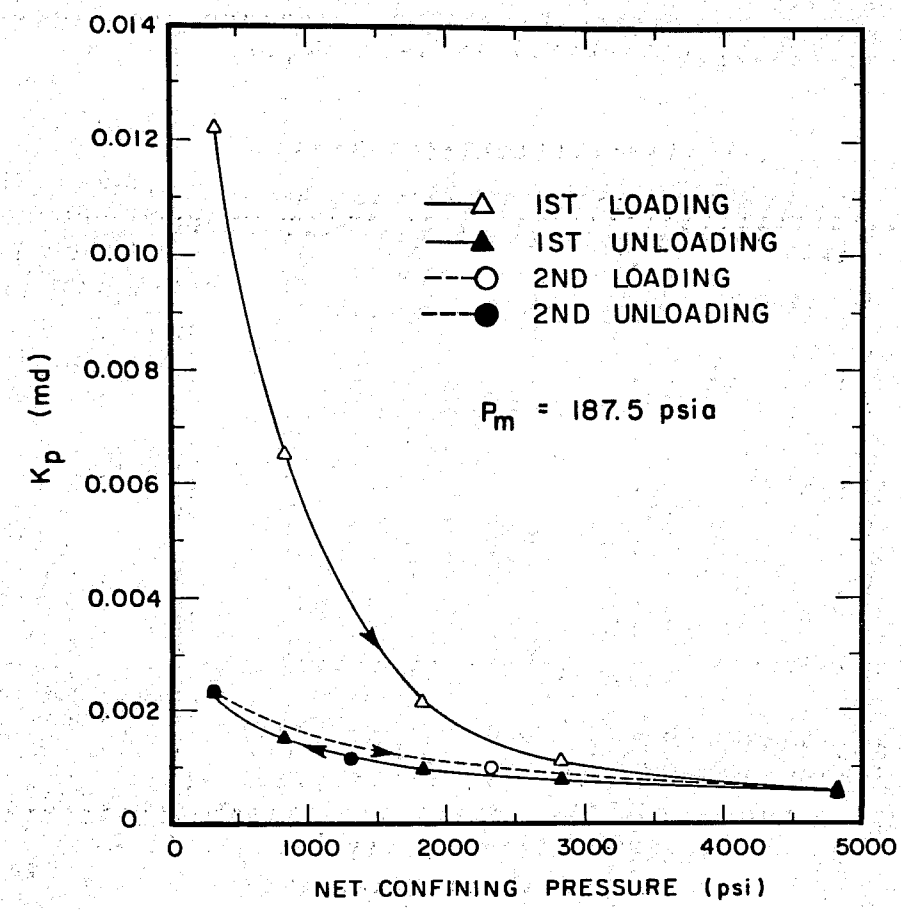

Fig. A1.31 Permeability vs. net confining pressure for Arco-Exxon L-36 core sample
(Group ID 25; depth 3701.0 ft)

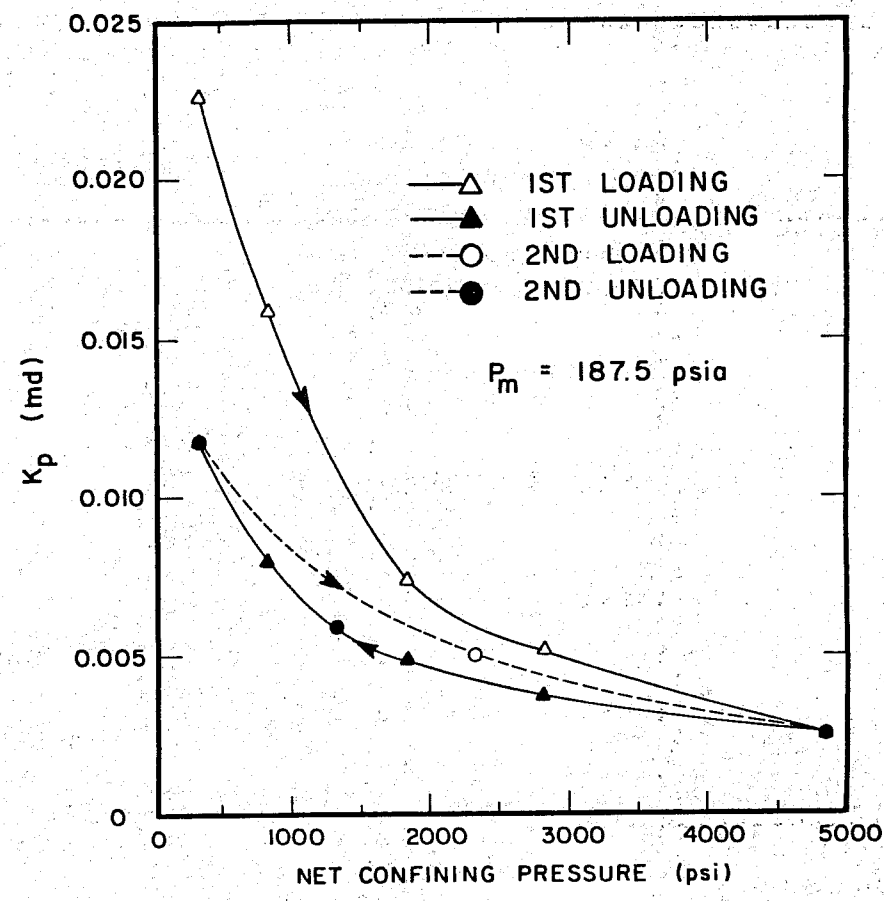

Fig. A1.32 Permeability vs. net confining pressure for 3014-15 core sample
(Group ID 25)

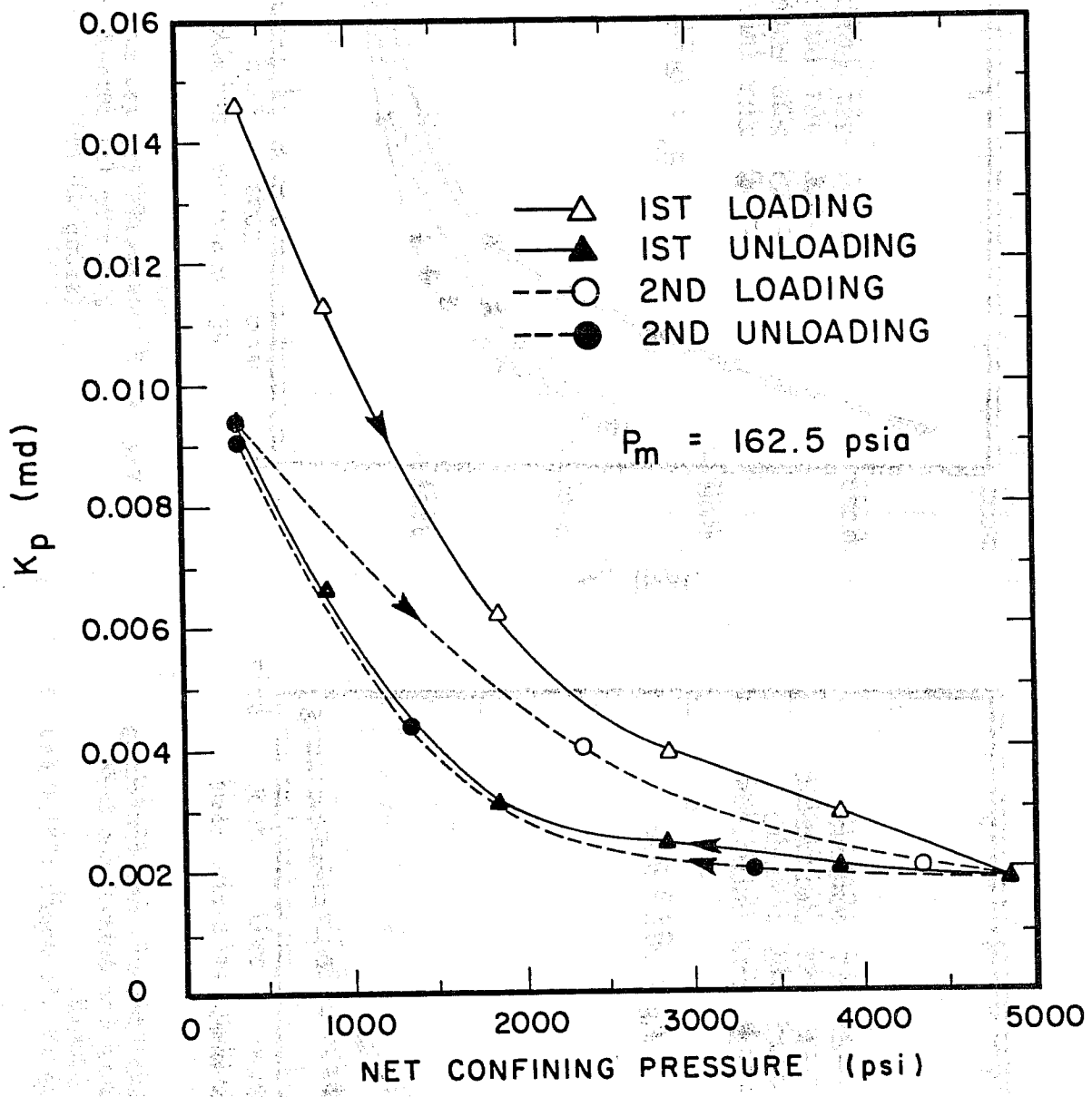

Fig. A1.33 Permeability vs. net confining pressure for (MWX-1) 42-25 core sample (Group ID 51; depth 6512.4 ft; vertical cut from bottom of whole core sample; nitrogen inlet pressure = 300 psig)

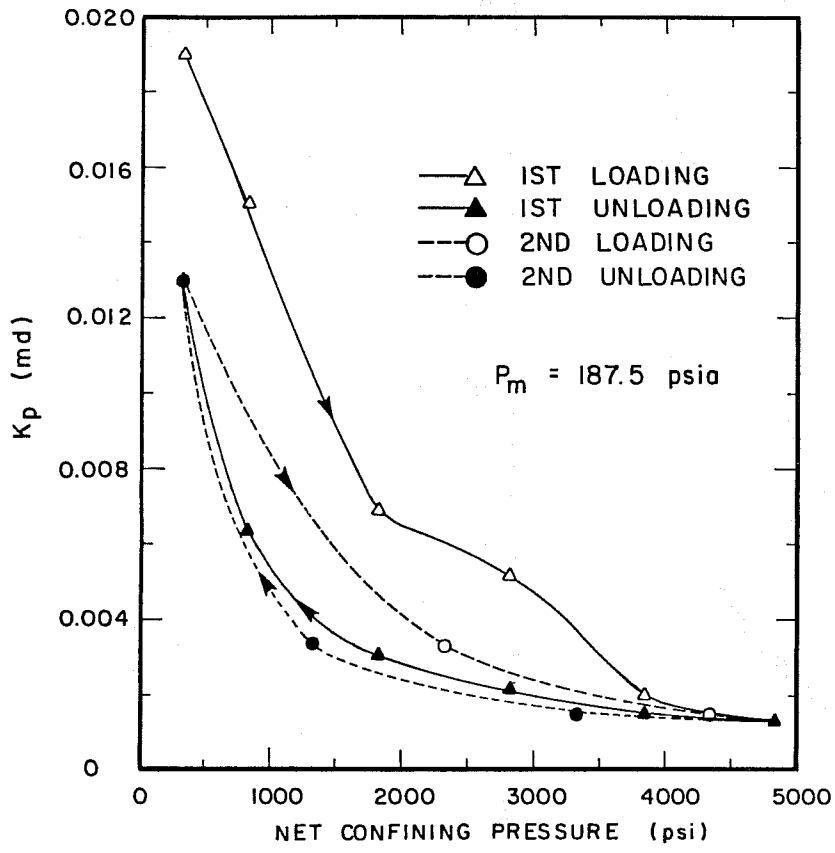

Fig. A1.34 Permeability vs. net confining pressure for (MWX-1) 31-32 core sample (Group ID 52; depth 5840.6 ft; horizontal cut from top of whole core sample; nitrogen inlet pressure = 350 psig)

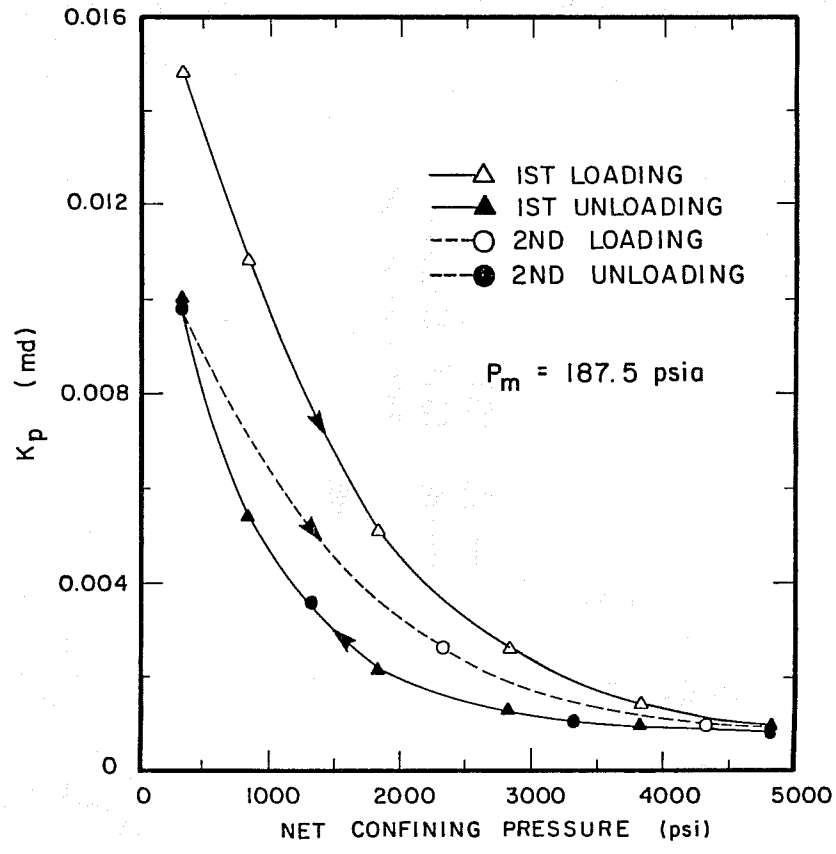

Fig. A1.35 Permeability vs. net confining pressure for (MWX-1) 31-32 core sample (Group ID 52; depth 5840.6 ft; vertical cut from top of whole core sample; nitrogen inlet pressure = 350 psig)

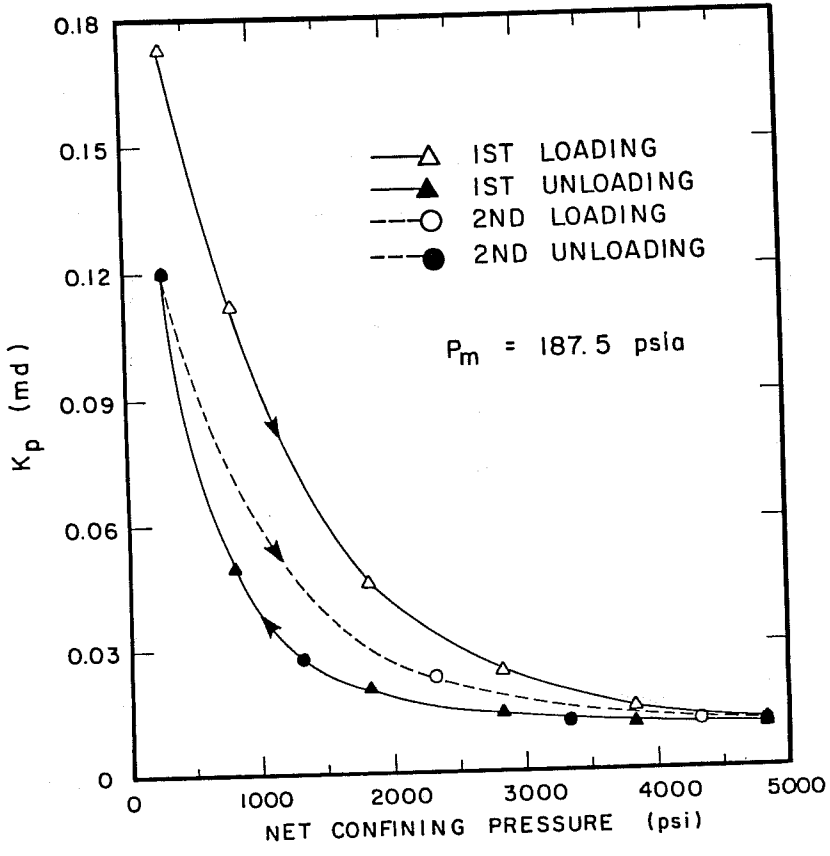

Fig. A1.36 Permeability vs. net confining pressure for (MWX-1) 14-14 core sample (Group ID 53; depth 4917.0 ft; horizontal cut from top of whole core sample; nitrogen inlet pressure = 350 psig)

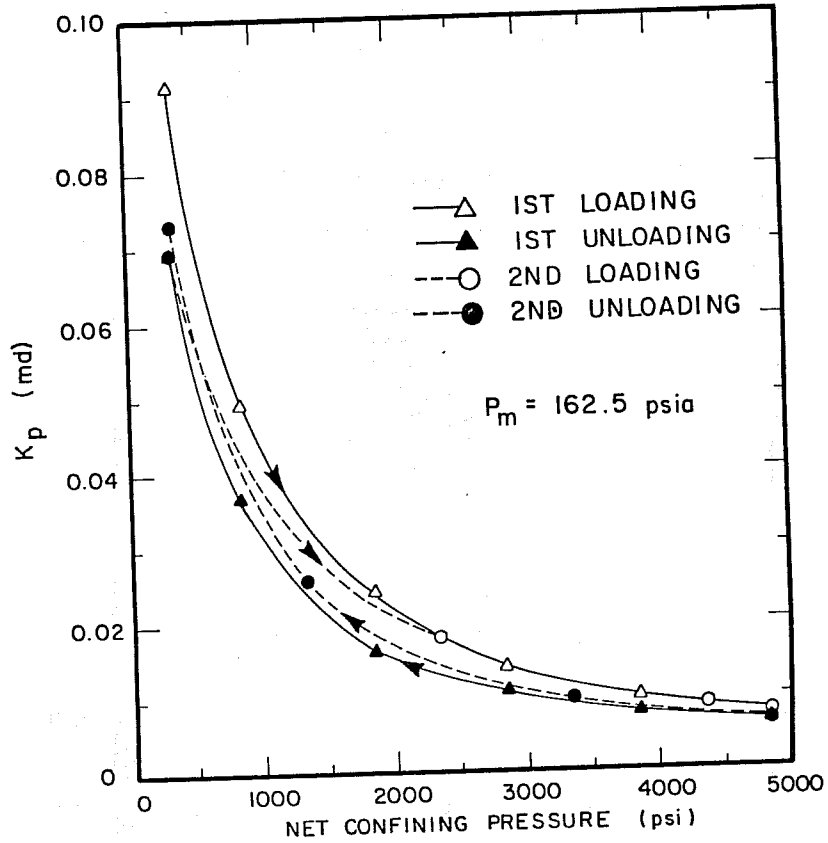

Fig. A1.37 Permeability vs. net confining pressure for (MWX-1) 14-14 core sample (Group ID 53; depth 4917.0 ft; vertical cut from top of whole core sample; nitrogen inlet pressure = 350 psig)

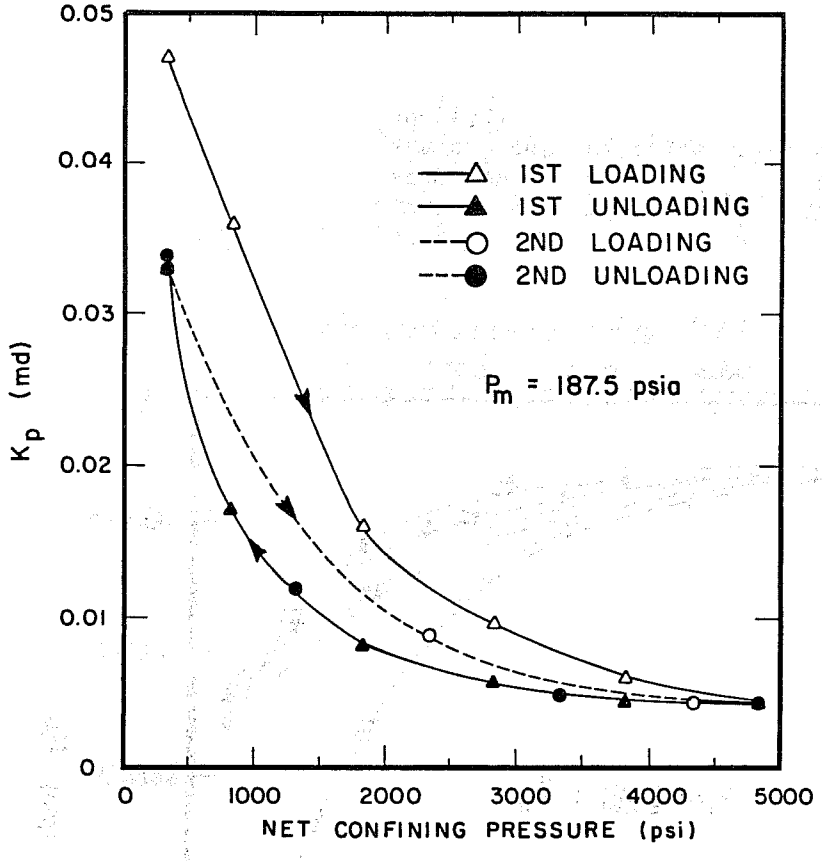

Fig. A1.38 Permeability vs. net confining pressure for (MWX-2) 48-9 core sample (Group ID 54; depth 5731.0 ft; horizontal cut; nitrogen inlet pressure = 350 psig)

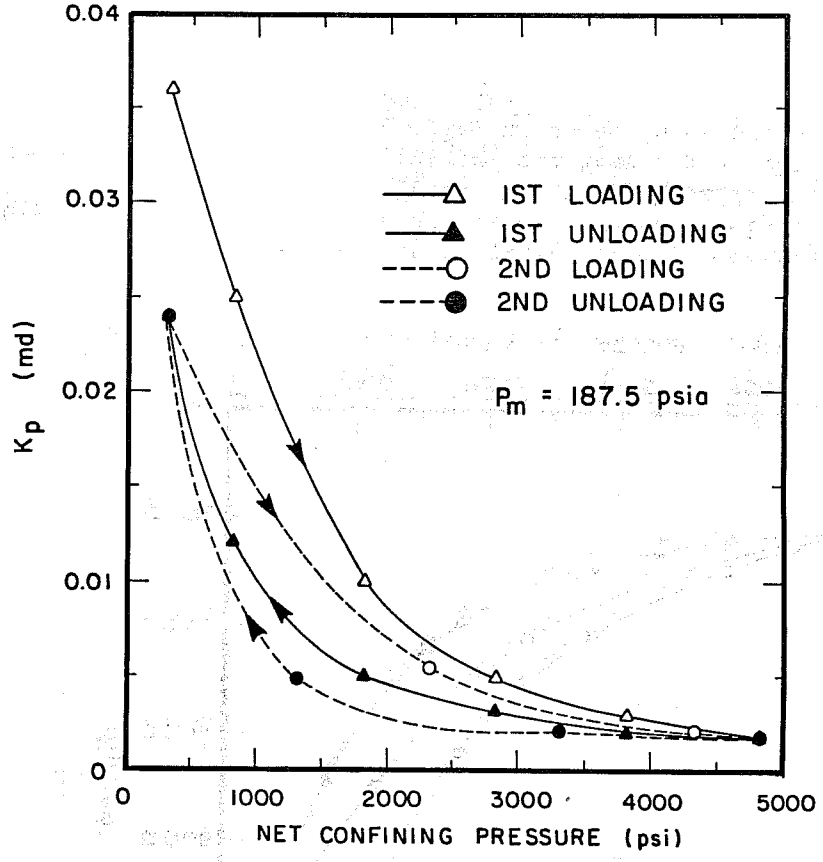

Fig. A1.39 Permeability vs. net confining pressure for (MWX-2) 48-9 core sample (Group ID 54; depth 5731.0 ft; vertical cut; nitrogen inlet pressure = 350 psig)

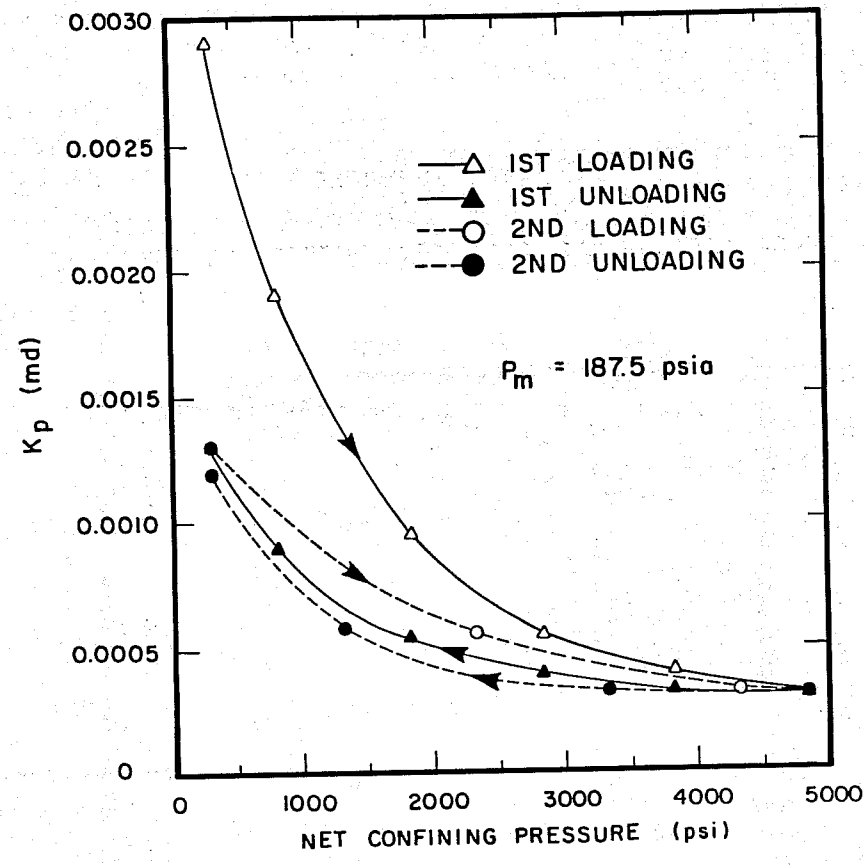

Fig. A1.40 Permeability vs. net congining pressure for (MWX-2) 56-19 core sample (Group ID 55; depth 7878.7 ft; vertical cut; nitrogen inlet pressure = 350 psig)

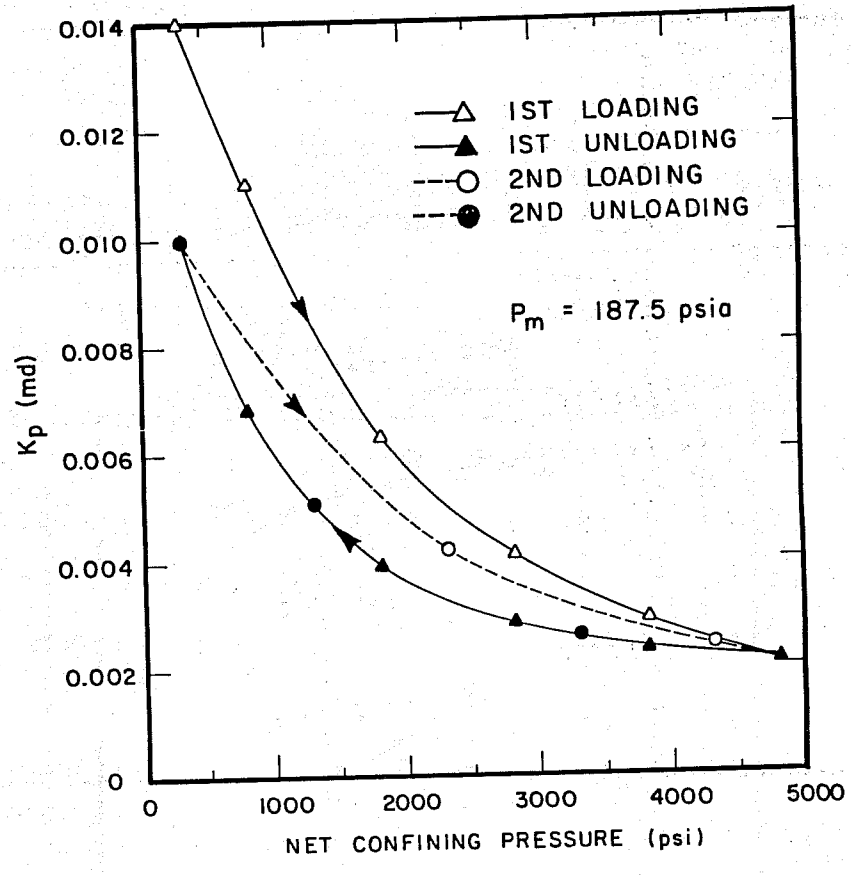

Fig. A1.41 Permeability vs. net confining pressure for (MWX-2) 51-10 core sample (Group ID 56; depth 6259.0 ft; vertical cut from top of whole core sample; nitrogen inlet pressure = 350 psig)

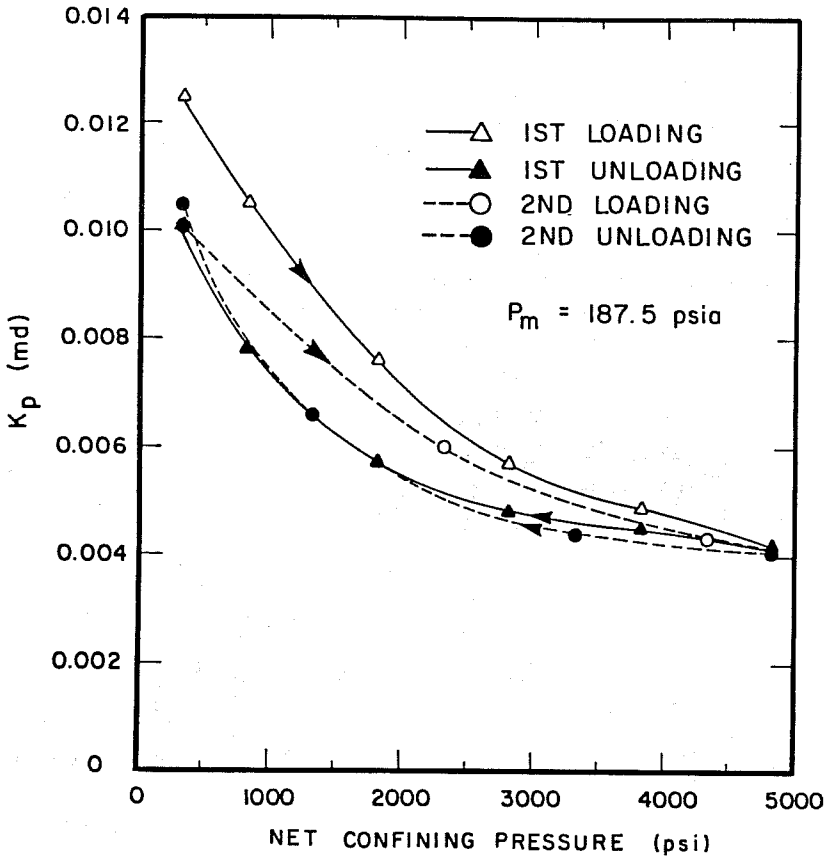

Fig. A1.42 Permeability vs. net confining pressure for (MWX-2) 52-15 core sample (Group ID 57; depth 7133.8 ft; vertical cut from top of whole core sample; nitrogen inlet pressure = 350 psig)

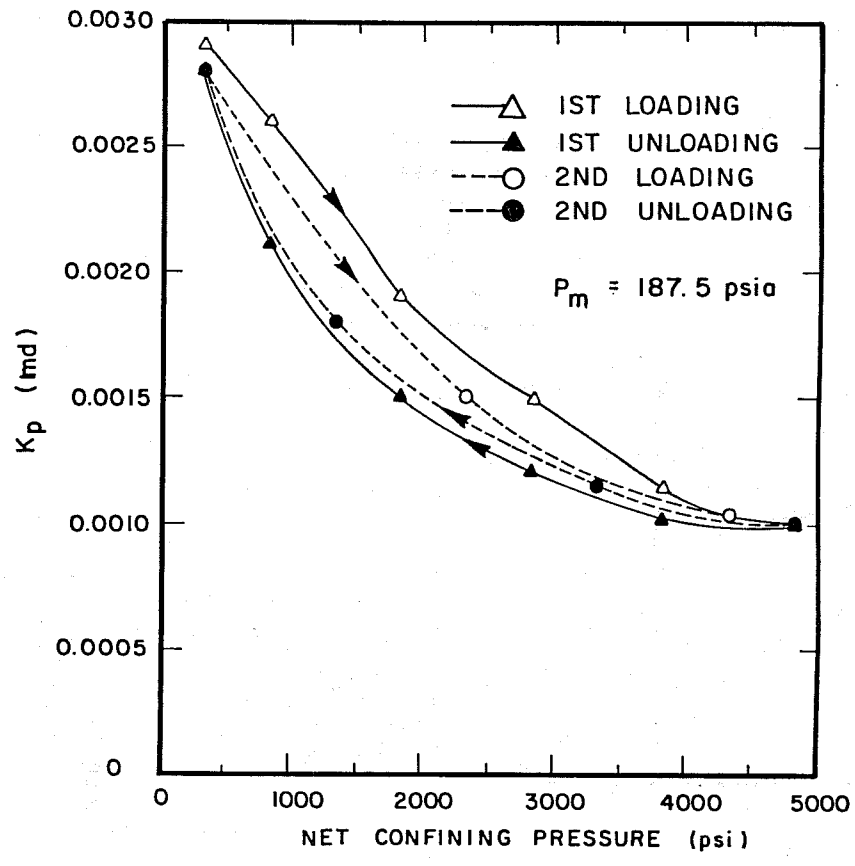

Fig. A1.43 Permeability vs. net confining pressure for (MWX-2) 52-15 core sample (Group ID 57; depth 7134.0 ft; vertical cut from bottom of whole core sample; nitrogen inlet pressure = 350 psig)

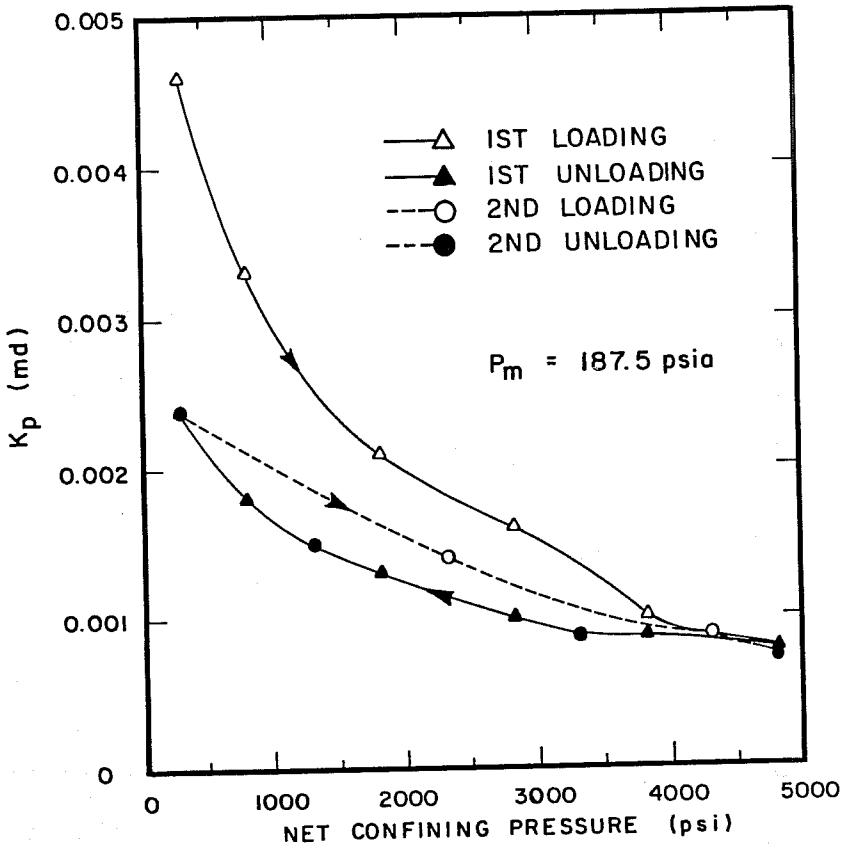

Fig. A1.44 Permeability vs. net confining pressure for (MWX-2) 42-11 core sample (Group ID 58; depth 7267.5 ft; vertical cut from top of whole core sample; nitrogen inlet pressure = 350 psig)

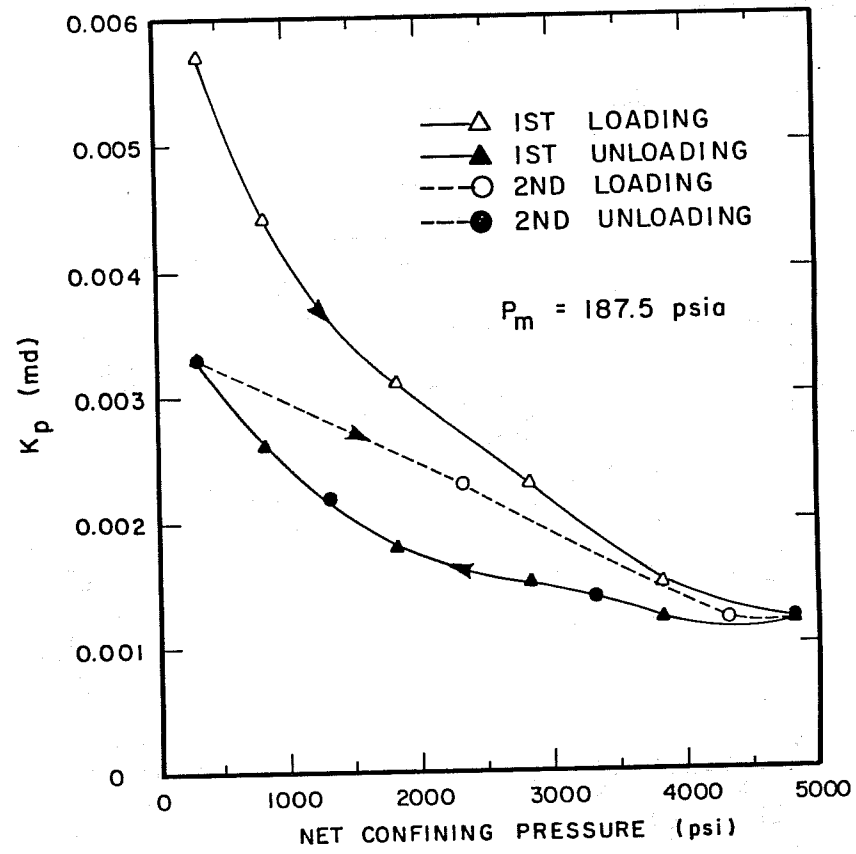

Fig. A1.45 Permeability vs. net confining pressure for (MWX-2) 54-11 core sample (Group ID 58; depth 7268.1 ft; vertical cut from bottom of whole core sample; nitrogen inlet pressure = 350 psig)

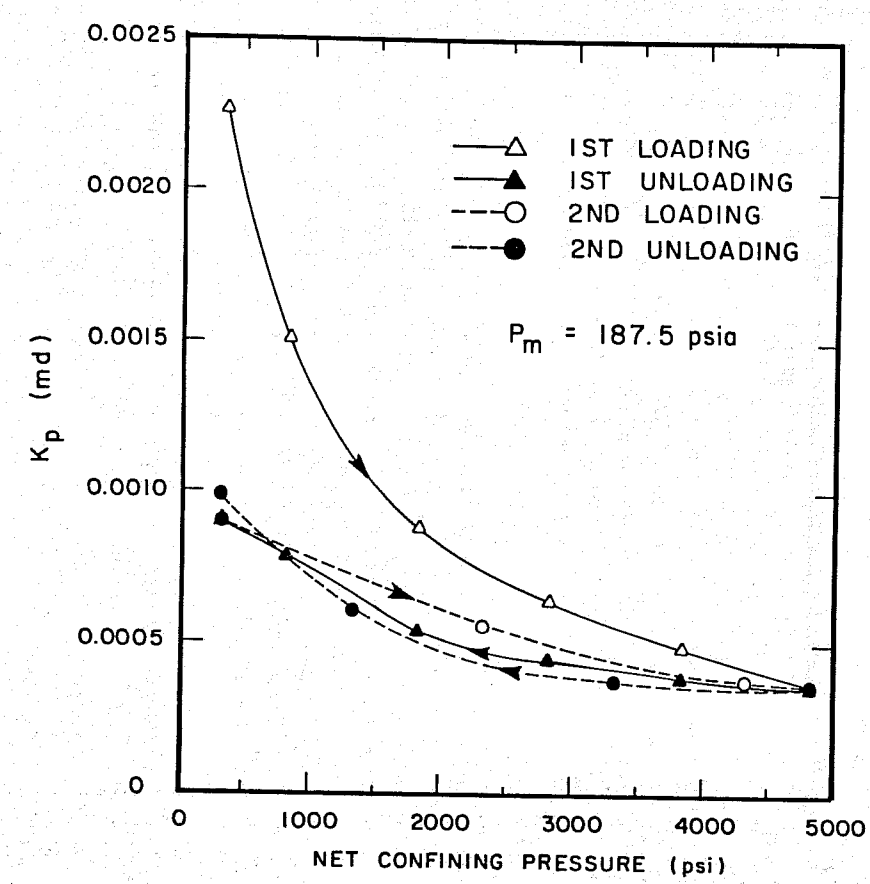

Fig. A1.46 Permeability vs. net confining pressure for (MWX-2) 55-16 core sample (Group ID 59; depth 7362.2 ft; vertical cut from top of whole core sample; nitrogen inlet pressure = 350 psig)

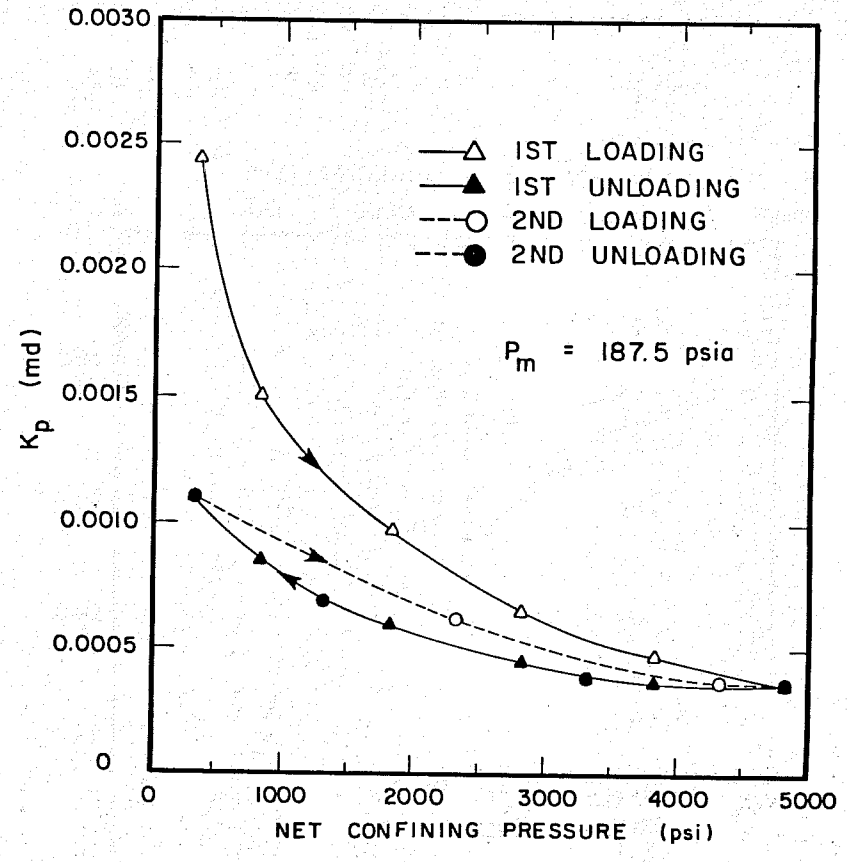

Fig. A1.47 Permeability vs. net confining pressure for (MWX-2) 57-2 core sample (Group ID 60; depth 8109.7 ft; vertical cut from bottom of whole core sample; nitrogen inlet pressure = 350 spig)

APPENDIX 2. AN ALTERNATIVE METHOD - RIDGE REGRESSION

Hoerl and Kennard[1.7] have presented the mathematical basis and general procedure for ridge regression. The standard model for multiple linear regression is

$$Y = X\beta + \varepsilon \qquad \text{(A2.1)}$$

where Y is an (n x 1) matrix of observed values of the dependent variable, X is an (n x p) matrix of values of independent variables, β is a (p x 1) matrix of unknown coefficients to be estimated, ε is an (n x 1) error matrix, n is the number of observations, and p is the number of independent variables (factors). When X'X (X' is the transpose of X), in the form of a correlation matrix, is such that it has a nonuniform eigenvalue spectrum, the estimates of β, based on the criterion of minimum residual sum of squares, can have a high probability of being far removed from the true values of β. Ridge regression involves adding a small positive quantity k to each diagonal element of X'X. By this method, a system that acts more like an orthogonal system can be obtained. If the biasing parameter k is the same for each diagonal element of the matrix, then the solutions $\hat{\beta}^*$ of

$$[X'X + kI]\ \hat{\beta}^* = X'Y \qquad \text{(A2.2)}$$

where I is the (n x n) identity matrix, can be plotted against k. The resulting plot is called a ridge trace and includes a curve for each of the factors (see Figs. A2.1-A2.3). Such a plot can serve as a two-dimensional characterization of the system and a portrayal of the kinds of difficulties caused by the intercorrelations among the predictors. Examples are used by Hoerl and Kennard[1.8] to illustrate that a very large increase or decrease in the value of an element of $\hat{\beta}^*$ with a small change in k can be a symptom that this estimator is unreliable. Also, if the value of an element of $\hat{\beta}^*$ changes sign as k is increased, the estimator may be regarded as unreliable. Selective removal of factors whose estimators are unreliable can improve the overall estimate. Thus, the ridge trace can guide the user to a better estimate based on $\hat{\beta}^*$. Such an estimate is biased, but it can be used to improve the mean square error of estimation.

Ridge regression[1.7,1.8] was used in the present work to identify variables that are most useful for correlation with sensitivity of permeability to overburden pressure without intercorrelations among the variables excessively distorting values of the corresponding estimates of regression coefficients. With help from some IMSL subroutines, this statistical method was used for a combined data set comprising Suites 1, 2, and 3. A ridge trace involving estimates of coefficients of twelve of the variables listed in Table 1.5 is shown in Fig. A2.1. It can be seen that the coefficients of percents quartz, lithic fragments, total carbonate, and matrix (factors 15, 19, 20, and 21) lose most of their predictive power as the biasing parameter k is increased from 0 to 1. Also, the absolute value of each of the simple correlation coefficients of

pressure sensitivity index with percents of quartz, lithic fragments, and matrix (variables 15, 19, and 21) is less than 0.2. Thus, percents of quartz, lithic fragments, and matrix were removed from further consideration. However, percent total carbonate (factor 20, which had a simple correlation coefficient of about 0.3 with pressure sensitivity index) was allowed to remain. Each time one or more variables were removed from consideration (or restored), ridge regression was started anew for the modified set of variables. Sometimes this resulted in more (or fewer) samples being treated, as there are some samples for which data are incomplete. Such a change in the portion of the data base used typically resulted in the values of the simple correlation coefficients changing somewhat.

The ridge trace for the remaining nine factors is shown in Fig. A2.2. Depth, percents total carbonate and visible porosity from thin section, and crack thickness at 5000 psi (factors 2, 20, 22, and 27) are the least important of these nine factors when $k = 1$. Also, comparison of the ridge trace with simple correlation coefficients (of the above variables with the pressure sensitivity index) shows that, when $k = 0$, estimates of β values for at least three of these factors (factors 20, 22, and 27) all have signs which are opposite to those of the corresponding simple correlation coefficients. Therefore, these four factors were removed from further consideration. The ridge trace shown in Fig. A2.3 was obtained for the remaining five factors. At this point, it was somewhat unclear as to which factor should be removed next. Factor 8 (Klinkenberg permeability at 5000 psi), the coefficient of which exhibits a sign change when k is increased much above zero, seems to be a reasonable candidate for removal. However, the simple correlation coefficient of around -0.5 for Klinkenberg permeability at 5000 psi with the pressure sensitivity index tends to argue against removal.

Since the simple ridge regression method was close to suggesting a final combination of factors, and Klinkenberg permeability at 5000 psi and crack thickness at 500 psi (factors 8 and 26) were among the five factors remaining, another consideration was introduced. As indicated previously, combinations that almost amounted to using the pressure sensitivity to predict the pressure sensitivity index were to be disregarded. Thus, elimination of Klinkenberg permeability at 5000 psi (factor 8) or crack thickness at 500 psi (factor 26) was appropriate. Ridge traces were generated for each of these cases. In another trial, both of these factors were omitted, and percent total carbonate (factor 20) was added to the three remaining. The resulting ridge trace indicated that the earlier elimination of percent total carbonate was appropriate, as its coefficient showed a change of sign, and it had little predictive power when k was increased beyond 0.3. Thus, use of ridge regression for variable selection suggests that, of the twelve variables examined, porosity and percentages of sodium feldspar and chert, and perhaps Klinkenberg permeability at 5000 psi or crack thickness at 500 psi, appear to be the most useful in predicting pressure sensitivity by forming combinations of relevant variables whose intercorrelations do not greatly distort estimates of their true coefficients. The two sets of four curves showing estimates of coefficients of porosity and percentages of sodium feldspar

and chert (in both sets) and Klinkenberg permeability at 5000 psi (in one set) or crack thickness at 500 psi (in the other set) appear to be well behaved. (They appear similar to examples of curves from a well behaved system shown by Hoerl and Kennard[1,8] for a ten factor example with factors 5 and 7 deleted.) Actual vs. predicted pressure sensitivity index plots were generated for the three final combinations of four factors. Observed vs. predicted pressure sensitivity index values for one of these combinations are shown in Fig. 1.23. The estimated values of coefficients for percents porosity, sodium feldspar and chert, and crack thickness at 500 psi were used to generate this figure. Since these coefficients were estimated at $k = 0$, their values correspond to the usual least-squares estimate. Although ridge regression enabled selection of two rather well behaved combinations of variables, their predictive performances are rather disappointing. Further, percent sodium feldspar, one of the variables selected in this approach, appears to be essentially worthless for the usual least-squares estimate.

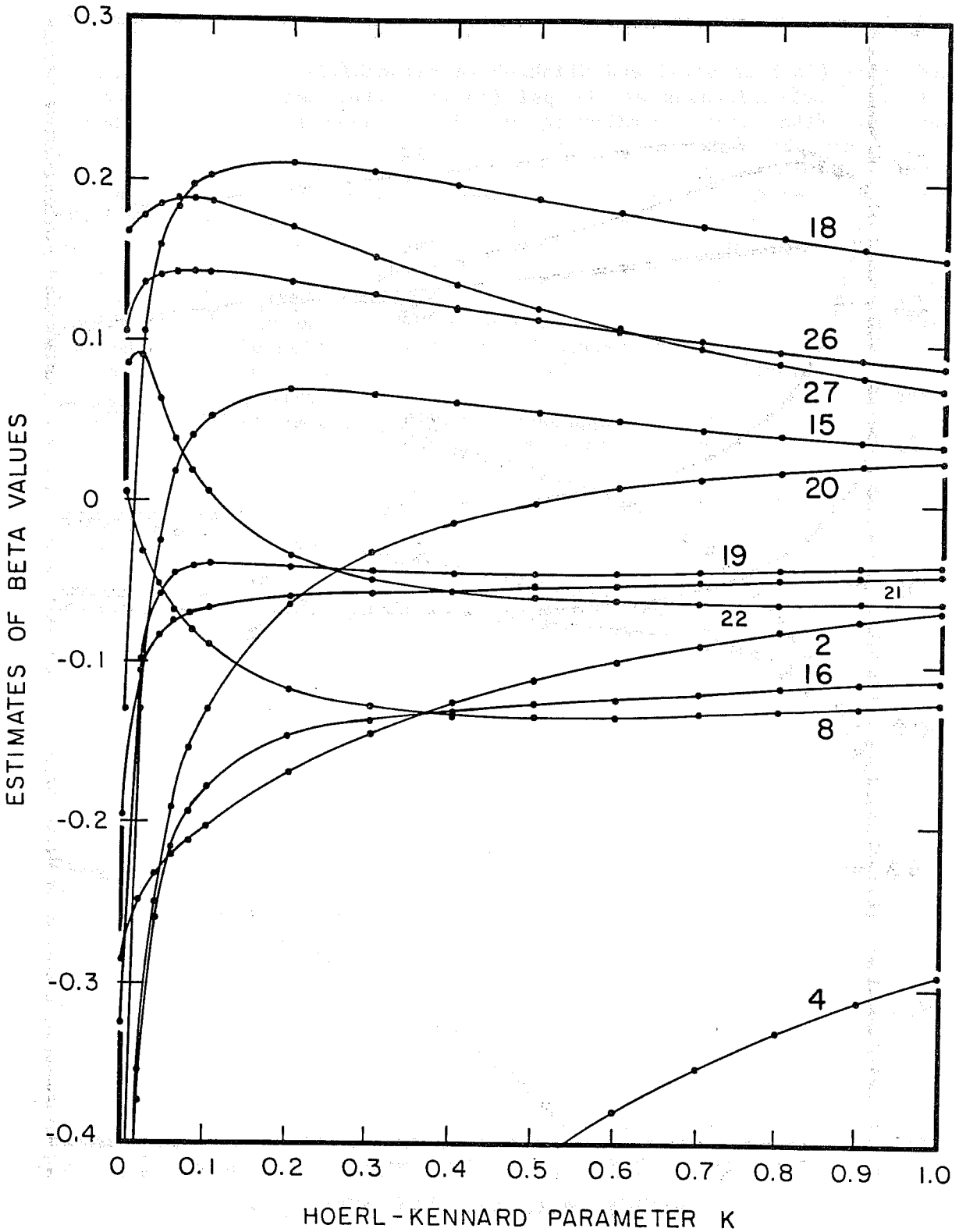

Fig. A2.1 Ridge trace for combined data set (assorted high carbonate, and Multi-Well cores). Variables 15, 19, and 21 are not very good predictors and therefore are to be omitted in the next step.

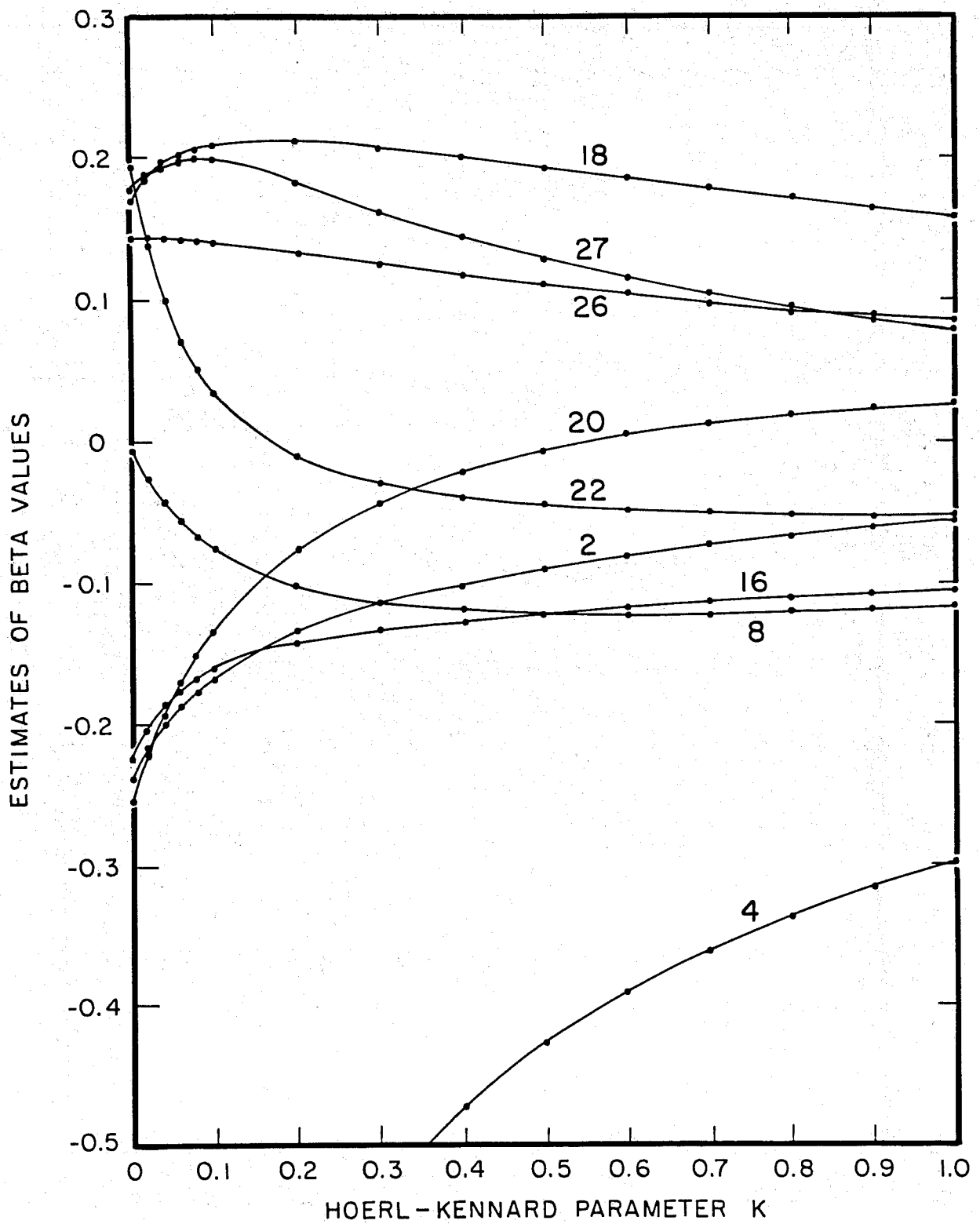

Fig. A2.2 Ridge trace for combined data set (assorted, high carbonate, and Multi-Well cores). Factors 2, 20, 22, and 27 are the least important of these nine factors when k = 1, as can be seen from the estimates of the corresponding beta values being closest to zero.

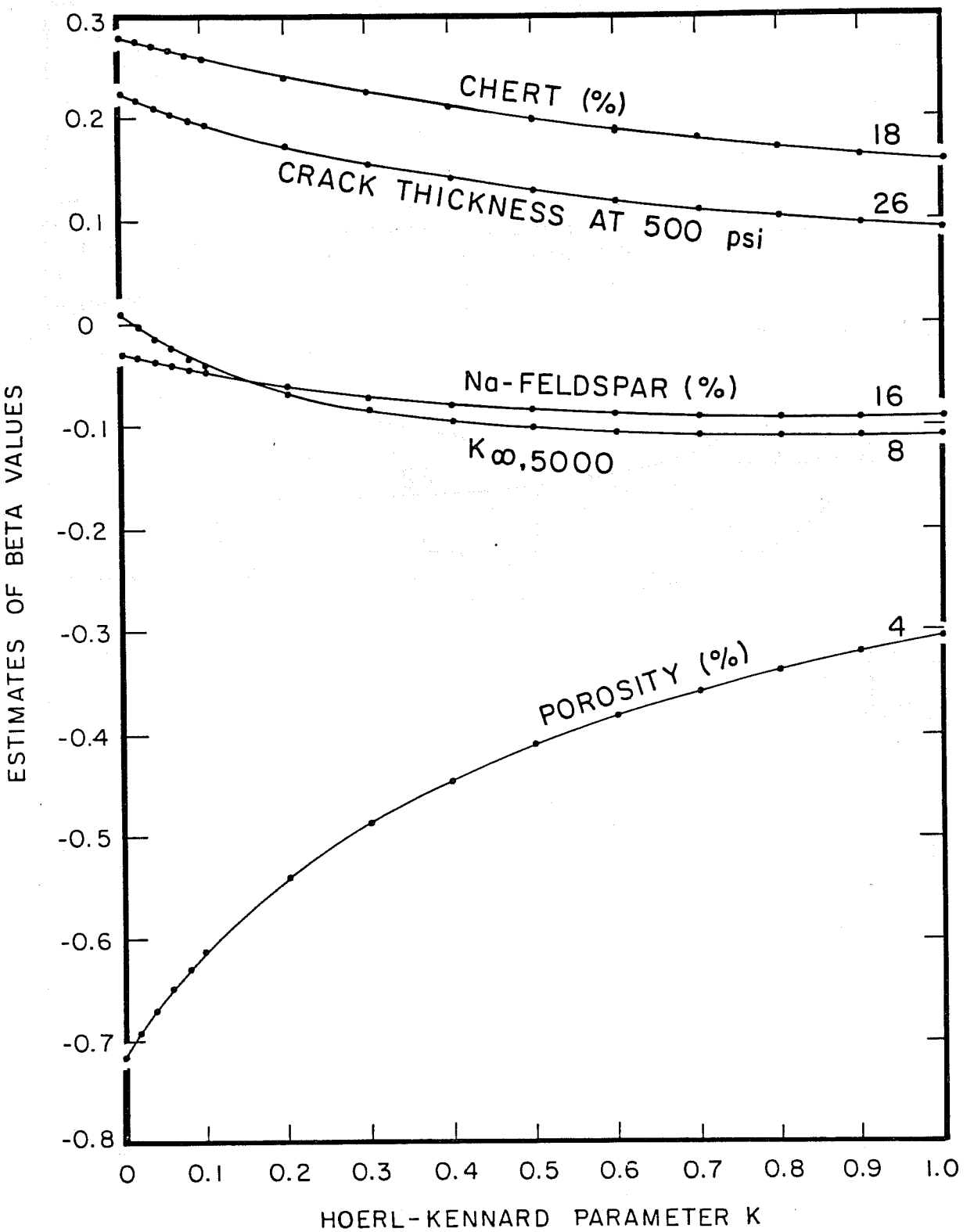

Fig. A2.3 Ridge trace for combined data set (assorted, high carbonate, and Multi-Well cores). Porosity and percent chert seem to be good predictors. Klinkengerb permeability at 5000 psi, percent Na-feldspar, and crack thickness at 500 psi appear to be weaker, but two of these factors can be retained.

ACKNOWLEDGMENT

Special acknowledgment is due to several members of the Department of Energy. They include Herb Carroll with whom technical discussions were initiated, and James Jennings, Leonard Volk, Clarence Raible, and James Chism who in this sequence served as Technical Project Officer. Allan Sattler of Sandia National Laboratories has been extremely helpful in providing samples obtained in the course of the DOE Multi-Well Project and in selecting samples from intervals of mutual interest. X-ray analysis for clays was carried out in the New Mexico Bureau of Mines using techniques suggested by George Austin. Electron microscopy and surface area measurements were carried out in the Department of Metallurgy at NMIMT. The work, over the course of this project, of Kathy Grattan and Janet Golding (technical secretaries), Jessica McKinnis (draftsperson) and Bill DeMarco (photographer), is greatly appreciated. J.J. Taber, director of PRRC, and all other members of PRRC technical and administrative staff, have been unstinting in providing advice and assistance.

☆U.S. GOVERNMENT PRINTING OFFICE:1984 -746-081/ 10098 REGION NO. 4